Cryogenic Spectroscopy of Anionic Biochromophores

by

Wyatt Zagorec-Marks

B.S. University of Utah

A thesis submitted to the

Faculty of the Graduate School of the

University of Colorado in partial fulfillment

of the requirements for the degree of

Doctor of Philosophy

Department of Chemistry

2021

Committee Members:

Carl Lineberger

Heather Lewandowski

J. Mathias Weber

Sandeep Sharma

Veronica Vaida

Zagorec-Marks, Wyatt (Ph.D., Chemistry, Department of Chemistry)

Cryogenic Spectroscopy of Anionic Biochromophores

Thesis directed by Professor J. Mathias Weber

Abstract

Biochromophores are ubiquitous and have the potential to be modified to suit our needs in many applications involving the absorption or emission of visible light. Many chromophores have already been adapted for this purpose and leading to radical changes in their field, such as the implementation of the chromophore of the Green Fluorescent Protein in bioimaging. Not only are these molecules incredibly useful and versatile, they are also interesting from a more fundamental standpoint. They all involve the excitation of electrons residing in conjugated π systems, and both the excited states and the resulting de-excitation dynamics are influenced by the structure of the chromophore and the functional groups present. A thorough understanding of these properties will aid in their modification.

This thesis presents my contribution to the understanding of several biochromophores. The first chapter presents a more in-depth introduction to the field and my place in it. This is followed by a chapter detailing the methodology. The next two chapters focus on two examples of a common functional group in chromophores, the phenolate moiety. This group consists of a deprotonated phenol ring with another functional group branching off the ring, typically in the *para*- position. In the first of these chapters, the functional group is an NO_2 entity, and we explore substitution effects by comparing electronic spectra from the *ortho*-, *meta*-, and *para*- isomers. In the second chapter we look at the chromophore of the Green Fluorescent Protein including experiments on the temperature dependence as well as the effects of microsolvation on the electronic spectra. In

the last two chapters we look at a second common structural motif, tetrapyrrole. This structure consists of four pyrrole rings linked by methine bridges, with the conjugated system spanning all four rings. The first of these chapters details the properties of protoporphyrin, in which the four pyrrole rings form a conjugated ring. Here we investigate the effect of a strong electric field on the photophysical properties. The final chapter details ongoing experiments on a linear tetrapyrrole known as biliverdin.

For Livi

Acknowledgements

While the molecules in this thesis were *in vacuo*, I certainly was not. I received help, guidance, and support from a wide variety of people who deserve mention. First, I have to thank Mathias for everything he has done for me as an advisor. When I originally visited CU Boulder, it wasn't on one of the prescribed graduate student visiting weekends (due to a scheduling conflict). I arrived in town and soon learned that my plans to visit had been misplaced in all the excitement surrounding the hectic event that is graduate recruiting, and no arrangements for faculty meetings, or housing, had been made. I reached out to several of the faculty I had been hoping to meet with to see if they had been contacted at all, and if they had any free time in their schedule to meet with me. Mathias responded quickly, was available to meet, and was immediately contacting the relevant administrators to get things sorted out. This sort of behavior is characteristic of his managing style. He addresses any problems efficiently, always provides useful feedback, and maintains a positive group environment. This is an incredibly important aspect of advisors that is typically not emphasized enough.

While Mathias is an important aspect of the Weber group, he is not the only important part. I have had the privilege to overlap with many fantastic people during my time in the group, all of which I think of as friends first and coworkers second. When I first joined the group, two graduate students, James E. T. Smith and "Xavier" Shuang Xu, were leaving the group and I had minimal interaction with them at that time. I would later collaborate with James on the protoporphyrin project where his expertise and positive attitude were very helpful. There were two other graduate students, Michael Thompson and Curtis Beimborn, who were not on my project and so provided a way to escape the day to day struggles. We frequently had hilarious conversations over lunches or coffee breaks the made every day much more enjoyable. Curtis and I would eventually coauthor a paper which required frequent ski trips to discuss the nature of the reflection of sun light off a crystalline surface, such as snow, and the implications for nanosecond laser experiments on crystalline rubrene. The final member of the Weber group when I joined was a post-doc named Leah Dodson. Typically, Mathias will recruit a new student for a project when the current student on the project is in their 3rd/4th year and knows what they are doing, creating a good amount of overlap with the new student to transfer knowledge. That schedule did not work out when I joined. Instead I got to work with Leah, who had been on the project for a few months and was still learning how to operate what was, at the time, a very temperamental instrument. The skills one arrives with as a first year graduate student are typically limited, to say the least. Mine were not only limited, but they were also only applicable to biochemistry. I knew nothing about vacuum technology, oscilloscopes, wrenches, screwdrivers, or really anything that would be helpful on this instrument. Leah was able to not only teach me these basic things, but she did so in a way that had me operating and troubleshooting the instrument by myself in a relatively short amount of time. My graduate experience would have had a significantly rockier start had it not been for her patience, good sense of humor, and willingness to stand back let me try to fix things. When it came time for me to train my replacement, Madison Foreman and Rebecca Hirsch joined the group. Madison would be working with me and she brought some much needed enthusiasm to a catalysis project which had been on ice for some time. I had a wonderful time training her and am sure her graduate career will be filled with excitement. I overlapped less with Rebecca, as she was on the other low pressure experiment, but because of the culture of the Weber group we still enjoyed many lunches, hiking trips, coffee breaks, etc. together and I wish her luck with her graduate career as well. None of this work would be possible without our funding sources. I was fortunate enough to be funded by the Department of Education through a GAANN fellowship, and the National

Science Foundation through the JILA AMO Physics Frontier Center (award no. PHY-1734006) and through an NSF Chemistry grant (award no. CHE-1764191). I also had access to resources from the University of Colorado Boulder Research Computing Group, which is supported by the National Science Foundation (awards ACI-1532235 and ACI-1532236), the University of Colorado Boulder, and Colorado State University

There are many people outside the Weber group that deserve acknowledgement as well. Every member of the machine shop staff has fielded countless questions from me and have always been incredibly nice and exceedingly helpful. I also had a significant amount of help from those in the electronics shop, as much of our instrument is run by devices they have made. They are always very willing to look at a device that may be misbehaving, help you troubleshoot, provide potentially life-saving tips for working with high voltage after you have broken a high voltage switch. I need to acknowledge James Fung-A-Fat specifically for help with that last item. With his help, the switch was replaced without incident. Like many experiments, much of this experiment relies on old (ancient?) computers talking to each other, running specific programs, and surviving long enough to be useful. None of these things would happen were it not for the work of the computing staff here at JILA. Last but not least, there are a plethora of people in the JILA administration who work tirelessly to make sure graduate students can focus on research. These people do their various jobs so well that most students never have to interact with them at all.

I would also like to thank a few professors outside of JILA. First, my undergraduate research professor Matthew Kieber-Emmons who guided me through my first experiences in scientific research and who is undoubtedly the reason I ended up in a graduate program at all. I also need to thank Jan R. R. Verlet who worked in our group as a visiting professor for a few months and brought with him the molecule which would lead to nearly half of my publications.

He also taught me that while choosing interesting projects is important, it is also good to occasionally pick the low lying fruit (in this case, a very juicy pineapple).

I also need to thank my family for their constant support and interest in what I was doing, even if they didn't really understand the specifics. They certainly made it easier to get through this program, and remain interested in science even when it wasn't cooperating.

Lastly, I need to thank my wife, Livi. Rather than being worried about me moving out of state for a graduate program, she encouraged it and, without hesitation, packed up her things and brought her dog. Throughout my life and graduate career, she has been an excellent sounding board, source of stress relief, and genuinely curious about how things went in the lab each day. She been an incredible motivator by reminding me that no matter how well or terribly things go in the lab, I am still a wonderful trophy husband. For these things, I am eternally grateful.

CONTENTS

Figures

Tables

Chapter 1 Introduction

1.1 Why study biochromophores?

A molecule is considered a chromophore if it absorbs visible light, including the molecules that make bruises blue-green, oranges orange, and ladybugs red, to name a few examples. Biochromophores are those which have biological origins. These molecules typically have a high degree of conjugation and either act alone, or as a cog in a larger machine (such as those present in the chlorophylls of plants) and are often housed in a protein pocket. These protein pockets will often hold a chromophore in a specific configuration, which may not be stable in solution, and provide a specific chemical environment to tune the photophysical properties (absorption spectrum, fluorescence quantum yield, etc.) of the chromophore to suit the needs of the process they are involved in.

Figure 1.1. Image of a *ficus lyrate* (fiddle-leaf fig) from my personal collection. The green coloration is due to various chlorophylls which perform the initial absorption of sunlight in photosynthesis.

Nature has developed a wide variety of chromophores and variants thereof to accomplish a plethora of tasks. Researchers have been able to coerce some of these chromophores to perform other tasks, and one of the best examples of this is the use of the Green Fluorescent Protein (GFP). This protein was originally isolated from the jellyfish *Aequorea victoria* and has since become a work-horse in fluorescence labeling in biology and biochemistry (which lead to the Nobel Prize in Chemistry in 2008). The fluorescence of GFP originates from a relatively small chromophore consisting of a phenol ring linked to an imidazole ring. This chromophore has been modified, both by nature and by researchers, to emit at a variety of wavelengths.

Figure 1.2. Image of organ pipe coral of the genus *Tubipora* from my personal collection. The red coloration is due to a combination of biochromophores, including carotenoids which produce the bright orange color of carrots.

In order to expand the capabilities of chromophores, a great deal of research has gone into understanding how they work. Most of these experiments have been performed on chromophores in the condensed phase (e.g., in solution, crystals, or a protein environment), which makes sense as that is where they are found and will be used. The present work involves the application of laser spectroscopy to cryogenically prepared ionic biochromophores *in vacuo*.

1.2 Why *in vacuo*?

When studying chromophores in the condensed phase, one must be cognizant of interactions between the molecule of interest and the chemical environment. Electronic transition energies of the same molecule dissolved in different solvents, or housed in a protein pocket, can vary significantly (solvatochromism). These shifts can range from barely noticeable to thousands of cm^{-1}, and can result in higher or lower transition energies. This makes it important to specify the solvent, as well as characteristics such as pH, when reporting an electronic transition in solution. Speciation in solution can be an issue if there are breakdown products, mixtures of isomers, varying degrees of protonation, or aggregation effects to name a few situations. When taking spectra of such a solution, one acquires the response from every species present, which can be challenging, if not impossible, to disentangle. Together, these effects, among others, can make it difficult to compare experimental data to theoretical results, or even to other experimental data. Having experimental data on the intrinsic photophysical properties of a chromophore (i.e., independent of its chemical environment) is highly desirable when one is looking to modify its properties, but this is impossible to achieve in the condensed phase. Studying molecules *in vacuo* allows investigation of their properties as an isolated system, free from any interaction with a chemical environment, and provides clean access to their intrinsic photophysics. By looking at ionic chromophores, we are able to employ mass spectrometric techniques and select ions by their mass-to-charge ratio, eliminating many problems that can arise in the condensed phase due to speciation.

Spectra taken in solution are often plagued by other effects that limit the detail that can be extracted from them. A typical solution UV/vis spectrum is taken at room temperature and consists of broad and featureless absorption bands, which makes a detailed understanding of the underlying photophysics inaccessible. To gain valuable information from a spectrum, one must be able to resolve individual transitions which typically requires substantially cooling the molecule of interest to suppress the broadening induced by thermal excitation (hot bands). This can be achieved in frozen solutions, but here one encounters matrix effects, which additionally complicate interpretation. We are able to cool molecules *in vacuo* to cryogenic temperatures using buffer gas cooling techniques, which, in cases where temperature was a significant cause of the spectral broadening, can greatly improve spectral resolution.

1.3 Scope of this thesis

This thesis involves infrared (IR) and electronic photodissociation spectroscopy of cryogenically prepared, mass-selected ions *in vacuo* used to investigate the intrinsic electronic and molecular structure of anionic biochromophores. The experimental methods are described in detail in Chapter 2. Chapters 3 and 4 will explore molecules containing a phenolate moiety, a functional group observed in many chromophores. Nitrophenolates will be the subject of Chapter 3, where we will observe the power of the experimental technique on a nearly ideal molecular system. Chapter 4 describes work on the GFP chromophore. It also introduces the idea of a microsolvation environment (where the ion is solvated by only a few solvent molecules), which can be thought of as bridge between experiments done *in vacuo* and those done in solution. Chapters 5 and 6 discuss tetrapyrroles, which consist of four pyrrole rings linked by methine bridges, and occur in a wide range of biological systems. Protoporphyrin, where the pyrrole rings form a macrocycle, is the subject of Chapter 5. In addition to the spectroscopy of this molecule, we explore the effect of the electric field of a point charge located a few Å away from the conjugated system. Ongoing work on biliverdin is discussed in Chapter 6. Biliverdin is structurally similar to protoporphyrin, as it has similar building blocks, but the conjugated macrocycle found in porphines is broken, forming a linear tetrapyrrole instead. In this chapter, we again explore the effect of a negative charge near the conjugated system of a very promising near-IR emitter which may not be being used to its full potential.

Chapter 2 Methods

2.1 Overview

The experiments described here were done using a home built photodissociation mass spectrometer.[1] In a typical experiment, the ions are initially generated through electrospray ionization using either water, methanol, or a mixture of the two as the solvent. The ions are then guided through a series of differential pumping stages by octopole ion guides and lenses until they reach a 3D quadrupole ion trap (Paul-trap). This trap is mounted on a closed cycle helium cryostat and is equipped with a resistive heater to allow control of the cold head temperature from 4-300 K. Ions are held in this trap with an inert buffer gas for an amount of time dependent on the repetition rate of the experiment (45 or 95 ms for 20 Hz or 10 Hz, respectively). During this time, the ions are colliding with the buffer gas molecules, which are in turn colliding with the walls of the trap, cooling the ions. Three body collisions in the cold buffer gas can lead to formation of weakly bound clusters between the ions of interest and the buffer gas. These clusters are often useful in our experiments, as will be discussed in greater detail below. Once the ions are cooled, they are ejected as a packet into a time-of-flight mass spectrometer. After a few μs flight time, the packet separates by mass-to-charge ratio (m/z) and encounters a pulsed mass gate, which allows transmission of a particular m/z, while discarding the rest. The selected ion species is then irradiated by the output of a tunable light source (600-4000 cm^{-1} for IR spectroscopy, 220-2500 nm for UV-Vis spectroscopy). Absorption of a photon (or in some cases a few photons) places the ion in an excited state with few relaxation options. If the ions absorb enough energy, the ions can dissociate into fragments. A reflectron is used to separate the fragments from any parent ions that have not dissociated, and the formation of fragments is monitored as a function of the laser wavenumber. Results are compared to calculations performed on the RMACC Summit supercomputing cluster at CU Boulder.[2]

2.2 Ion preparation

2.2.1 Electrospray ionization

Many biochromophores exist as charged species which enables the use of mass spectrometric techniques to study them. A widely used method of getting biologically relevant molecules into the gas phase is to use electrospray ionization (ESI).[3] This method is often chosen because it can get large, fragile molecules into the gas phase without fragmenting them. The experimental setup involves taking a molecule of interest dissolved in a volatile, polar solvent such as water or methanol, and spraying the solution out of a small highly charged needle (ca. -3-4 kV) aimed at a desolvation capillary that serves as a counter electrode (ca. -300 V) and provides the entry into the vacuum system of the apparatus. The potentials given here are typical for anionic species, but we note the apparatus can also produce cationic species in which case the polarity is swapped to produce positive values. In our experiment (see Figure 2.1), the spray assembly is a commercial product (Analytica of Branford), and the solution is pumped through a silica capillary (75 μm ID, 193 μm OD, Polymicro Technologies) inside the needle at a rate of ca. 50 μL/h by a syringe pump (New Era, model NE-1000). At the tip of the silica capillary, a cone forms as a result of surface tension of the solution, the Coulomb repulsion of the dissolved ions, and the electric field of the needle attempting to expel the ions (Taylor cone). The tip of this cone emits a fine mist of small, highly charged droplets. As solvent evaporates from these droplets, the density of charged species increases, leading to the eventual breakdown of the droplets. This process repeats itself until all that remains are bare ions in the gas phase. This spray is entrained in a nebulizing gas of dry N_2. The desolvation capillary is heated to aid in evaporation of any remaining solvent molecules as ions pass through it into the first differential pumping stage of the experiment.

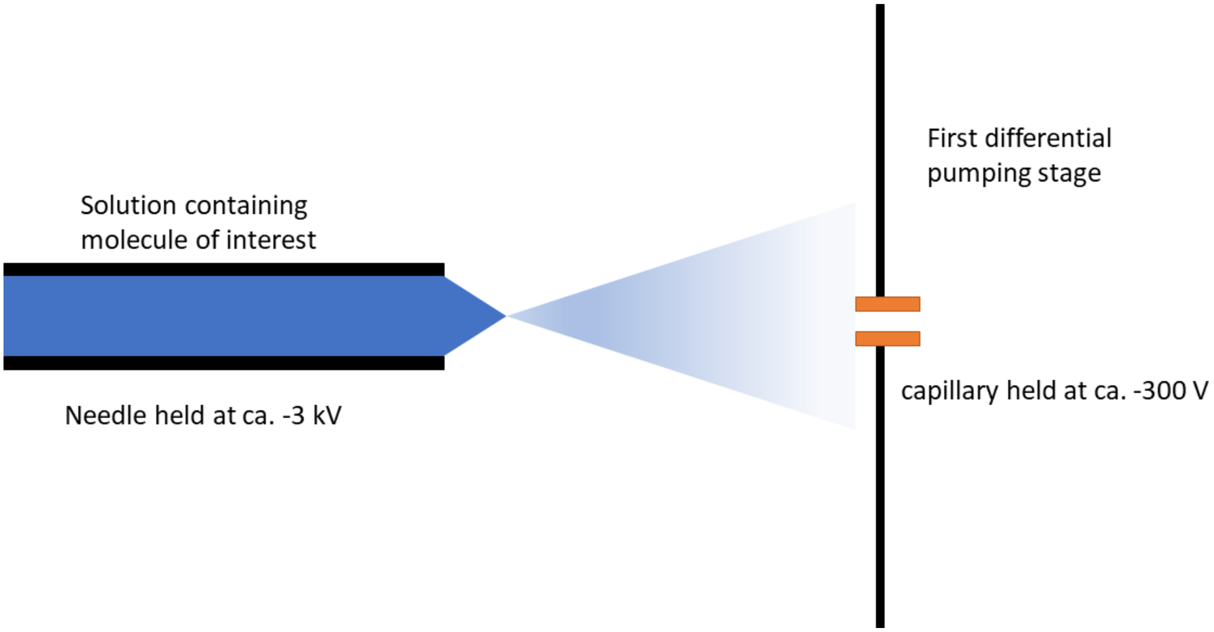

Figure 2.1. Cartoon of the electrospray source.

2.2.2 Pre-trap ion guides

The electrospray process occurs at ambient pressure and time-of-flight mass spectrometry (TOF-MS) requires high vacuum conditions ($<10^{-6}$ mbar). A series of four differential pumping chambers are used to step the pressure down to this level. For the ions, the first chamber comprises a ca. 1 cm flight distance from the exit of the capillary, through a focusing lens, and into a skimmer that separates the first chamber from the second. The first chamber is pumped by a 65 m^3/h rotary vane pump (Leybold, Trivac D65 B) and operates at ~1 mbar. The second chamber contains an octopole ion guide that is ~14 cm long, at the end of which is another skimmer. The chamber is pumped by a second 65 m^3/h rotary vane pump (Leybold, Trivac D65 B) and reaches pressures of ~0.1 mbar. The second skimmer is pulsed from a high potential (ca. -100 V) to a lower potential (ca. -50 V). While the skimmer is held at the high potential, this region of the experiment accumulates ions until the skimmer is pulsed to the low potential. We refer to this region as the "pre-trap" and it allows us to take the continuous source of ions that ESI generates and create a pulsed source. A pulsed source is advantageous as it provides a more uniform cooling time for the ions when they reach the cryogenic trap. After passing through the second skimmer, the ions pass into a third chamber which contains a ~30 cm long octopole ion guide. The third chamber is pumped by a 685 L/s turbomolecular pump (Pfeiffer HiPace 700) and reaches operating pressures of 10^{-4} mbar. An electrostatic lens bridges the gap between the third and fourth differential pumping chamber where the ion packets are guided by another ~30 cm long octopole into a home built quadrupole bender. The bender turns the ion path by 90 degrees to separate out any remaining neutrals before the ions pass through a set of electrostatic lenses and a final octopole before they enter the 3D quadrupole trap. This chamber is pumped by a 1100 L/s turbomolecular pump (Leybold Turbovac 1000 C) and has a typical operating pressure of 10^{-6} mbar.

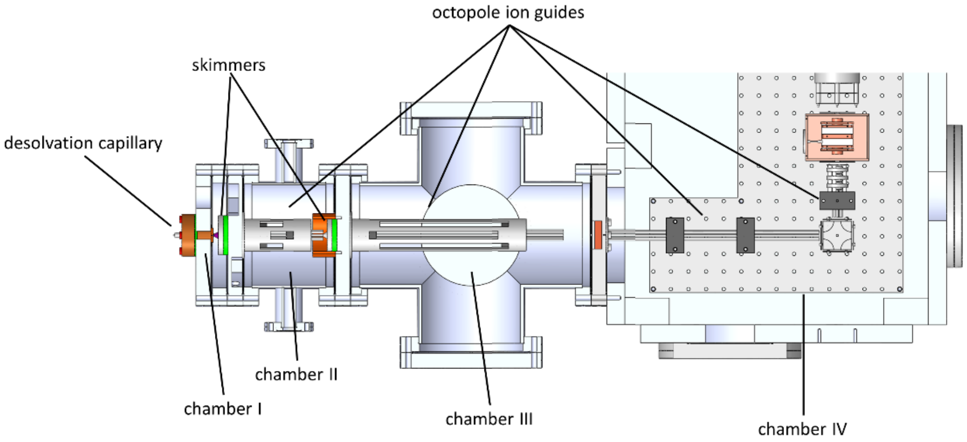

Figure 2.2. Instrument drawing of the source region from the desolvation capillary to the 3D quadrupole trap.

2.2.3 Cryogenic ion trap

Our 3D quadrupole trap was modeled after a stainless-steel trap purchased from Jordan TOF products but was instead machined from copper for better thermal properties. The trap is mounted on the cold head of a closed cycle helium cryostat (Sumitomo F-70L, 1.5 W at 4.2 K) and is equipped with a resistive heater to allow temperature control from 4 K to 300 K. The trap is enclosed in an OFHC copper heatshield which is mounted to the outer stage of the cold head, keeping the heatshield at ca. 40 K. Helium buffer gas is admitted into this trap at the same time as the ions by a pulsed valve (Parker General Valve Series 99). Depending on the repetition rate of a particular experiment, 10 Hz or 20 Hz, the ions are held in the trap for 45 or 95 ms. During this time, the ions collide with the buffer gas, which is in turn colliding with the cryogenic walls of the trap, cooling the ions.

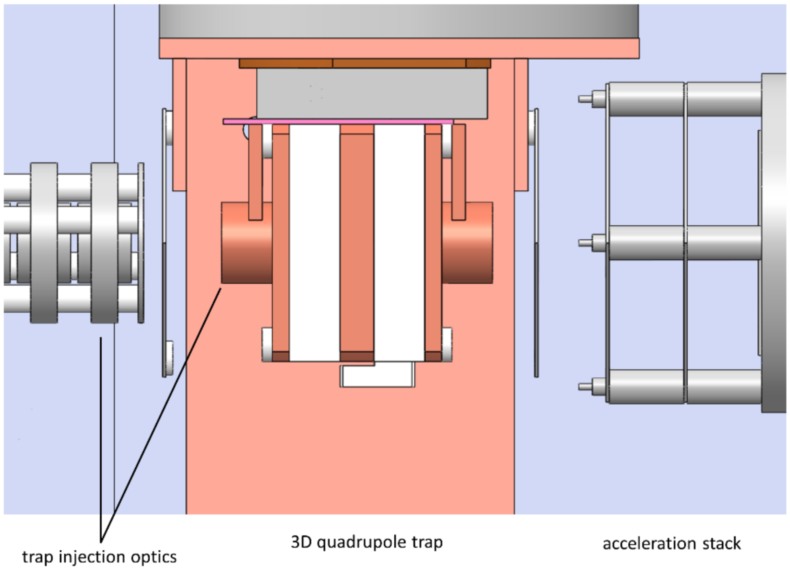

Figure 2.3. Zoom in on 3D quadrupole trap and nearby ion optics.

As the ions cool, complexes with other molecules in the trap can be formed in three-body collisions. In the experiments described in this thesis, complexes with N_2, D_2, and H_2O were studied. N_2 and water molecules are part of the residual gas from the ESI source. Complexes with D_2 are formed by seeding the helium buffer gas with D_2 (10%). These complexes form over unique temperature ranges, which are determined by the balance of their temperature dependent vapor pressure, and the binding energy of the complexes (temperatures leading to internal energies higher than the binding energy of the complex lead to a dissociation event). This complexation is demonstrated by dodecanedioic acid dianion ($DDDA^{2-}$) in Figure 2.4, which we often employ for diagnostic purposes. All of these complexes can be useful in photodissociation spectroscopy, which will be discussed in section 2.4. The choice of running an experiment at 10 Hz or 20 Hz depends on several factors. 10 Hz allows more cooling time, and thus the stored ions get colder resulting in larger complexes with weakly bound molecules. For some molecules which are reluctant to form complexes at all, using a lower repetition rate can be critical to forming them. The advantage of operating at 20 Hz is a reduction in the time required to collect data. This can be done when the ion signal is intense enough, and any desired complexes still form despite the shorter cooling period.

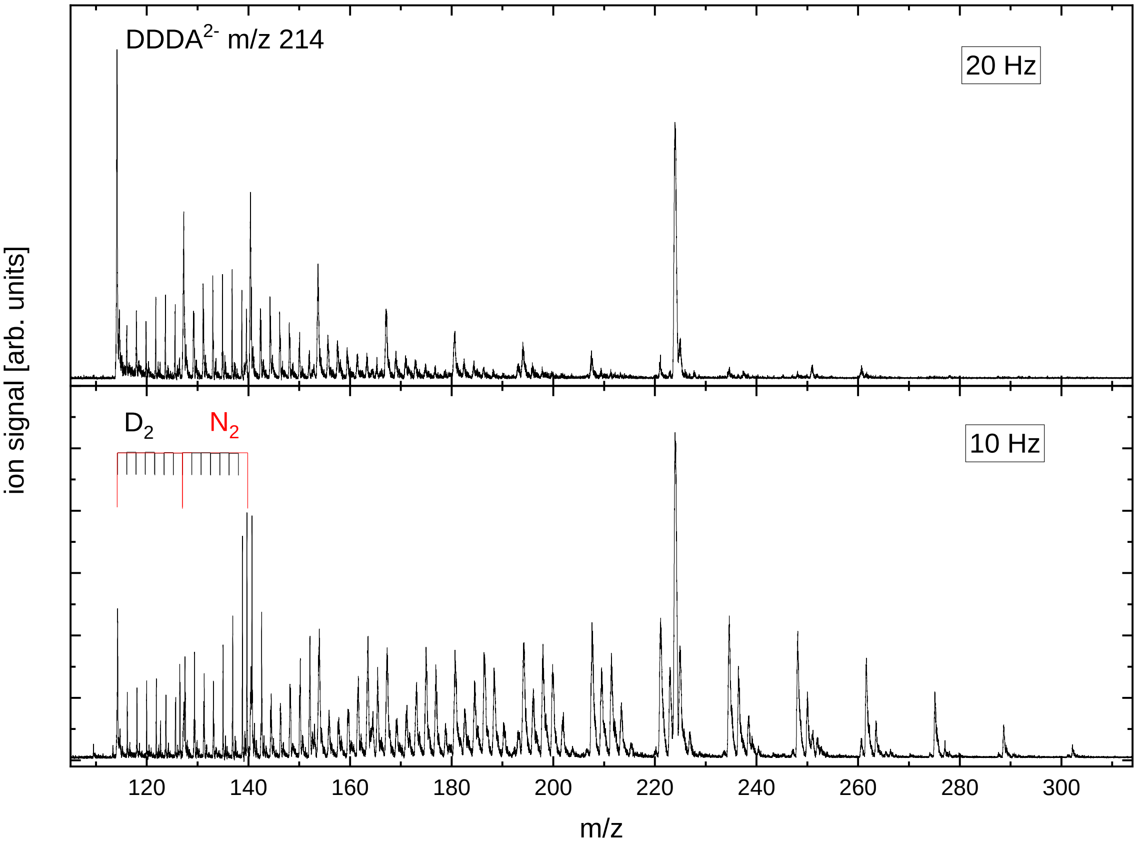

Figure 2.4. Mass spectrum of dodecanedioic acid dianion (DDDA2-) taken at 33 K trap temperature and a repetition rate of 20 Hz (top) and 10 Hz (bottom). All other parameters are kept constant. This molecule complexes with D_2 and N_2 at this temperature at both repetition rates, but significantly more complexes are observed with a 10 Hz repetition rate, indicative of a lower ion temperature.

2.3 Time-of-flight mass spectrometry

After the ion packets have cooled, and formed any desired complexes, they are ejected from the trap by pulsed potentials on the endcaps of the cryogenic trap, creating a ~50 V/cm potential gradient across the trap pushing the ions out through an exit lens. The contents of the cryogenic trap drift into series of three electrodes, one grounded and two with pulsed potentials which are initially held at ground. The two later electrodes are pulsed to ~300 V and ~4000 V in a

Wiley-McLaren arrangement.[4] When the ion packet is between the first and second electrode. The resulting electric field accelerates the ion packets into the final set of chambers of our experiment, the first of which is a differential pumping stage pumped by a 230 L/s turbomolecular pump (Pfeiffer TMU261) and operating at 10^{-7} mbar. In this chamber, we have a set of x and y deflectors which consist of 2 sets of metal plates each, as well as an Einzel lens to adjust the ion trajectories. The second chamber is the flight tube of the TOF-MS, which is pumped by a 520 L/s turbomolecular pump (Pfeiffer TMU521) and operates at 10^{-8} mbar.

If one assumes that the drifting packet of ions all have identical starting positions, then every ion in the packet receives the same amount of initial kinetic energy (KE) from the acceleration pulse. This can be expressed as:

$$KE = \frac{m}{2z}v^2 = U$$

Where m/z is the mass-to-charge ratio of the ion in question, v is the velocity, and U is the potential difference between the plates causing the acceleration. Assuming a constant flight length L for all ions (about 2 m in this experiment) a relationship between the m/z of a pair of ions and their flight times assuming the same initial KE is given by:

$$\sqrt{\frac{m_1}{m_2}} = \frac{t_1}{t_2}$$

This gives a simple way to assign a mass spectrum assuming one knows the m/z of at least one feature in the spectrum. Of course the underlying assumption that all the ions have identical starting positions is not true in any experimental situation, and in particular ours where the ions have drifted ca. 2 cm to arrive at the acceleration region. The packet that is actually accelerated is more accurately represented as a cloud of ions spread between the two electrodes.

In a Wiley-McLaren setup, ions closer to the first electrode receive a higher initial KE than those closer to the second electrode when the voltages are pulsed on. All of the ions receive the same, and substantially larger, KE from the potential drop across electrodes 2 and 3. The difference in initial KE incurred in the first region results in a slightly higher velocity for ions that were closer to the first electrode and a point in space where eventually these ions overtake those that started closer to the second electrode. The location where this occurs can be tuned by adjusting the potentials of the first two electrodes and is called the space focus of the mass spectrometer. In our experiment, the space focus occurs at the laser interaction region, where we have a microchannel plate (MCP) detector that can be moved into the ion beam for diagnostic purposes. Just before the laser interaction region, we have a home built mass gate which is a collection of parallel shim electrodes that can be biased with alternating polarity. The mass gate is pulsed such that when an ion of interest impinges upon it the potentials of all shims are held at ground, and the rest of the time they are held at +/-100 V to cause ions to be deflected, preventing their detection. This allows us to select a particular ion by its mass-to-charge ratio to continue to ion detection, while removing all others. All of this is contained in our flight tube which is the final chamber of the experiment.

Ions that have been selected to pass through the mass gate are irradiated by the output of our laser system (see section 2.5), and the photodissociation products continue to drift until they encounter a two-stage reflectron (Jordan TOF), which reflects the ions towards another MCP detector, giving the ions flight path a “U” shape. The reflectron has three purposes in this experiment. It nearly doubles the flight distance, which leads to an increase in the resolving power of the mass spectrometer. It also allows us to separate fragment ions formed before entering the reflectron from any parent ions who did not dissociate. Finally, after the ions pass through the laser interaction region where they were tightly focused they will become unfocused again. The reflectron introduces a second focal point to the trajectory of the ions that is tuned to occur at the detection MCP.

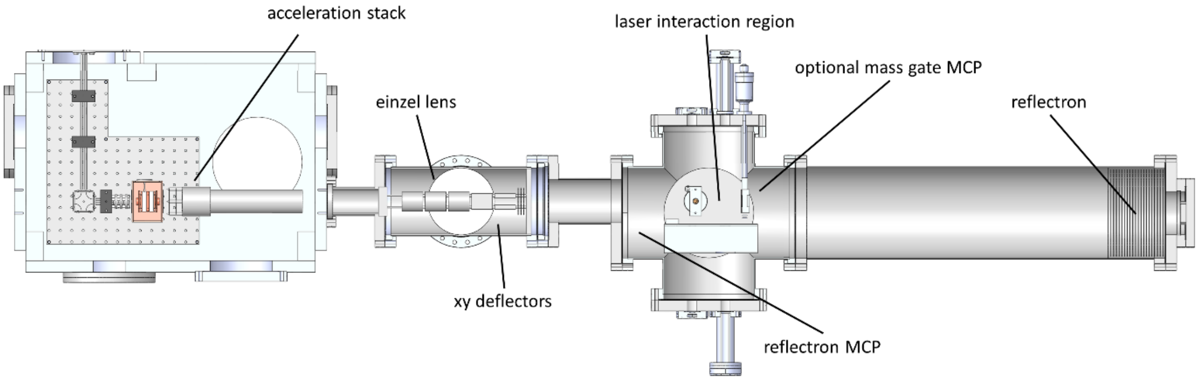

Figure 2.4. Diagram of the mass spectrometer.

2.4 Photodissociation spectroscopy

Photodissociation spectroscopy involves a molecule absorbing a photon and subsequently dissociating. In our experiment, the laser light is introduced at the first space focus of our Wiley-McLaren setup. If the ions absorb an incident photon (or several depending on the molecule, laser intensity, and experiment) the energy is redistributed throughout the modes of the molecule producing a vibrationally “hot” ion with no solvent bath to dissipate this excess energy. One way the ions can dissipate the energy is to dissociate. In the case of UV-Vis experiments, with photon energies on the order of a couple eV, a single photon (or multiple) can cause dissociation of some chemical bonds. In the case of IR experiments, photon energies are substantially lower, in the range of 1000-4000 cm^{-1}. If one has access to a more intense light source, such as a free electron laser[5-7] it is possible to get absorption of many photons and break chemical bonds with IR photons. We rely instead on a technique referred to as messenger tagging. This entails forming clusters of the ion of interest with weakly bound messenger tags, such as N_2 or D_2 whose binding energy to the ion is on the order of a few hundred cm^{-1}.[8-9] Using messenger tagging provides a low energy pathway to dissociation while introducing minimal perturbation to the molecular system. The degree of this perturbation is investigated in Chapter 4 where another path to dissociation is explored. As discussed earlier, we also form clusters with water molecules which, while binding energies are typically weaker than chemical bonds (ca. 0.5 eV), can have significant perturbations on the ion of interest which is also visited in Chapter 4. If dissociation occurs before the ions reach the reflectron (ca. 10 μs after irradiation) the reflectron is used to separate the fragments from the undissociated parent ions, which would otherwise have the same velocity and thus the same arrival time at a detector in a linear detection setup.

2.5 Laser system

2.5.1 IR light source

The IR light source used in these experiments is an IR optical parametric converter (OPC) system (Laservision) which produces 900 to 4000 cm^{-1} light with linewidth of ~2 cm^{-1} and a pulse duration of 5 ns. The system is pumped by a Nd:YAG laser (Innolas Spitlight 600, 5 ns pulse, 500 mJ/pulse, 1064 nm) which is run at half the repetition rate of the mass spectrometer for reasons discussed in Section 2.6. The output of the 1064 nm pump beam is split into two beams, one of which is frequency doubled to produce 532 nm light, which then pumps an optical parametric oscillator (OPO) consisting of two potassium titanyl phosphate (KTP) crystals. This generates a signal and idler wave (ν_{signal} 710–880 nm, and ν_{idler} 1345–2122 nm). The photon energy and momentum of these waves adds up to the 532 nm pump energy and momentum. The signal wavelength and any residual 532 nm light is removed using a Si filter which is transparent to the idler beam. The idler beam propagates through a $\lambda/2$ wave plate, rotating its polarization by 90º, and then mixes with the second 1064 nm pump beam in an optical parametric amplifier (OPA), which consists of a set of four potassium titanyl arsenate (KTA) crystals. The idler beam from the OPO and the 1064 nm pump beam are difference-frequency mixed to create mid-IR light (ν_{mid}) from 2100 to 4000 cm^{-1}. Any residual 1064 nm pump is removed from the beam using a dichroic beam splitter. Depending on the experiment, the idler beam is either removed by a polarizer at this point, or the mid IR and idler beam are routed together into a silver gallium selenide ($AgGaSe_2$) crystal, where difference frequency mixing of the beams produces our far-IR (ν_{far}) beam with wavenumbers of 900 to 2150 cm^{-1}. Residual mid-IR and idler light is removed using a germanium filter. Because ambient water and CO_2 are strong IR absorbers in the spectral region of this system, the entire beamline is enclosed and continuously purged with dry nitrogen.

2.5.2 UV-Vis light source

Like the IR light source, the UV-Vis source in these experiments is an OPC system (GWU) which produces irradiation from 220 – 2500 nm with a linewidth of 5 cm^{-1} and a pulse duration of 5 ns. The system is pumped by the third harmonic (355 nm) of another Nd:YAG laser (Innolas Spitlight 600, 5 ns pulse, 100 mJ/pulse, 355 nm) which is run at half the experimental rep. rate for reasons discussed in section 2.6. The 355 nm pump beam is introduced to one of two Type II beta barium borate (BBO) crystals that convert the pump beam into a signal and idler beam under photon energy and momentum conservation. One of the BBO crystals, referred to as the "red" crystal, generates a signal beam from 505-710 nm and an idler from 710-1190 nm. The other crystal, referred to as the "blue" crystal, generates a signal beam from 415-515 nm and an idler of 1140-2450 nm. The output of the OPO passes through a UV filter to remove any residual pump beam. In order to generate UV irradiation, an additional set of BBO crystals can be installed after the OPO. With the output of only the OPO, second harmonic generation can be performed to generate 220-257 nm light from the "blue" OPO setup or 257-354 nm from the "red" OPO setup. One can also use sum frequency mixing (SFM) with 1064 nm pulses from the pump laser to generate 299-350 nm or 350-404 nm irradiation from the "blue" and "red" OPO crystals, respectively. Any light generated in the OPC system passes through a Pellin-Broca prism to allow selection of a specific wavelength to route to the molecular beam apparatus. All other beams are dumped before exiting the OPC system.

2.6 Data collection

All ion detection is done using an MCP detector after the reflectron (see section 2.3). The signal generated is visualized on two oscilloscopes (Tektronix TDS 2022). These oscilloscopes and the laser system in use are triggered at half the experimental repetition rate of the mass spectrometer (10 Hz for a 20 Hz experiment, 5 Hz for a 10 Hz experiment). One of the oscilloscopes is triggered in phase with the laser system, while the other is triggered out of phase, providing us a display of the ion signal with and without laser irradiation. The intensity of the ion signal is averaged over 16 shots per data point to reduce noise. When collecting data, we set the oscilloscopes to display only the fragment peak and monitor the intensity of this peak as a function of laser wavelength, using the oscilloscopes as boxcar averagers for the ion signals with and without laser irradiation. The IR laser pulse energy is monitored by reflecting a small portion of the beam into a pyroelectric joule meter using a KBr window before the beam enters the vacuum apparatus. The UV-Vis laser pulse energy is also monitored by a pyroelectric joule meter, but this is placed at the exit window of the vacuum apparatus and is thus monitored after interacting with the ions. Absorption of laser light by the ions of interest is too low to have a detectable effect (due to the low density of ions, 100-10^4 ions per ion packet) on the measured laser pulse energy, so measurement before and after interaction of the ions yields the same result. The laser pulse energy is monitored by the second channel of the oscilloscope that measures the “laser on” signal. While the ion signal and laser pulse energy are being monitored, the wavelength of the OPC system in use is scanned through the desired tuning range by a LabVIEW program, which is simultaneously collecting output from the oscilloscopes. We subtract the “laser off” signal from the “laser on” signal for the fragment peak and then correct for photon fluence by dividing the signal intensity by the photon number per pulse as a function of photon energy. Individual scans are collected for at least 2 days to verify reproducibility (often more time is often required to achieve an adequate signal-to-noise ratio).

2.7 Computational

Calculations are used in all our experiments in order aid in the interpretation of spectra. All of our calculations were performed using Gaussian 16.[10] Specifics of calculations vary by experiment, but in general we use density functional theory (DFT, typically B3LYP[11] or the range corrected CAM-B3LYP[12], but occasionally ω-B97XD[13]) to calculate ground state geometries and harmonic frequencies which we then compare to experimental IR spectra. In many cases we employ time-dependent DFT to calculate excited state structures in efforts to interpret UV-Vis spectra. Initial structural guesses are often based on chemical intuition or previous experiments but these frequently had to be modified to reach a structure that best reproduced the experimental results. The basis sets employed are reported in the relevant sections, but they include def2-TZVPP[14] and cc-pVDZ[15].

2.8 References

1. Xu, S.; Gozem, S.; Krylov, A. I.; Christopher, C. R.; Mathias Weber, J., Ligand influence on the electronic spectra of monocationic copper–bipyridine complexes. *Physical Chemistry Chemical Physics* **2015,** *17* (47), 31938-31946.
2. Anderson, J.; Burns, P. J.; Milroy, D.; Ruprecht, P.; Hauser, T.; Siegel, H. J., Deploying RMACC Summit: An HPC Resource for the Rocky Mountain Region. In *Proceedings of the Practice and Experience in Advanced Research Computing 2017 on Sustainability, Success and Impact*, Association for Computing Machinery: New Orleans, LA, USA, 2017; p Article 8.
3. Fenn, J. B.; Mann, M.; Meng, C. K.; Wong, S. F.; Whitehouse, C. M., Electrospray ionization for mass spectrometry of large biomolecules. *Science* **1989,** *246* (4926), 64.
4. Wiley, W. C.; McLaren, I. H., Time-of-Flight Mass Spectrometer with Improved Resolution. *Review of Scientific Instruments* **1955,** *26* (12), 1150-1157.
5. van Geenen, F. A. M. G.; Kranenburg, R. F.; van Asten, A. C.; Martens, J.; Oomens, J.; Berden, G., Isomer-Specific Two-Color Double-Resonance IR2MS3 Ion Spectroscopy Using a Single Laser: Application in the Identification of Novel Psychoactive Substances. *Analytical Chemistry* **2021,** *93* (4), 2687-2693.
6. Bakels, S.; Gaigeot, M.-P.; Rijs, A. M., Gas-Phase Infrared Spectroscopy of Neutral Peptides: Insights from the Far-IR and THz Domain. *Chemical Reviews* **2020,** *120* (7), 3233-3260.

7. Prazeres, R.; Berset, J. M.; Chaput, R.; Glotin, F.; Jaroszynski, D. A.; Ortega, J. M., CLIO, an infrared free electron laser facility. *Nuclear Instruments and Methods in Physics Research Section B: Beam Interactions with Materials and Atoms* **1994,** *89* (1), 54-59.

8. Weber, J. M.; Robertson, W. H.; Johnson, M. A., Argon predissociation and electron autodetachment spectroscopy of size-selected CH3NO2−·Arn clusters. *The Journal of Chemical Physics* **2001,** *115* (23), 10718-10723.

9. Xu, S.; Smith, J. E. T.; Weber, J. M., The electronic spectrum of cryogenic ruthenium-tris-bipyridine dications in vacuo. *The Journal of Chemical Physics* **2016,** *145* (2), 024304.

10. Frisch, M. J.; Trucks, G. W.; Schlegel, H. B.; Scuseria, G. E.; Robb, M. A.; Cheeseman, J. R.; Scalmani, G.; Barone, V.; Petersson, G. A.; Nakatsuji, H.; Li, X.; Caricato, M.; Marenich, A. V.; Bloino, J.; Janesko, B. G.; Gomperts, R.; Mennucci, B.; Hratchian, H. P.; Ortiz, J. V.; Izmaylov, A. F.; Sonnenberg, J. L.; Williams; Ding, F.; Lipparini, F.; Egidi, F.; Goings, J.; Peng, B.; Petrone, A.; Henderson, T.; Ranasinghe, D.; Zakrzewski, V. G.; Gao, J.; Rega, N.; Zheng, G.; Liang, W.; Hada, M.; Ehara, M.; Toyota, K.; Fukuda, R.; Hasegawa, J.; Ishida, M.; Nakajima, T.; Honda, Y.; Kitao, O.; Nakai, H.; Vreven, T.; Throssell, K.; Montgomery Jr., J. A.; Peralta, J. E.; Ogliaro, F.; Bearpark, M. J.; Heyd, J. J.; Brothers, E. N.; Kudin, K. N.; Staroverov, V. N.; Keith, T. A.; Kobayashi, R.; Normand, J.; Raghavachari, K.; Rendell, A. P.; Burant, J. C.; Iyengar, S. S.; Tomasi, J.; Cossi, M.; Millam, J. M.; Klene, M.; Adamo, C.; Cammi, R.; Ochterski, J. W.; Martin, R. L.; Morokuma, K.; Farkas, O.; Foresman, J. B.; Fox, D. J. *Gaussian 16 Rev. C.01*, Wallingford, CT, 2016.

11. Becke, A. D., Density-Functional Exchange-Energy Approximation with Correct Asymptotic-Behavior. *Phys. Rev. A* **1988,** *38* (6), 3098-3100.

12. Yanai, T.; Tew, D. P.; Handy, N. C., A new hybrid exchange–correlation functional using the Coulomb-attenuating method (CAM-B3LYP). *Chemical Physics Letters* **2004,** *393* (1-3), 51-57.

13. Chai, J.-D.; Head-Gordon, M., Long-range corrected hybrid density functionals with damped atom–atom dispersion corrections. *Physical Chemistry Chemical Physics* **2008,** *10* (44), 6615-6620.

14. Weigend, F.; Ahlrichs, R., Balanced Basis Sets of Split Valence, Triple Zeta Valence and Quadruple Zeta Valence Quality for H to Rn: Design and Assessment of Accuracy. *Phys. Chem. Chem. Phys.* **2005,** *7* (18), 3297-3305.

15. Scolaro., L. M.; Castriciano., M.; Romeo., A.; Patane., S.; Cefali., E.; Allegrini., M., Aggregation Behavior of Protoporphyrin IX in Aqueous Solutions: Clear Evidence of Vesicle Formation. *J. Phys. Chem. B* **2002,** (106), 2453-2459.

Chapter 3 Nitrophenolates, a 'simple' model system

This chapter has been adapted from Ref.[1] with permission from the PCCP Owner Societies.

3.1 Introduction

The phenolate moiety is a chemical structure observed in many biochromophores such as the chromophore of the Photoactive Yellow Protein,[2] Luciferase,[3] Rhodopsin,[4] and Green Fluorescent Protein,[5] to name a few. Nitrophenolates (NPs) serve as a small model system for phenolate containing chromophores, as well as charge-transfer chromophores,[6] and can exist as one of three isomers shown in Figure 3.1. Exciting these chromophores with visible irradiation causes a transfer of electron density from the negatively charged phenolate group to the nitro group.[7] These molecules are small enough that quantum chemical calculations are expected to be straightforward and NPs provide an interesting opportunity to investigate substitution effects on the electronic behavior. The combination of these two features, along with others, has garnered NPs a lot of attention in the literature.[8-17]

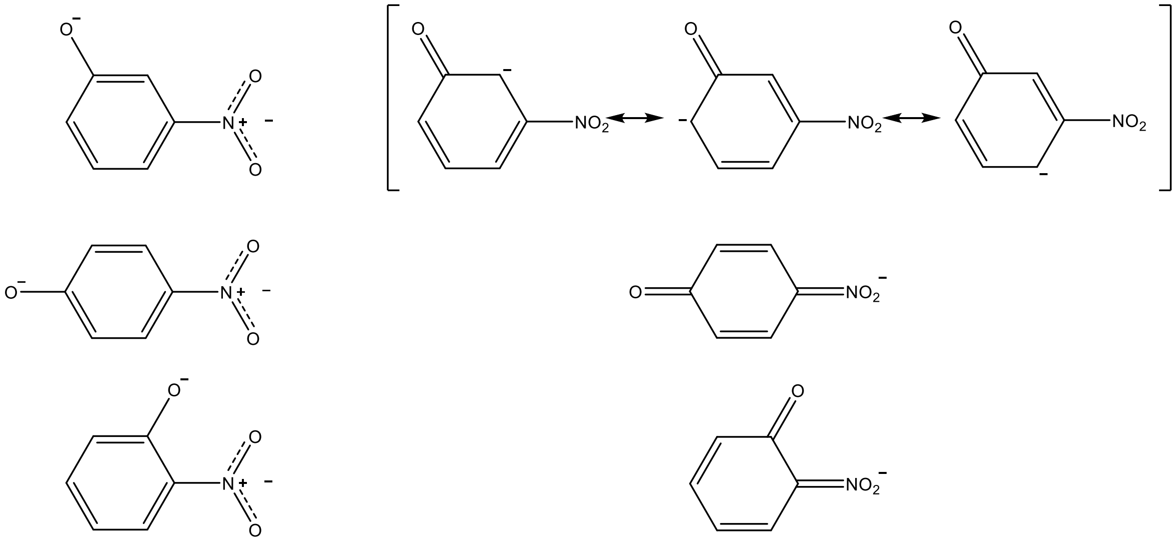

Figure 3.1. Structures and resonances of *meta*, *para*, and *ortho* isomers of NP, adapted from Wanko *et al*.[10]

Much of what is known about NPs comes from solution phase experiments. One key observation is that the substitution position has a drastic effect on the excited state dynamics. This was shown in a recent study by Michenfelder et al.[17] where they observed that *o*- and *p*-NP have much shorter excited state lifetimes than *m*-NP (300 fs compared to 5 ps). The nature of the solvent also had a pronounced effect on these lifetimes, and they were generally shorter in aqueous solution than in organic solvents.

NPs have been investigated *in vacuo* as well, specifically by Brøndsted Nielsen and coworkers.[8-11, 13-14, 16] They observed excitation energies of the S_1 state of *p*- and *o*-NP to be significantly to the blue of the excitation energy of *m*-NP. This difference can be explained through resonance stabilization arguments.[10] Their experiments were carried out at room temperature, and so the spectra are largely unresolved, leaving key details about the excited state electronic structure and dynamics unanswered. In this chapter, we present the electronic photodissociation spectra in the S_1 region for *o*-, *p*-, and *m*-NP at cryogenic temperatures, showing that the spectra of *o*- and *p*-NP remain broad, but *m*-NP exhibits an extended and assignable vibronic progression.

3.2 Computational

Several theoretical approaches have been taken in the literature to describe the electronic spectra of NPs. These include MP2 geometry optimizations of the ground state, with vertical excited state energies calculated from the optimized ground state geometry.[8-10] CC2 and TD-DFT calculations have been used to calculate vertical excitation energies and achieved reasonable agreement with experiments.[13] However, diagnostics in these CC2 calculations revealed that NP anions have multi-reference character. This makes the use of any single-reference method problematic. Despite this, the CC2 calculations compare favorably with SORCI vertical excitation energies.[10]

In this experiment, we sought to compare a Franck-Condon (FC) simulation with the experimental UV-Vis spectrum to assign observed vibronic transitions and assess broadening mechanisms. Performing a FC calculation requires optimized geometries for both the ground and excited state (S_1 in this case) as well as harmonic vibrational frequency calculations. We also required vertical excitation energy calculations. These calculations would be computationally demanding using multi-reference methods, and so we employed DFT methods instead. This of course means the accuracy of our computational results may suffer. We used the range-separated hybrid functional CAM-B3LYP as it has recently been used by Panja, *et al.* to evaluate the UV/vis absorption spectra of substituted NPs, where they found good agreement between the experimental spectra and the values obtained using CAM-B3LYP.[15]

3.3 Results and discussion

3.3.1 Overview

Figure 3.2 shows the electronic spectra in the S_1 region for all 3 isomers of NP, acquired at a trap temperature of 30 K. These spectra represent the two-photon induced loss of a neutral NO group as observed previously by others.[8-11, 13-14] Despite being taken at cryogenic temperatures, the spectra of *o*- and *p*-NP remain broad with no resolved features and onsets at 20500 and 22450 cm^{-1}, respectively. At first glance, the spectrum of *m*-NP appears to be noisy, but this is vibronic structure, with an onset beginning at *ca.* 16000 cm^{-1}, which will be discussed in detail in section 3.3.3. Table 3.1 compares the calculated and experimental values of electronic properties for all three isomers.

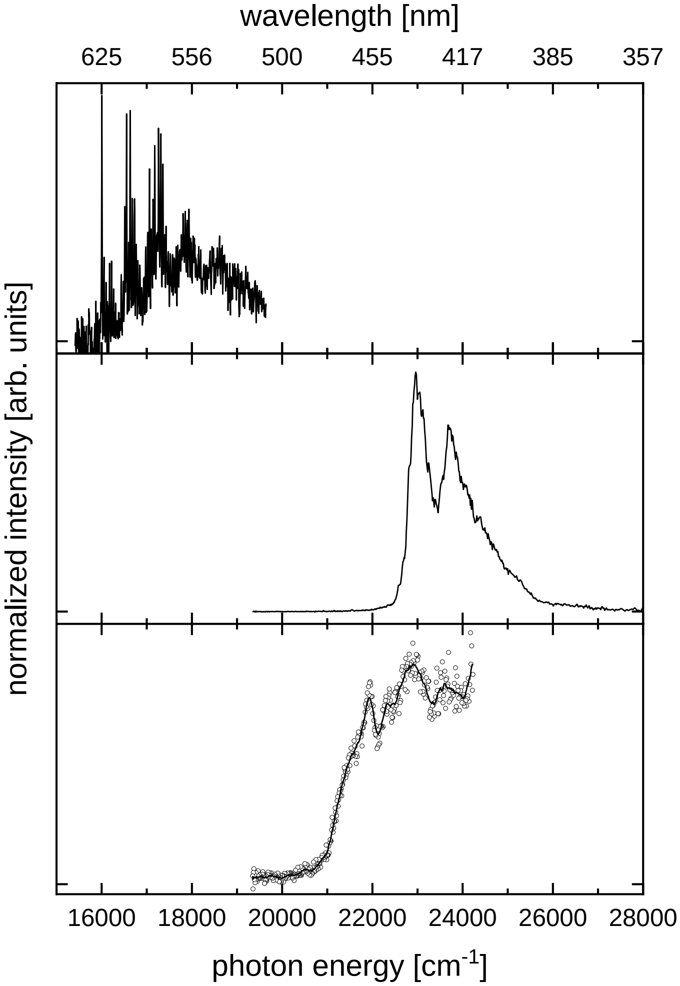

Figure 3.2. Electronic spectra showing the S_1 transition for *m*-, *p*-, and *o*-NP with a trap temperature of 30 K. In the traces of *m*- (top) and *p*-NP (middle), full lines connect the data points. In the case of *o*-NP, the data points are shown as open circles with a full line representing a 15-point gliding average to guide the eye.

Table 3.1. Calculated S_1 and S_2 properties (vertical excitation energies, band origins, and oscillator strengths) compared with experimental data. Calculations shown here were performed with the CAM-B3LYP functional and aug-cc-pVDZ basis set. Transitions are given in cm^{-1}.

	m-NP	*p*-NP	*o*-NP
Experimental onset[a]	16003	22450	20500
Experimental vertical transition	17300	22960	23000
Calculated S_1 properties			
Adiabatic transition energy[b]	15849	18497	17604
Vertical transition energy	18761	28772	27130
Oscillator strength	0.0268	0.5048	0.2033
Orbitals (contribution)	HOMO → LUMO	HOMO → LUMO	HOMO → LUMO+2
Calculated S_2 properties			
Adiabatic transition energy[b]	N/A [c]	N/A [c]	21700
Vertical S_2 (calc.)	27540	30980	26963
S_2 oscillator strength (calc.)	0.0000	0.0000	0.0001

[a] For *m*-NP, this entry is the energy of the 0_0^0 band; for *p*- and *o*-NP, the onset of the spectrum is listed

[b] Values have been corrected for zero-point energies.

[c] Adiabatic excitation energies for *m*- and *p*-NP were not calculated in the present work.

The difference in absorption energies has been explained previously by Brøndsted Nielsen and coworkers,[10] using resonance arguments. The ground state structures of the *o*- and *p*- isomers can both be described with a low-lying charge transfer resonance, where the charge transfer state places a formal negative charge on the nitro group. The analogous charge transfer resonance is energetically unfavorable for *m*-NP isomer, as seen in Figure 3.1. This leads to ground state stabilization in *o*- and *p*-NP which causes an increase in the $S_0 \rightarrow S_1$ gap, pushing their absorptions to higher energy. The individual spectra will be discussed in the following sections.

3.3.2 *para*-Nitrophenolate

The spectrum of *p*-NP shown in Figure 3.3 shows an onset at 22450 which peaks at 22960 cm^{-1} and is followed by a second feature at *ca*. 23690 cm^{-1}. There is some additional structure, most clearly seen on the first peak, consisting of shoulders spaced by 100-130 cm^{-1}, but otherwise the absorption features are broad and unresolved. Excited state calculations place the vertical excitation energy at 28772 cm^{-1}, about 6000 cm^{-1} higher than experiment, and give an oscillator strength of 0.5048 which is the highest of the three isomers.

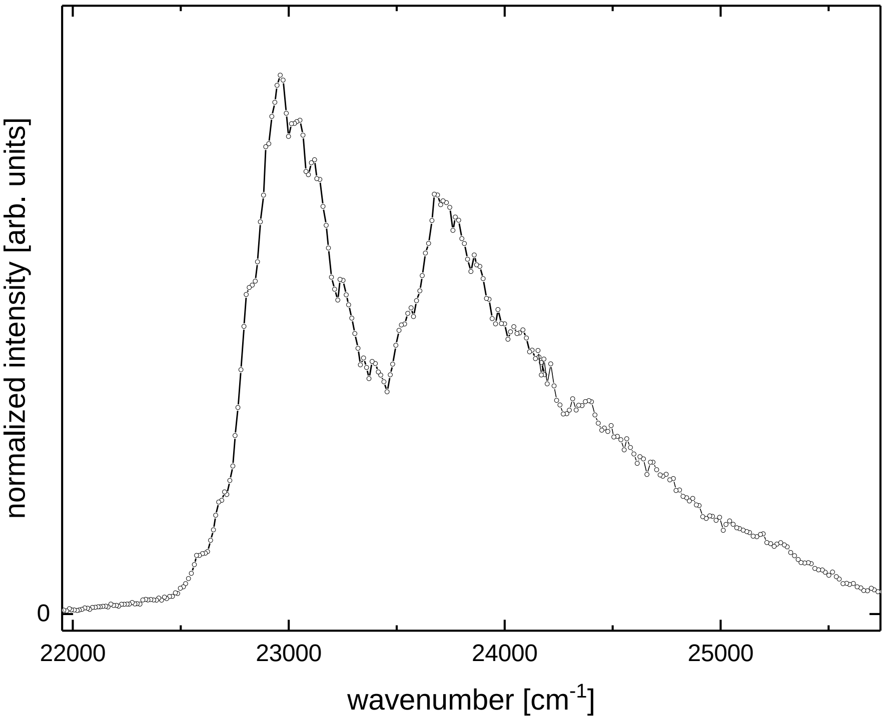

Figure 3.3. Electronic spectrum of *p*-NP in the band origin region.

Calculations on the ground and excited states of this isomer revealed large changes in the minimum energy geometry between the two states, which are predominantly localized on the nitro group of the molecule. The molecule has a planar ground state, but the minimum energy geometry in the excited state is realized by twisting the nitro group around the CN bond by 90°, and pyramidalizing the nitrogen to more closely resemble an sp^3 hybridization, rather than sp^2. Figure 3.4 shows the potential energy surfaces of S_0 and S_1 in the Franck-Condon (FC) region. The ground state minimum energy geometry is a saddle point on the excited state surface, *ca*. 9300 cm^{-1} above the minimum of the S_1 state. This means that a vertical excitation of the molecule will be exciting into highly excited vibrational motion in both the nitro torsion and pyramidalization coordinates, and thus there will be a large density of states in these vibrational modes, which can both be expected to be FC active. This large density of states high above the band origin results in significant spectral congestion, this effect is clearly demonstrated in the spectrum of *m*-NP which is discussed in section 3.3.4.

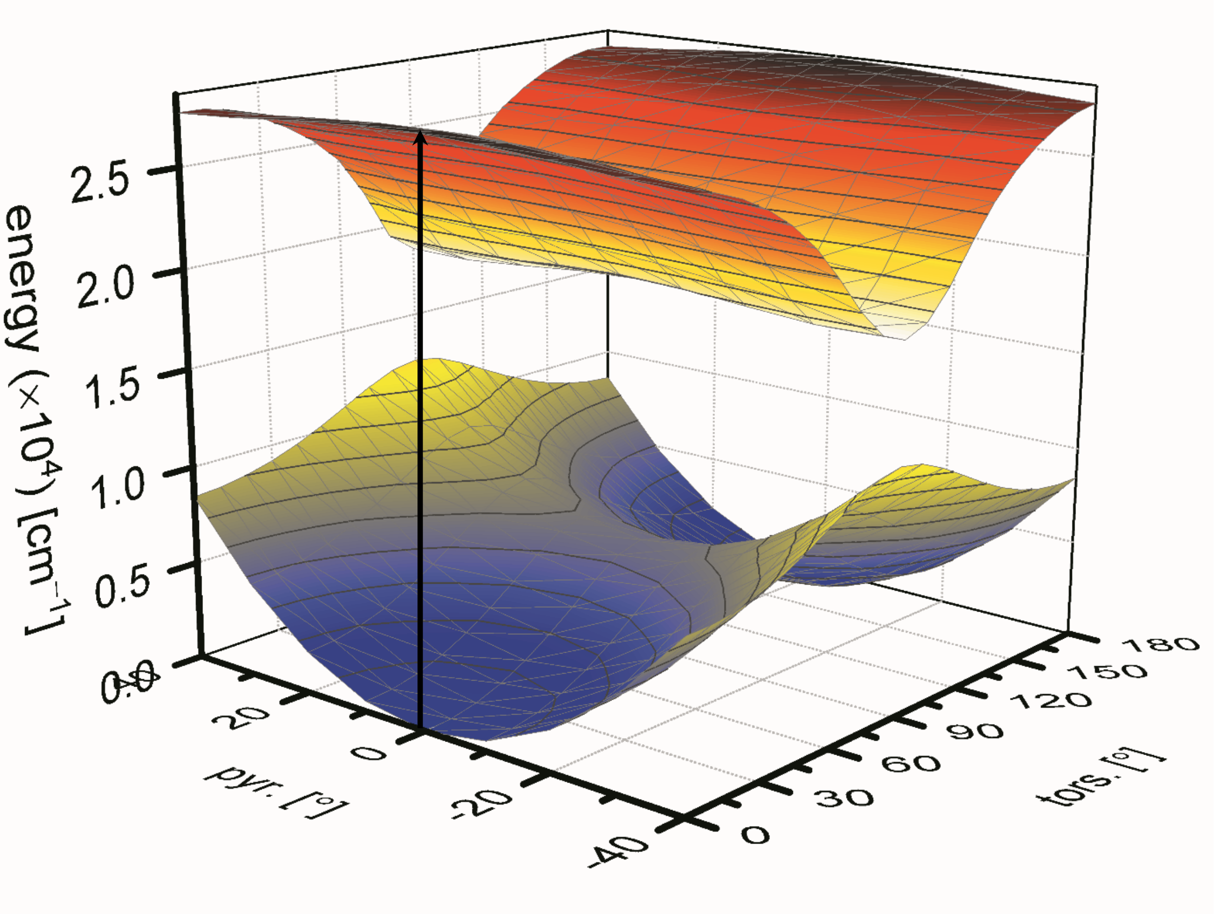

Figure 3.4. Potential energy surface of the S_0 and S_1 states in the FC region of *p*-NP. The black arrow indicates a vertical excitation. Calculations for the surface were performed at the CAM-B3LYP/aug-ccpVDZ level of theory using a relaxed scan over the nitro torsion (tors.) and pyramidalization (pyr.) coordinates.

The potential energy surface sheds some light on why the spectrum remains unresolved at low temperatures. Exciting into a high density of vibrational states in both the torsion and pyramidalization modes (as well as any state coupling to these modes) will lead to significant spectral congestion. The torsion mode is calculated to be 96 and 257 cm^{-1} in the S_0 and S_1 respectively. The difference of these frequencies is comparable with the observed experimental spacing of 100-130 cm^{-1} for the shoulders on the main absorption feature (see Figure 3.3). The difference for the pyramidalization modes is *ca*. 250 cm^{-1} which does not match the experimental spacing. As mentioned before, the excited state lifetime of *p*-NP has been measured by Michenfelder *et al.* to be 300 fs,[17] which leads to lifetime broadening of *ca*. 18 cm^{-1}. This broadening combined with a high density of vibrational states on the S_1 surface provides a plausible explanation for the lack of resolved features in the electronic spectrum. Michenfelder *et al*. also invoked a conical intersection coupling S_1 and S_0 along the nitro torsion mode as the mechanism of relaxation.[17] Neither our calculations nor theirs were able to corroborate the existence of this conical intersection, but both should only be taken as qualitative.

3.3.3 *ortho*-Nitrophenolate

Like *p*-NP, *o*-NP has a broad electronic spectrum in the S_1 region, despite being taken at cryogenic temperatures. The spectrum has an onset at *ca*. 20500 cm^{-1} and a set of peaks at 21930, 23000, 23600, and 24200 cm^{-1}. We observe no regular features that could be assigned to specific vibrational transitions. The vertical excitation is calculated to be 27130 cm^{-1}, well above the experimental features as was also observed in *p*-NP. Excited state calculations reveal that there are two close-lying electronic states in the FC region with a calculated separation of 167 cm^{-1} (see Figure 3.5).

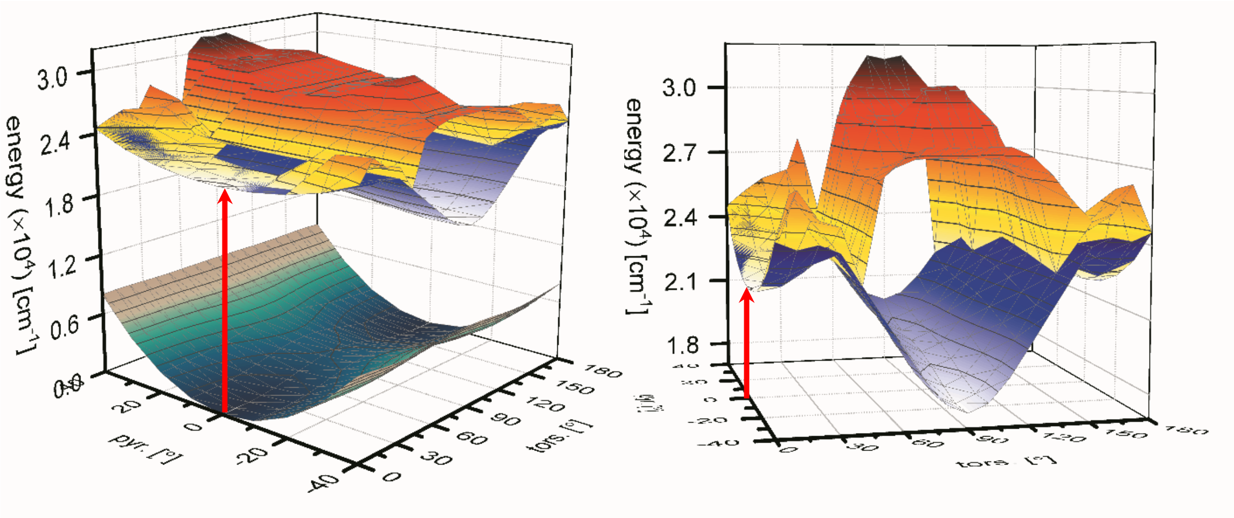

Figure 3.5. Potential energy surface of the S_0, S_1, and S_2 states in the FC region of *o*-NP. The red arrow indicates a vertical excitation. Calculations were performed at the same level as for *p*-NP.

Geometry optimizations of the excited states shows that the S_1 state has a similar minimum energy geometry to that of *p*-NP with a rotated and pyramidalized nitro group. The S_2 state has a minimum energy geometry that is planar like the ground state and the calculations place its potential energy surface energetically below the S_1 state in the FC region. The two electronic states being in such proximity in the FC region suggests they may mix, and there may be a conical intersection in this region between the two. We note that these calculations should be taken as qualitative at best due to the low level of theory and the multireference character of the system. In the absence of the S_1 state, vertical excitation into the S_2 state may have had well-structured vibronic features. However, excitation into the S_1 state should have a similarly congested spectrum to that of *p*-NP due to the high density of vibrational excitation in the S_1 state. Also, like *p*-NP, *o*-NP has an excited state lifetime of 300 fs. The combination of these two sources of congestion with the additional congestion due to S_1/S_2 mixing makes deeper analysis of the experimental spectrum unfeasible.

3.3.4 *meta*-Nitrophenolate

Unlike *p*- and *o*-NP, the band origin region of *m*-NP contains sharp, assignable vibronic features. The band origin (excitation between the vibrational ground states of the ground and first excited electronic states) occurs at 16003 cm^{-1} (0_0^0). In the remainder of this work, we denote transitions by $Q_{\nu"}^{\nu'}$, where Q is the label of the vibrational mode numbered in order of increasing vibrational frequency in the S_1 state, and ν” and ν’ are the numbers of quanta in mode Q of the lower and upper electronic states, respectively.

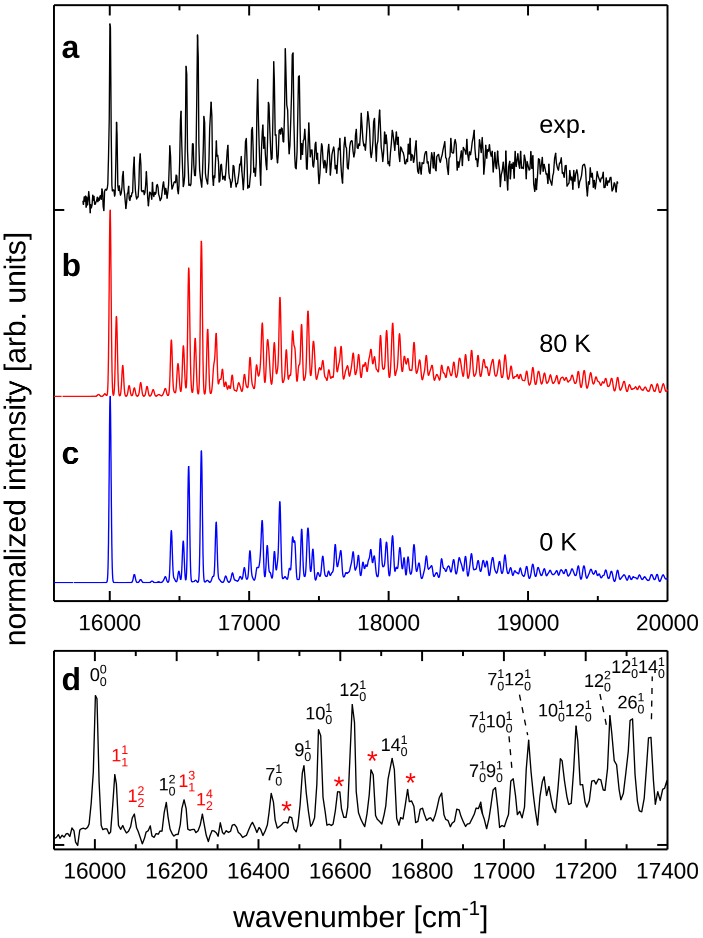

Figure 3.6. The top panel contains the experimental electronic spectrum in the band origin region of *m*-NP (a), compared to FC simulations at 80 (b) and 0 K (c) which have been shifted match the experimental band origin. The lower panel contains only the first 2400 cm^{-1} above the band origin, along with assignments of selected peaks (d); a more extensive assignment is given in Table 3.2. Hot bands are marked in red, with red asterisks labeling peaks whose primary contribution comes from a hot band with one quantum in the nitro torsion vibration.

The vibronic bands in the experimental spectrum shown in Figure 3.6 (a) exhibit a regular spacing of *ca*. 45 cm^{-1} near the band origin and throughout the band envelope. There are several regions of high signal intensity, spaced by 620-640 cm^{-1}, and extending to the end of the measured region (*ca*. 3500 cm^{-1}). Although the vibronic features are sharp, the photodissociation signal does not return to baseline in between peaks, indicating increasing spectral congestion.

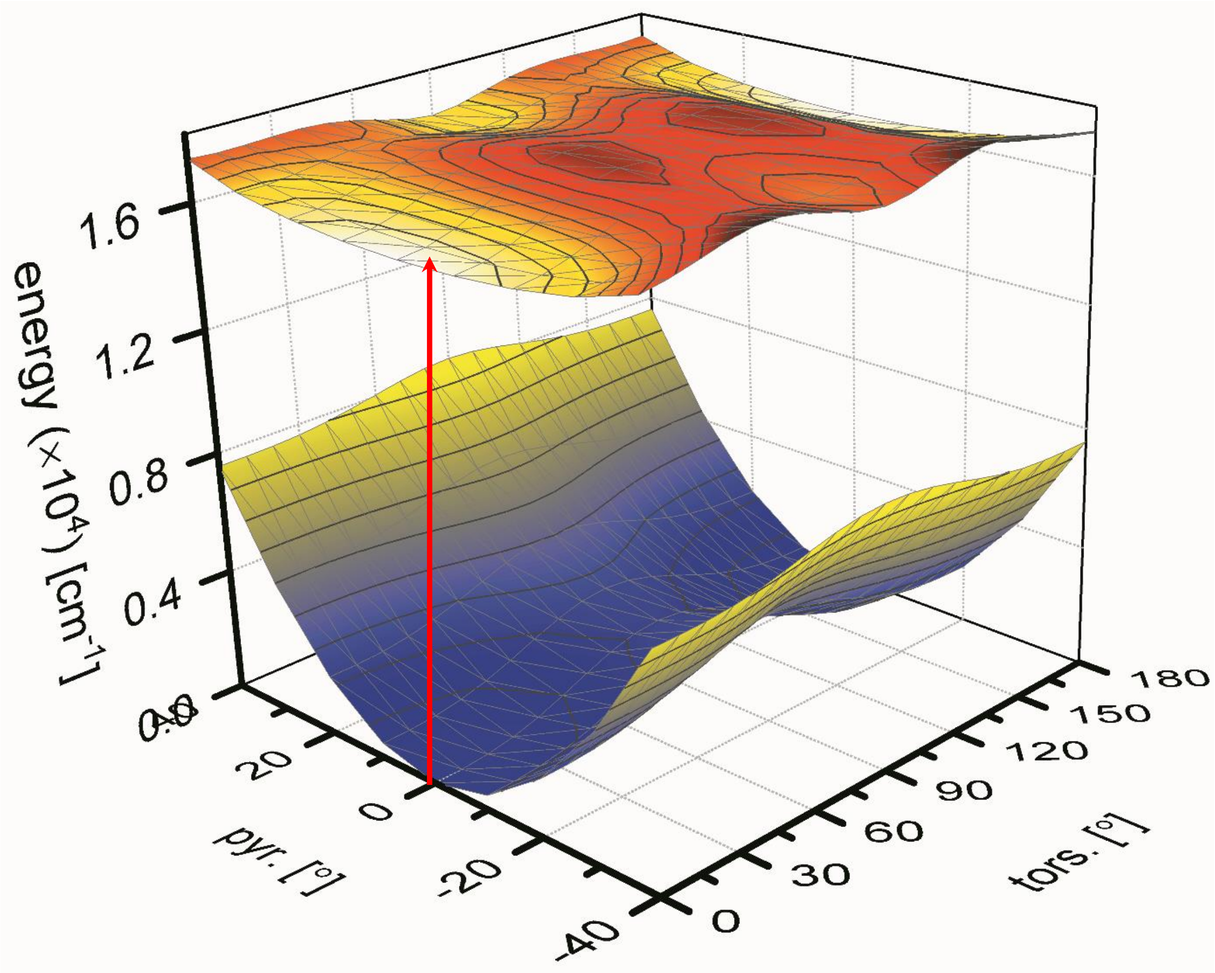

Figure 3.7. Potential energy surface of the S_0 and S_1 states in the FC region of *m*-NP. The red arrow indicates a vertical excitation. Calculations were performed at the same level as for *p*-NP.

The minimum energy geometry of *m*-NP is calculated to be planar in both the ground and excited state (see Figure 3.7). The vertical transition energy is calculated at 18761 cm^{-1} which is too high, but still within the experimental band. The calculated band origin is at 15849 cm^{-1} which is close to the experimental value, but this is likely fortuitous. The largest geometry changes that occur upon excitation are a 3% decrease in the CN and a 4% increase in the NO bond length. Typical values for stretching frequencies of modes involving these bonds are greater than 1000 cm^{-1}, inconsistent with the spacing of the vibrational features. The mode assignments in Figure 3.6 are from FC simulations based on harmonic wave functions. A more extensive summary is given in Table 3.2. Overall, the simulation at 80 K qualitatively recovers the experimental spectrum. This temperature is significantly higher than the experimental trap temperature of 30 K, an observation which will be discussed following the assignment of the spectrum.

The FC simulation at 80 K produces hot bands in the nitro torsion mode, ω_1, which is the lowest frequency mode in both the ground and excited electronic states, with harmonic frequencies of 41 and 77 cm^{-1}, respectively. This mode, however, is significantly anharmonic (see Figure 3.8). It can be described as a hindered internal rotor around the CN bond axis, with an 1890 cm^{-1} barrier at 90º in the S_0 state, while in the S_1 state there is a local minimum at this rotation angle, 1400 cm^{-1} above the planar geometry. The excited state torsion frequency was set to 87 cm^{-1} in the FC simulations to optimize the agreement with experiment. Every transition belonging to a principal FC active mode is accompanied hot hands on the high energy side, originating from thermally populated levels in S_0 with one or two quanta in ω_1.

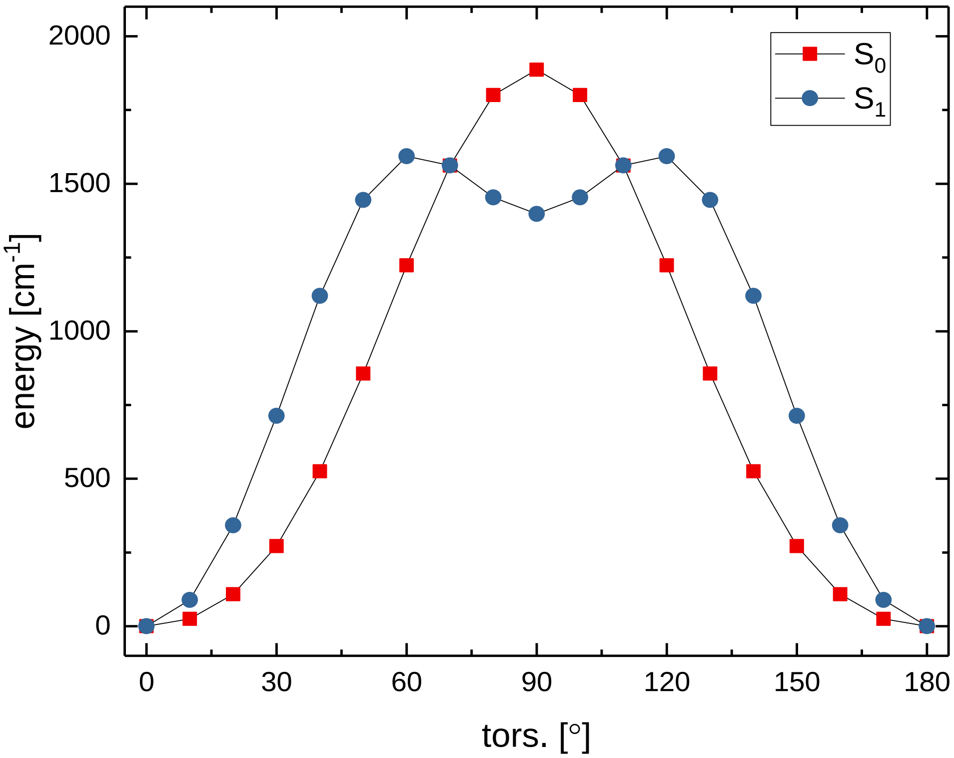

Figure 3.8. Potential energy scans of *m*-NP along the torsion (tors.) coordinate of the S_0 and S_1 states using CAM-B3LYP/aug-cc-pVDZ and a NO_2 pyramidalization angle constrained to zero (corresponding to a planar nitro group). Energies are given relative to the minimum energy structure for each surface, in cm^{-1}.

The simulation at 0 K provides a straightforward assignment of the principal FC active modes. The first feature we assign is due to the overtone of the nitro torsion mode, 1_0^2 (transitions with odd Δv are forbidden by symmetry), which coincides with the onset of features at 16175 cm^{-1}. The next set of FC active modes are a set of intense peaks between 16390 and 16910 cm^{-1}. The first peak, at 16434 cm^{-1}, we assign to 7_0^1 where ω_7 is characterized as an in-plane phenolate bending motion coupled with an in-plane nitro wagging motion, as well as a ring deformation. Next, we assign the 9_0^1 (in-plane phenolate bending and ring deformation), 10_0^1 (ring deformation), 12_0^1 and 14_0^1 (both of which are ring deformation and nitro scissoring modes)

modes. Modes belonging to the group of transitions in the spectral region close to the band origin will be referred to as group 1 modes.

Group 2 transitions will refer to modes with fundamental transitions in the region of 16900-17590 cm^{-1} which also contains second order combination bands of ω_7, ω_9, ω_{10}, ω_{12}, and ω_{14}, as well as overtones of ω_{10} and ω_{12} ($\Delta v = 2$). Other overtones are assignable but are weaker. Additionally, transitions involving CN/NO_2 stretching motions (ω_{26}, ω_{28}, and ω_{31}) appear in this region of the spectrum. The third region of high intensity (*ca*. 18000 cm^{-1}) is comprised of second order combination bands of group 1 modes with group 2 modes, as well as third order combination bands of group 1 modes (see Table 3.2). Above this region, the spectrum becomes too congested to assign. This is not an unexpected result, as excitation in this region will result in vibrational levels that are above the calculated barrier in the torsional potential energy curve (see Figure 3.8). Thus, the corresponding density of vibrational states, along with coupling effects between vibrational modes, will result in a high degree of spectral congestion, corroborating the interpretation of the spectral congestion in the spectra of *p*- and *o*-NP.

The features in the vibronic progression of *m*-NP have a linewidth we can cleanly determine (average FWHM for the first ten well-resolved lines of 10.4 ± 1.2 cm^{-1}), which allows a rough estimate of a lower limit for the excited state lifetime. We performed a simulation using the PGOPHER program[18] and rotational constants obtained through our electronic structure calculations to obtain an expected width of the rotational envelope of 8 cm^{-1} (individual rotational lines are not resolved). Convoluting the bandwidth of our light source (5 cm^{-1}) with the result from PGOPHER leads to an expected linewidth of 9.4 cm^{-1}. Assuming the width is due to lifetime broadening, a lifetime of *ca*. 1200 fs is compatible with the observed 10.4 cm^{-1} linewidth and this value is in the range observed for *m*-NP in recent ultrafast experiments.[17] Our result is, of course, crude, but we note that the longer lifetimes reported by Michenfelder *et al*. from ultrafast spectroscopy experiments were measured in nonpolar solvents (5000 fs). We would expect the absence of solvent molecules to be more comparable with the nonpolar environment and therefore our estimate of 1200 fs as a lower limit for the S_1 lifetime is in rough agreement with the ultrafast experiments.

Table 3.2. List of calculated harmonic vibrational frequencies (cm^{-1}) and symmetries for *o*-, *m*-, and *p*-NP. Note that the point group is C_s for *o*- and *m*-NP in both the X (ground) and A (excited) state. For *p*-NP, the X state belongs to C_{2v}, while the A state belongs to C_s.

	o-NP				*m*-NP				*p*-NP			
Mode	X		A		X		A		X		A	
1	18.30	A"	41.89	A"	41.45	A"	76.95	A"	95.84	A_2	88.66	A"
2	107.85	A"	133.33	A"	169.14	A"	150.68	A"	103.56	B_1	178.59	A"
3	232.88	A"	152.85	A'	191.49	A"	213.41	A"	235.67	B_2	195.32	A'
4	253.02	A'	243.41	A"	228.67	A'	219.36	A'	258.73	B_1	257.46	A"
5	381.73	A'	337.54	A'	387.09	A'	246.72	A"	369.92	A_1	342.62	A'
6	429.30	A'	385.02	A"	439.62	A'	384.46	A'	439.32	A_2	373.87	A"
7	438.88	A"	456.38	A'	452.86	A"	439.41	A'	451.21	B_2	449.46	A'
8	546.34	A"	533.96	A"	526.84	A'	443.86	A"	487.26	B_1	526.02	A"
9	565.75	A'	551.90	A'	563.49	A'	524.99	A'	551.72	B_2	546.87	A'
10	572.62	A'	636.22	A'	571.67	A"	563.57	A'	635.38	B_2	586.49	A'
11	662.60	A'	642.78	A"	683.07	A'	578.51	A"	648.04	A_1	638.26	A'
12	723.45	A"	673.86	A'	693.17	A"	654.18	A'	731.44	B_1	684.33	A"
13	750.86	A"	761.27	A"	730.67	A"	690.02	A"	801.08	B_1	772.77	A'
14	810.20	A"	783.74	A"	804.41	A"	760.99	A'	801.17	A_2	785.47	A"
15	825.06	A'	804.02	A'	843.22	A'	792.14	A"	822.78	A_1	830.39	A'
16	870.95	A"	857.18	A'	876.43	A"	880.08	A"	859.05	A_1	891.18	A"
17	893.67	A'	873.30	A"	902.22	A"	920.26	A'	883.99	B_1	983.00	A"
18	989.44	A"	959.42	A"	941.83	A'	944.17	A"	994.96	A_1	994.74	A'
19	998.41	A"	988.95	A"	982.56	A"	992.64	A"	1002.07	B_1	1005.41	A"
20	1037.80	A'	1075.13	A'	999.61	A'	996.77	A'	1002.50	A_2	1106.33	A'
21	1088.28	A'	1098.15	A'	1086.55	A'	1067.83	A'	1104.90	B_2	1121.61	A'
22	1146.37	A'	1163.38	A'	1094.06	A'	1077.58	A'	1138.07	A_1	1174.08	A'
23	1169.23	A'	1169.50	A'	1159.89	A'	1149.67	A'	1204.68	A_1	1248.25	A"
24	1241.75	A'	1260.46	A'	1256.62	A'	1240.35	A'	1271.77	B_2	1276.04	A'
25	1306.43	A'	1287.42	A'	1314.93	A'	1307.92	A'	1333.94	B_2	1318.99	A'
26	1379.71	A'	1344.05	A"	1400.13	A'	1374.15	A'	1371.93	A_1	1349.64	A"
27	1407.01	A'	1360.85	A'	1425.16	A'	1424.24	A'	1429.24	A_1	1387.72	A'
28	1495.56	A'	1389.56	A'	1498.42	A'	1454.57	A'	1501.01	B_2	1490.38	A'
29	1540.07	A'	1440.25	A'	1572.31	A'	1489.5	A'	1544.21	B_2	1500.70	A'
30	1581.74	A'	1559.89	A'	1578.25	A'	1524.57	A'	1591.06	B_2	1548.00	A'
31	1639.01	A'	1651.33	A'	1616.85	A'	1613.77	A'	1619.21	A_1	1628.51	A'
32	1691.94	A'	1693.12	A'	1669.72	A'	1647.13	A'	1674.01	A_1	1680.80	A'
33	3152.44	A'	3180.48	A'	3158.84	A'	3179.16	A'	3191.61	B_2	3204.36	A'
34	3194.28	A'	3201.21	A'	3189.66	A'	3217.54	A'	3192.30	A_1	3204.91	A'
35	3200.83	A'	3219.28	A'	3248.6	A'	3261.33	A'	3228.38	B_2	3224.74	A'

3.3.5 Ion temperature estimation

As mentioned before, the trap temperature in the experiment was 30 K, but the best agreement between the simulation and experiment is with a simulation temperature of 80 K. To explore this discrepancy in more detail, we performed a series of experiments to measure the temperature-dependence of the spectrum of *m*-NP close to the S_1 band origin over the experimental temperature range of 30-124 K. Figure 3.9 shows the band origin region and group 1 modes of the resulting spectra normalized to the peak absorption of the band origin. As the temperature of the ions increases, the intensity of the hot bands relative to the band origin should also increase. This can be used to extract an estimate of the ion temperature, assuming the FC factors and vibrational energies of the relevant bands are known.

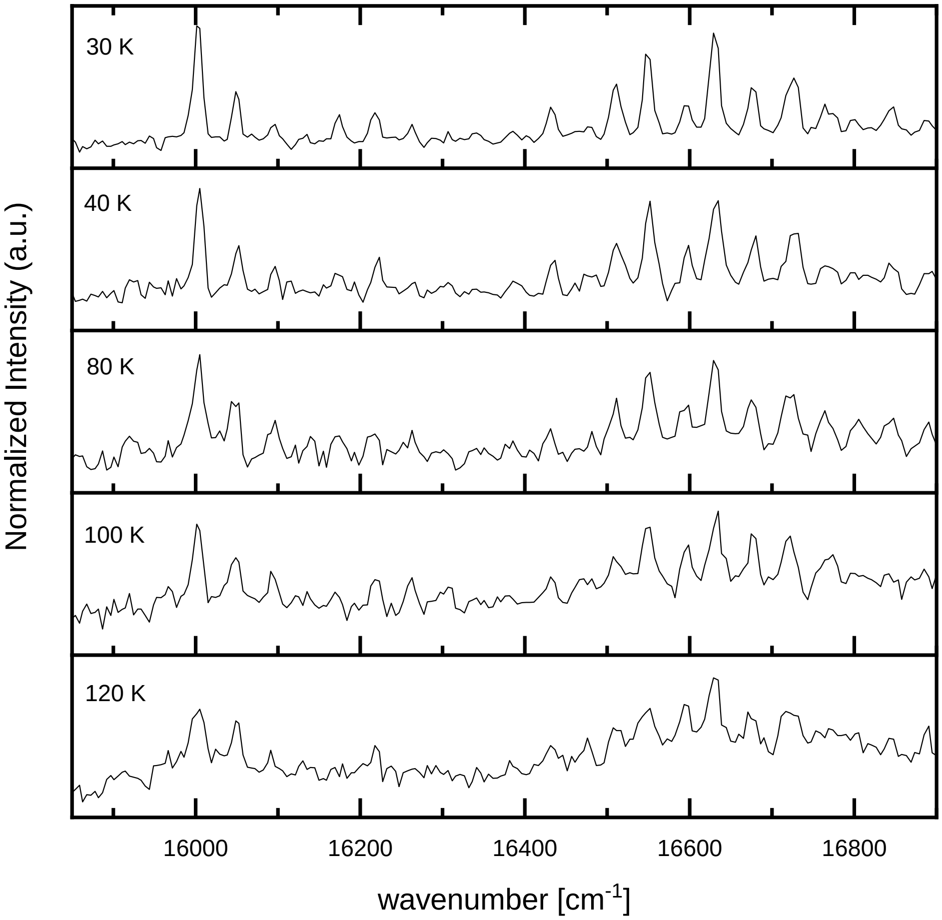

Figure 3.9. Temperature dependent spectra of *m*-NP in the band origin region. Spectra have been normalized to the peak absorption of the band origin at 16003 cm^{-1}.

The ratio of intensities of a hot band, I_1 to the origin band, I_{0-0} is equal to:

$$\frac{I_1}{I_{0-0}} = \frac{|\langle \phi_1'' | \phi_1' \rangle|^2 e^{-E_1/kT}}{|\langle \phi_{0-0}'' | \phi_{0-0}' \rangle|^2}$$

where $\langle \phi_1'' | \phi_1' \rangle$ is the FC overlap, E_1 is the vibrational energy of the vibrational level in the electronic ground state which gives rise to the hot band, and T is the temperature of the ion. This can be rearranged to yield:

$$T = \frac{-E_1/k}{ln\left(\frac{I_1}{I_{0-0}}\right) - ln\left(\frac{|\langle\phi_1''|\phi_1'\rangle|^2}{|\langle\phi_{0-0}''|\phi_{0-0}'\rangle|^2}\right)}$$

where the right-hand side can be plotted against the experimental trap temperature and should result in a straight line. The trap temperature will not be the same as the ion temperature, $T = T_{meas} + T_{corr}$, where T_{meas} is the measured temperature of the ion trap, and T_{corr} is an additive correction term. Plotting the last equation as a function of T_{meas} produces a y-intercept of T_{corr}. The values for E and ϕ are taken from the FC simulations.

We evaluated the temperature correction term T_{corr} for the lowest two energy hot bands, 1_1^1 and 1_2^2, at 16051 and 16097 cm^{-1}, respectively. The excited state torsion frequency was set to 87 cm^{-1} as mentioned above. Each data set was fitted with a line with a fixed slope of one. For the 1_1^1 peak, T_{corr} = (35 $\pm$ 3) K, and for 1_2^2, T_{corr} = (37 $\pm$ 5) K. Therefore, data collected at a trap temperature of T_{meas} = 30 K are expected to represent the spectrum of ions with a temperature T = 30 + 36 K = (66 $\pm$ 5) K.

Radio frequency traps are known to cause heating by driving collisions between the buffer gas and trapped ions.[19-21] Additionally, the presence of residual buffer gas in the trap during extraction can lead to heating. Finally, it is possible that collisional cooling of the ions is incomplete after the storage time in the trap (95 ms in this experiment). None of these effects is easily quantified in our experiment due to the high sensitivity of the ion intensity on the relevant experimental parameters, and it is likely that they all contribute to the difference between ion temperature and trap temperature. The deviation between the ion temperature and the temperature of the optimal FC simulation is also influenced by computational parameters, such as choice of functional (using B3LYP instead of CAM-B3LYP yields a best-fit temperature of 150 K) and basis set, and the anharmonicity of the nitro torsion mode (ω_1). With these facts in mind, we conservatively assume that the ion temperature is in the range of 60-80 K. This estimate is in line with previous experiments at similar trap temperatures, where complexes of ions with N_2 molecules were formed and the temperature estimation was made based on the calculated binding energy of these adducts.[18]

3.3.5 Charge transfer character of NP excitations

All three of the NP isomers exhibit some degree of charge transfer character. Looking at the orbitals involved in the electronic transitions (see Figure 3.10), the charge transfer character is most apparent in *m*-NP. The HOMO has significant density on the phenolate oxygen whereas the LUMO has significant density on the nitro group. The extent charge transfer is less in the other two isomers, and their transitions are better described as primarily ππ* transitions. Charge transfer transitions generally have lower oscillator strengths, due to low overlap between the involved orbitals. The oscillator strength is lowest for the *m*-NP isomer, followed by that of *o*-NP, and *p*-NP which has the largest calculated S_1 oscillator strength of the three isomers.

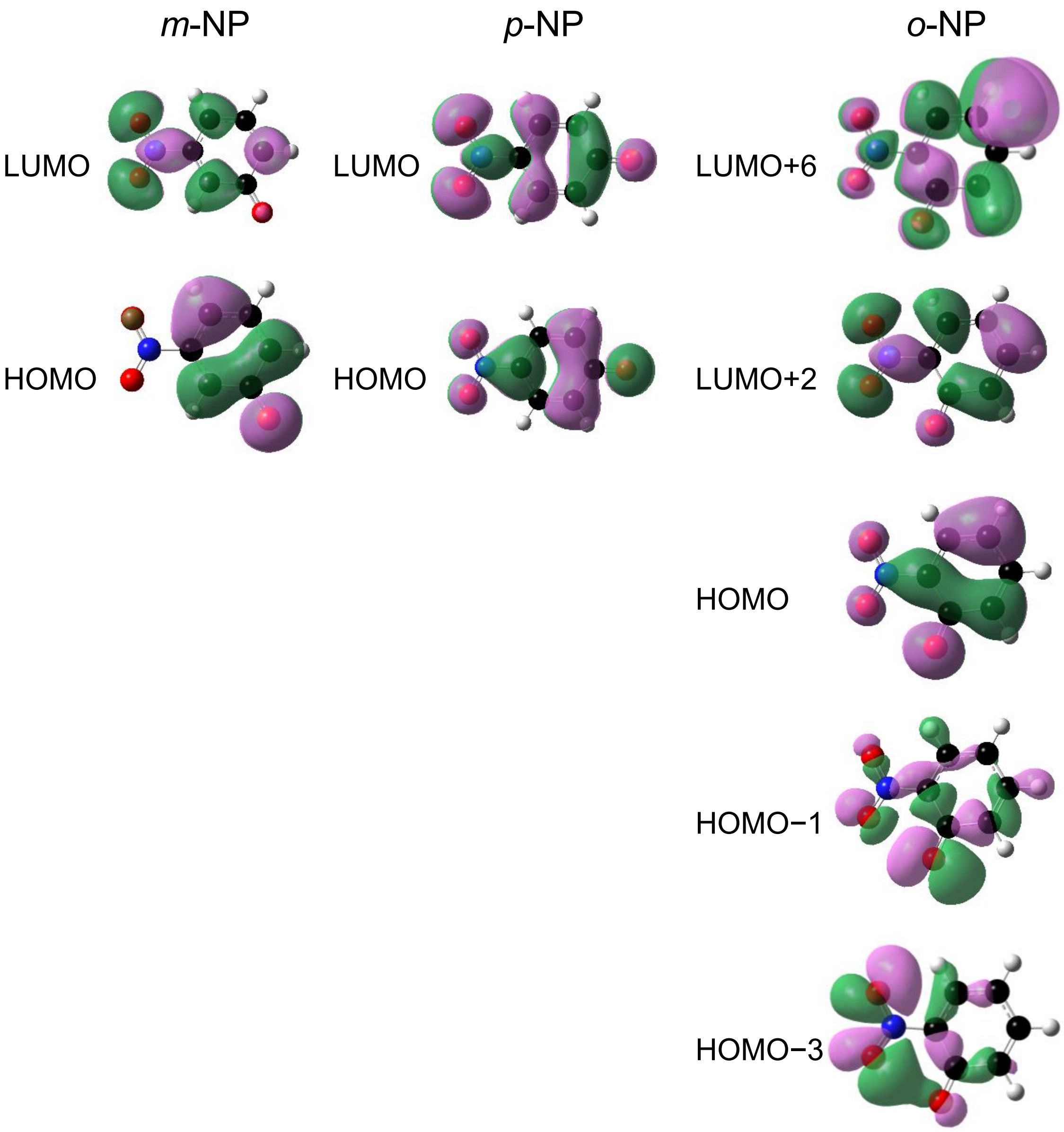

Figure 3.10. Frontier orbitals for *m*-, *p*-, and *o*-NP, calculated using CAM-B3LYP. Both *meta* and *para* isomers exhibit pure HOMO → LUMO transitions for $S_0 \rightarrow S_1$. The $S_0 \rightarrow S_1$ transition for *o*-NP is HOMO → LUMO+2, while the $S_0 \rightarrow S_2$ transition for *o*-NP is a mixture of HOMO−1 → LUMO+2, HOMO−1 → LUMO+6, and HOMO−3 → LUMO+2.

To make a more quantitative argument, we calculated the change in dipole moment upon excitation for each of the isomers as well as plotting electron density difference plots (Figure 3.11). The change in dipole moment was 7.5 D, 2.4 D, and 1.6 D for *m*-, *o*-, and *p*-NP respectively. The large change for the *meta* isomer is consistent with it having the most charge transfer character. The other two isomers exhibit changes which are significantly lower, consistent with their transitions having less charge transfer character.

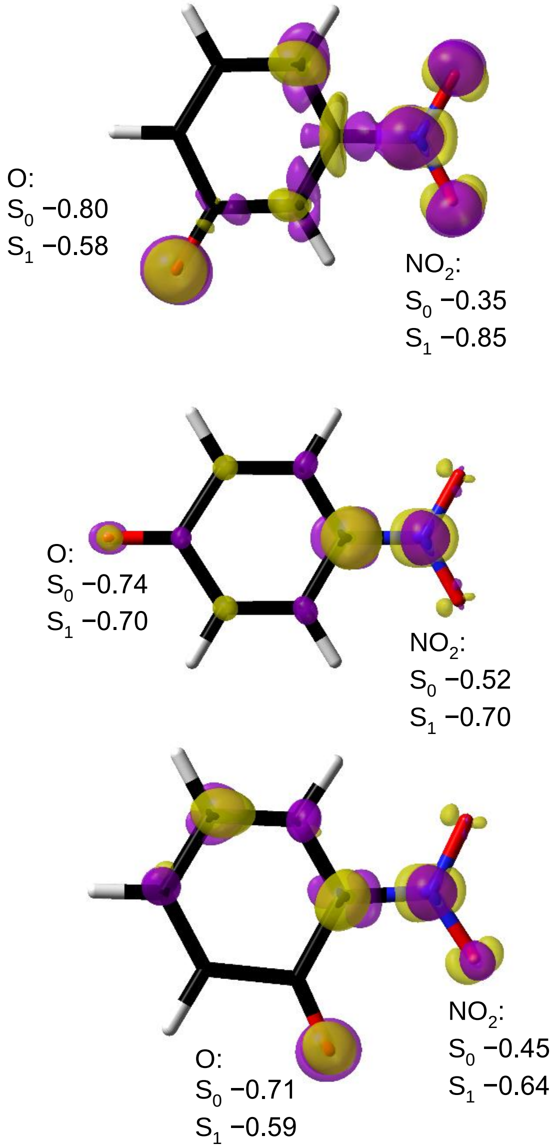

Figure 3.11. Electron density difference plots for *m*- (top), *p*- (center), and *o*-NP (bottom) in the FC region. Purple regions indicate an increase of electron density upon electronic transition, while yellow regions indicate a decrease of electron density upon electronic transition. The density difference for *o*-nitrophenolate was calculated for the S_1 state. Listed are the charges on the NO_2 and O groups for each isomer in the S_0 and S_1 states. Charges calculated using a Natural Population Analysis, given in e.

3.4 References

1. Dodson, L. G.; Zagorec-Marks, W.; Xu, S.; Smith, J. E. T.; Weber, J. M., Intrinsic photophysics of nitrophenolate ions studied by cryogenic ion spectroscopy. *Physical Chemistry Chemical Physics* **2018,** *20* (45), 28535-28543.
2. Borgstahl, G. E. O.; Williams, D. R.; Getzoff, E. D., 1.4 Å Structure of Photoactive Yellow Protein, a Cytosolic Photoreceptor: Unusual Fold, Active Site, and Chromophore. *Biochemistry* **1995,** *34* (19), 6278-6287.
3. Shimomura, O.; Johnson, F. H.; Masugi, T., Cypridina Bioluminescence: Light-Emitting Oxyluciferin-Luciferase Complex. *Science* **1969,** *164* (3885), 1299.
4. G. S. Harbinson, S. O. S., J. A. Pardoen, J. M. L. Courtin, J. Lugtenburg, J. Herzfeld, R. A. Mathies, R. G. Griffin, Solid-State C13 NMR Detection of a Perturbed 6-s-trans Chromophore in Bacteriorhodopsin. *Biochemistry* **1985,** *24*, 6955-6962.
5. Shimomura, O., Discovery of Green Fluorescent Protein (GFP) (Nobel Lecture). *Angewandte Chemie International Edition* **2009,** *48* (31), 5590-5602.
6. Grabowski, Z. R.; Rotkiewicz, K.; Rettig, W., Structural Changes Accompanying Intramolecular Electron Transfer: Focus on Twisted Intramolecular Charge-Transfer States and Structures. *Chemical Reviews* **2003,** *103* (10), 3899-4032.
7. Bureš, F., Fundamental Aspects of Property Tuning in Push–Pull Molecules. *RSC Advances* **2014,** *4* (102), 58826-58851.
8. Kirketerp, M.-B. S.; Petersen, M. Å.; Wanko, M.; Leal, L. A. E.; Zettergren, H.; Raymo, F. M.; Rubio, A.; Brøndsted Nielsen, M.; Brøndsted Nielsen, S., Absorption Spectra of 4-Nitrophenolate Ions Measured in Vacuo and in Solution. *ChemPhysChem* **2009,** *10* (8), 1207-1209.

9. Kirketerp, M. B. S.; Petersen, M. Å.; Wanko, M.; Zettergren, H.; Rubio, A.; Brøndsted Nielsen, M.; Brøndsted Nielsen, S., Double-Bond versus Triple-Bond Bridges: Does it Matter for the Charge-Transfer Absorption by Donor–Acceptor Chromophores? *ChemPhysChem* **2010,** *11* (12), 2495-2498.

10. Wanko, M.; Houmoller, J.; Stochkel, K.; Kirketerp, M.-B. S.; Petersen, M. Å.; Brøndsted Nielsen, M.; Brøndsted Nielsen, S.; Rubio, A., Substitution Effects on the Absorption Spectra of Nitrophenolate Isomers. *Physical Chemistry Chemical Physics* **2012,** *14* (37), 12905-12911.

11. Houmøller, J.; Wanko, M.; Støchkel, K.; Rubio, A.; Brøndsted Nielsen, S., On the Effect of a Single Solvent Molecule on the Charge-Transfer Band of a Donor–Acceptor Anion. *Journal of the American Chemical Society* **2013,** *135* (18), 6818-6821.

12. Kozłowska, J.; Wielgus, M.; Bartkowiak, W., TD-DFT Study on the Charge-Transfer Excitations of Anions Possessing Double or Triple Bonds. *Computational and Theoretical Chemistry* **2013,** *1014*, 49-55.

13. Brøndsted Nielsen, S.; Brøndsted Nielsen, M.; Rubio, A., Spectroscopy of Nitrophenolates in Vacuo: Effect of Spacer, Configuration, and Microsolvation on the Charge-Transfer Excitation Energy. *Accounts of Chemical Research* **2014,** *47* (4), 1417-1425.

14. Houmøller, J.; Wanko, M.; Rubio, A.; Brøndsted Nielsen, S., Effect of a Single Water Molecule on the Electronic Absorption by o- and p-Nitrophenolate: A Shift to the Red or to the Blue? *The Journal of Physical Chemistry A* **2015,** *119* (47), 11498-11503.

15. Panja, S. K.; Dwivedi, N.; Saha, S., Tuning the Intramolecular Charge Transfer (ICT) Process in Push-Pull Systems: Effect of Nitro Groups. *RSC Advances* **2016,** *6* (107), 105786-105794.

16. Stockett, M. H.; Boesen, M.; Houmøller, J.; Brøndsted Nielsen, S., Accessing the Intrinsic Nature of Electronic Transitions from Gas-Phase Spectroscopy of Molecular Ion/Zwitterion Complexes. *Angewandte Chemie* **2017,** *129* (13), 3544-3549.

17. Michenfelder, N. C.; Ernst, H. A.; Schweigert, C.; Olzmann, M.; Unterreiner, A. N., Ultrafast Stimulated Emission of Nitrophenolates in Organic and Aqueous Solutions. *Physical Chemistry Chemical Physics* **2018,** *20* (16), 10713-10720.

18. Western, C. M., PGOPHER: A Program for Simulating Rotational, Vibrational and Electronic Spectra. *Journal of Quantitative Spectroscopy and Radiative Transfer* **2017,** *186*, 221-242.

19. Xu, S.; Gozem, S.; Krylov, A. I.; Christopher, C. R.; Weber, J. M., Ligand Influence on the Electronic Spectra of Monocationic Copper–Bipyridine Complexes. *Physical Chemistry Chemical Physics* **2015,** *17* (47), 31938-31946.

20. Asvany, O.; Schlemmer, S., Numerical Simulations of Kinetic Ion Temperature in a Cryogenic Linear Multipole Trap. *International Journal of Mass Spectrometry* **2009,** *279* (2), 147-155.

21. Wester, R., Radiofrequency Multipole Traps: Tools for Spectroscopy and Dynamics of Cold Molecular Ions. *Journal of Physics B: Atomic, Molecular and Optical Physics* **2009,** *42* (15), 154001.

Chapter 4 The Green Fluorescent Protein Chromophore

This chapter has been adapted with permission from:

(a) W. Zagorec-Marks, M. M. Foreman, J. R. R. Verlet, J. M. Weber, "Cryogenic Ion Spectroscopy of the Green Fluorescent Protein Chromophore in Vacuo", J. Phys. Chem. Lett. 10 (2019) 7817 - 7822.

(b) W. Zagorec-Marks, M. M. Foreman, J. R. R. Verlet, J. M. Weber, "Probing the Microsolvation Environment of the Green Fluorescent Protein Chomophore in Vacuo", J. Phys. Chem. Lett. 11 (2020) 1940-1946.

(c) W. Zagorec-Marks, M. M. Foreman, J. M. Weber "Tag-Free, Temperature Dependent Infrared Spectra of the GFP Chromophore – Revisiting the Question of Isomerism", J. Phys. Chem. A 124 (2020) 7827–7831.

4.1 Introduction

The Green Fluorescent Protein (GFP) and its variants are widely used for fluorescence labeling in biology.[1-5] The chromophore (and fluorophore) is a small molecular unit, which consists of a phenol ring linked to an imidazole ring by a methine bridge in the *para*-position, residing inside the beta barrel of the protein. The chromophore is accompanied by a single water molecule, which binds to the anionic phenolate group of the chromophore.[6] A commonly used model of the GFP chromophore is deprotonated *p*-hydroxybenzylidene-2,3-dimethylimidazolinone ($HBDI^-$, see Figure 4.1). In this model, the linkers to the protein have been replaced with methyl groups on the imidazole ring. The deprotonated form is used because only the anion fluoresces in the protein, while the neutral form undergoes excited state proton transfer upon photon absorption, and relaxes without photon emission.[3] As can be seen in Figure 4.1, there are two isomeric forms referred to as *Z*- and *E*-HBDI$^-$ which are related by a twisting around the double bond of the methine bridge. This twisting motion is reminiscent of the torsional motion of *p*-nitrophenolate (*p*-NP), discussed in Chapter 3. As was the case in *p*-NP, excitation with visible irradiation initiates a twisting motion during relaxation on the S_1 excited state. This occurs both in low viscosity solvents[7-8] and *in vacuo*[9] and results in loss of fluorescence due to low Franck-Condon factors. In GFP, this motion is blocked, giving rise to the fluorescence.

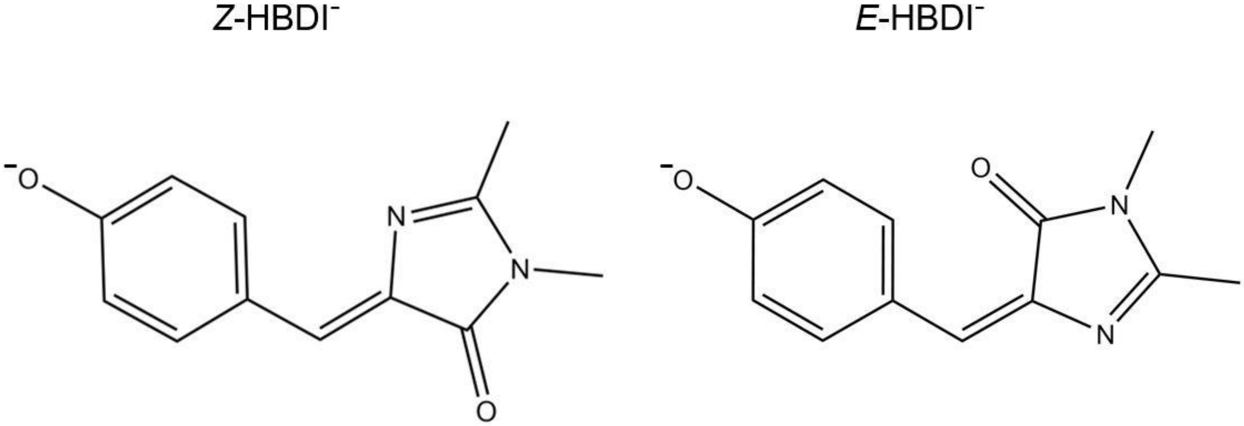

Figure 4.1. Deprotonated *p*-hydroxybenzylidene-2,3-dimethylimidazolinone (HBDI$^-$) as the *Z*- and *E*- isomer. The two isomers are related by rotation about the carbon double bond of the methine bridge.

The $S_0 \rightarrow S_1$ band envelope informs on the initial photophysics of the S_1 transition of HBDI$^-$ and its interactions with the chemical environment (the chromophore pocket of the protein, solvent, etc.). Consequently, there have been many experiments on HBDI$^-$ *in vacuo* aimed at understanding its intrinsic photophysics. Interestingly, the spectrum of isolated HBDI$^-$ is very similar to that of the chromophore in the protein, and in stark contrast to the absorption spectrum in aqueous solution. This suggests that the protein environment results in initial photophysics more like those in vacuum than aqueous solution. All previous photodissociation experiments on $HBDI^-$ have been done at room temperature. The broadening resulting from hot bands obscures details of the $S_0 \rightarrow S_1$ band envelope. In addition, the effect of a microsolvation environment mirroring the water molecule present in the chromophore pocket of the protein has only been explored computationally so far.[10]

The relaxation pathway from the S_1 excited state in vacuo results in dissociation or loss of an electron, since the energy deposited in the molecule cannot be dissipated into the chemical environment. As a consequence, the intrinsic photophysics of $HBDI^-$ has been primarily investigated using photodissociation and photoelectron spectroscopies.[7-9, 11-32] Photodissociation of bare $HBDI^-$ occurs primarily through the loss of a CH_3 group. In a one-photon absorption event with sufficient energy, this dissociation typically takes milliseconds.[33] This time scale is not accessible in our experiment, and thus we rely on absorption of two photons when studying bare $HBDI^-$, which causes dissociation on a microsecond timescale.[32] The threshold for electron detachment is only slightly higher than the energy of the absorption band maximum, but still within the FC envelope (22017 for electron detachment vs 20833 cm^{-1} band origin).[34] This means that electron detachment and unimolecular dissociation are competing relaxation pathways upon photoexcitation with two photons. Moreover, electron detachment can occur either directly, or through vibrational autodetachment, the latter of which is thought to dominate.[9, 16, 18-21, 25-28, 35] A recent study by Bieske and coworkers[13] revealed a further complication, when they showed that under typical preparation conditions at room temperature, a significant fraction of the produced $HBDI^-$ ions may exist as the *E* isomer, while previous interpretations have been largely focused the *Z* isomer. In this chapter, we discuss the spectra of bare, messenger-tagged, and microsolvated $HBDI^-$ in the visible and infrared spectral regions. The spectra are interpreted using DFT calculations. In the final section of the chapter, we introduce an IR-UV double resonance technique, which we will refer to as hot band assisted infrared (HAIR) spectroscopy, which can be used to circumvent the use of a messenger tag, and allows the acquisition of temperature dependent IR spectra, which is not possible with messenger tagging.

4.2 Computational

Ground state geometry optimizations and harmonic frequency calculations were performed at the DFT level of theory using the B3LYP functional and def2-TZVPP basis sets. As previously noted by Oomens and coworkers, there is a strong basis set dependence of the IR features for HBDI.[36] Exploratory calculations show that this problem only occurs for basis sets smaller than the one used here. Excited state geometry optimizations and harmonic frequency calculations were performed using the range-corrected CAM-B3LYP functional and def2-TZVPP basis set. Excited state frequency calculations were necessary to carry out Franck-Condon (FC) simulations. In these simulations, the temperature is 55 K and the full width at half-maximum (FWHM) of the vibrational features is 80 cm^{-1} fit the observed vibrational structure. Vertical excitation calculations using both CAM-B3LYP and ω-B97XD functionals yield similar results that overestimate the electronic band origin by about 0.5 eV for the *Z* isomer and were thus shifted by ca. -4000 cm^{-1} to match the experimental spectrum of $[HBDI^{-}\cdot N_2]$. All calculations were carried out in Gaussian 16.

4.3 The isolated chromophore

The electronic spectrum of the complex $[HBDI\cdot N_2]^{-}$ is shown in Figure 4.2. The loss channel for this spectrum was the loss of neutral N_2, which has a calculated binding energy of 630 cm^{-1} and 720 cm^{-1} when bound to the imidazole and phenolate groups, respectively. Due to the low binding energy of the messenger tag, dissociation of this complex is likely to occur with near unit probability upon absorption of a photon, even down to the far infrared (*ca.* 1000 cm^{-1}). The low binding energy also guarantees that the complexes are cold, and the temperature can be estimated to be < 75 K by describing cluster formation in the ion trap as an evaporative ensemble.[37] Afforded by the low temperature, the spectrum of $[HBDI\cdot N_2]^-$ shows a sharp onset at 20530 ± 25 cm^{-1} followed by peaks at 20780 ± 10 cm^{-1} and 20835 ± 10 cm^{-1}. Additionally, we partially resolve vibrational substructure with a spacing of *ca*. 70 cm^{-1}. Another feature appears with an onset at 21830 cm^{-1} and a peak at 22130 cm^{-1}.

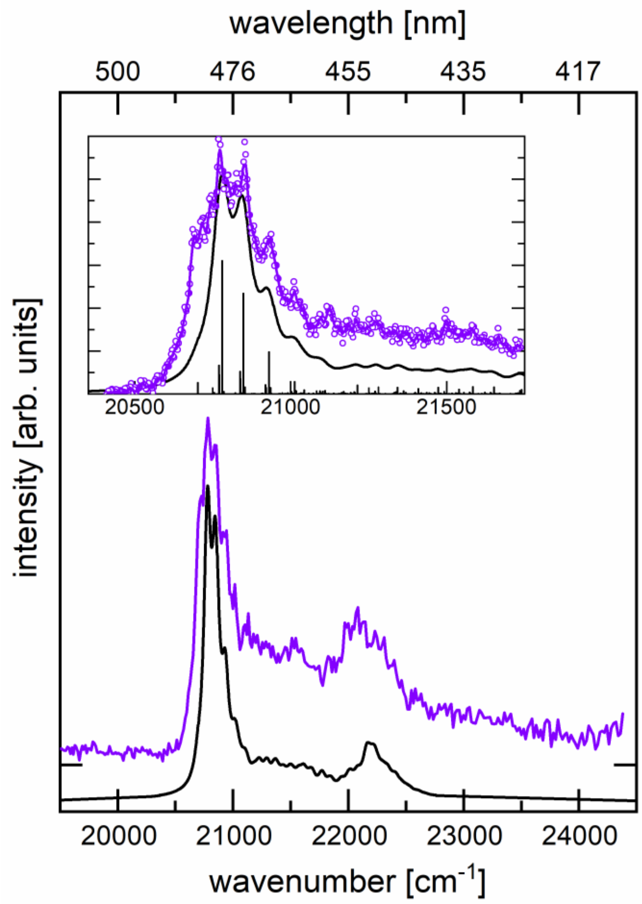

Figure 4.2. Electronic spectrum of $[HBDI{\cdot}N_2]^-$. The open circles are raw data points, the purple full line is a 5-point adjacent average to guide the eye. The black full lines are Franck-Condon-Herzberg-Teller (FCHT) simulations of the vibrational substructure in the $S_1 \leftarrow S_0$ electronic band, with the vibrational states indicated as vertical sticks. The insert shows the band origin region, and the data in this trace were taken with a step size of 2.6 cm^{-1}, while the step size in the overview spectrum was 13 cm^{-1} in the origin region. The FCHT simulation has been shifted by ca. -4000 cm^{-1} for the best match to the experimental spectrum (see section 4.2).

As mentioned above, there is the possibility of two isomers arising from the electrospray source. The infrared photodissociation spectrum of $[HBDI{\cdot}N_2]^-$ is presented in Figure 4.3 along with calculated harmonic spectra of the *Z* and *E* isomers. The two isomers have similar calculated spectra, but a distinction can be made using the spacing between the three most intense features in the 1400 – 1700 cm^{-1} region. The spacing between the upper two features is 80 cm^{-1} and 60 cm^{-1}

for the *Z* and *E* isomers respectively, compared to 80 cm^{-1} in the experimental. For the lower two features, the spacing is 50 cm^{-1} and 80 cm^{-1} for the *Z* and *E* isomers respectively, compared to 55 cm^{-1} in the experimental. We therefore conclude that the *Z* isomer is present, and the narrow width of the main features indicates that only one isomer is significantly populated. This assignment is consistent with the fact that calculations place the *Z* isomer lower in energy by 800 cm^{-1}, and with ion mobility experiments that showed the presence of the *Z* isomer exclusively when $HBDI^-$ is complexed with solvent molecules.[13] All vibrational features are assigned and described in Table 4.1.

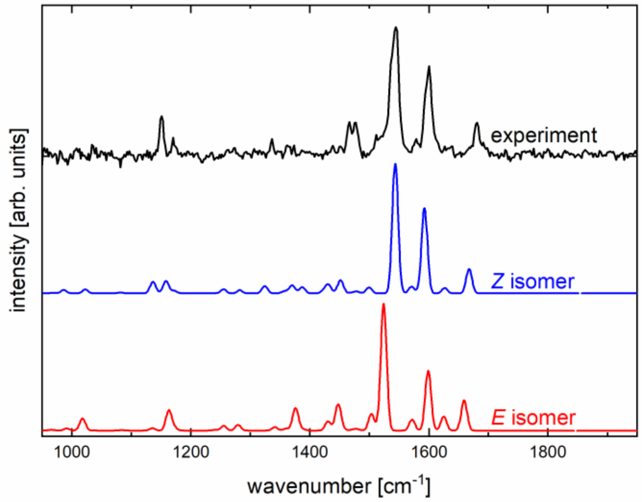

Figure 4.3. Infrared spectrum of $[HBDI{\cdot}N_2]^-$ (top trace) compared to simulated spectra of the *Z* isomer (center trace) and *E* isomer (bottom trace) of $HBDI^-$. The calculations have been scaled by 0.98. A detailed assignment of the vibrational features is listed in Table 4.1.

Table 4.1. Vibrational mode assignments for $[HBDI\cdot N_2]^-$ based on the calculated spectrum of the *Z* isomer.

mode	**observed [cm^{-1}]**	**calculated ^{a} [cm^{-1}]**
in-plane CH bending / imidazole ring deformation	1151	1137
phenolate CH in-plane bending	1170	1159
methyl umbrella / imidazole deformation	1466	1430
methyl umbrella / phenolate deformation	1477	1451
phenolate in-plane CH bending / phenolate deformation	1512	1500
in-plane CH bending / imidazole ring deformation	1544	1544
phenolate CO stretching / ring deformations	1578	1571
in-plane CH bending / imidazole ring deformation	1600	1593
phenolate CO stretching / bridge deformation	1632	1627
imidazole CO stretching	1680	1667

^{a} B3LYP/def2-TZVPP scaled by 0.98.

Figure 4.2 includes an FCHT simulation of the $S_1 \leftarrow S_0$ absorption band for the *Z* isomer, which after shifting the band origin by ca 4000 cm^{-1} qualitatively matches the experimental spectrum. Using this simulation, we assign the low-frequency mode, corresponding to the 70 cm^{-1} spacing prominently appearing in the experimental electronic spectrum, as a methine bridge bending/ ring scissoring mode (ω_B, calculated at ca. 80 cm^{-1} on the S_1 surface but set to 65 cm^{-1} to make the agreement better). We assign the peak at 20780 ± 10 cm^{-1} as the electronic band origin, based on the hot band structure on its low-energy side. The broad feature which peaks at 22130 ± 40 cm^{-1} is due to combination bands of ω_B building on an imidazole ring breathing/in-plane CH bending mode on the S_1 surface (ω_I, calculated at ca. 1350 cm^{-1}), consistent with previous assignments.[24, 38-39] The observed spectral congestion is largely due to the ω_B mode which is responsible for the two hot bands below the band origin and the high-energy shoulder of the ω_I feature. The width of the experimental features is not limited by the experimental resolution (see Chapter 2). We estimate the measured linewidth has a full width at half maximum of *ca.* 80 cm^{-1}, based on a comparison with the calculated spectrum, and note that in the previous chapter we were able to resolve narrow lines of the vibronic progression of *meta*-NP. The width is instead attributed to congestion of the spectrum along with intrinsic dynamics of the system, where the initial excited state dynamics are expected to occur on a sub-100 fs timescale.

The unshifted value of the calculated band origin is 26200 cm^{-1} which is substantially higher than the experimental value. Our FC profile is substantially different from calculations done at much higher levels of theory,[24, 38-39] which yielded more accurate values for the band origin but vibronic progressions that deviate from the experimental progression (see Figure 4.4 for a direct comparison). We note that the experimental data presented in Figure 4.2 provide the best benchmark to date to gauge the quality of computational approaches to this molecular system.

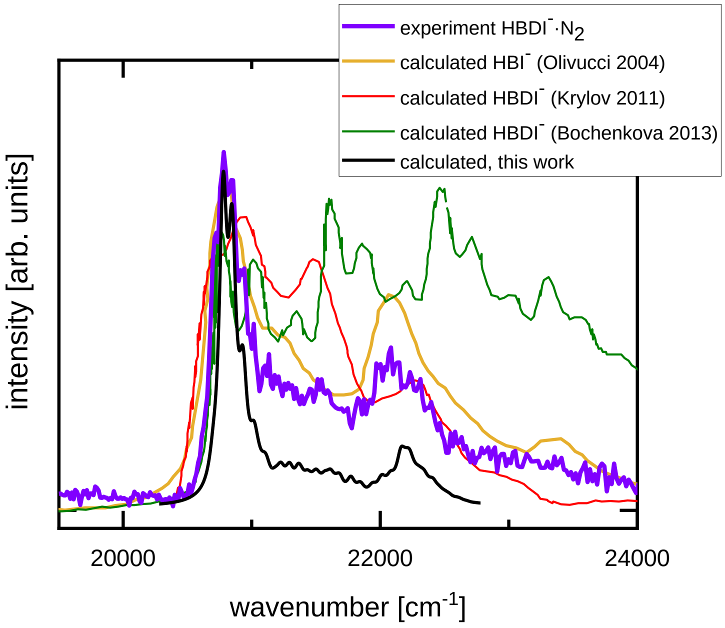

Figure 4.4. Comparison of the experimental spectrum of $[HBDI \cdot N_2]^-$ with calculated spectra from the literature. The calculated curves have all been shifted to optimally match the experimental data. The literature data have been adapted from the references.[24, 38-39]

Prior electronic spectroscopy experiments using N_2 as a messenger tag suggest that a small shift of spectral features is expected relative to the bare species, so it is of interest to contrast the spectrum of $[HBDI \cdot N_2]^-$ presented in Figure 4.2 with that of bare $HBDI^-$.[40] Figure 4.5 shows this comparison at various ion trap temperatures.

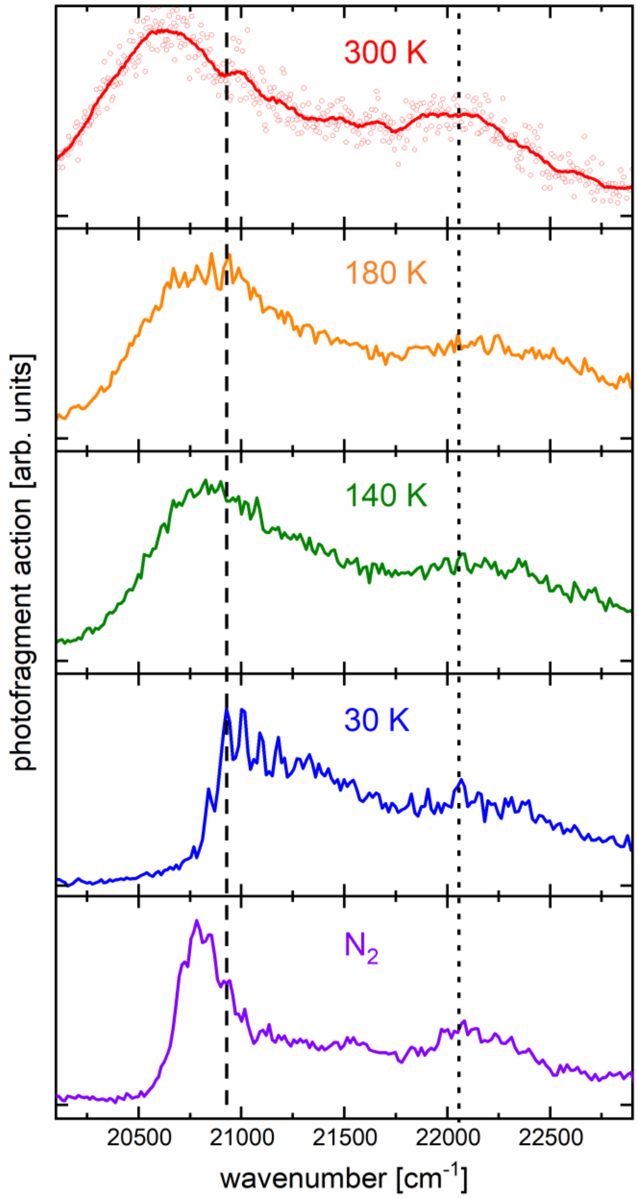

Figure 4.5. Electronic spectra of HBDI$^-$ at various trap temperatures. The open circles are raw data points, the full lines are adjacent averages to guide the eye, with 3, 5 and 20 points for [HBDI·N$_2$]$^-$, 30 K and the other experimental conditions, respectively. The vertical dashed and dotted lines show the peak positions for bare HBDI$^-$ (30 K) of the (v=0) ← (v=0) band at (20800 ± 10) cm^{-1}, and of the high energy feature around 22100 cm^{-1}, respectively.

The electronic spectrum of bare HBDI$^-$ has an onset at 20250 ± 50 cm^{-1}, which is at much lower wavenumbers than that of [HBDI·N$_2$]$^-$, and the peak of the spectrum is at 20930 ± 10 cm^{-1}, with partially resolved shoulders on the lower energy side. The high-energy side of this peak has the same spacing of vibrational features in both the bare and $[HBDI\cdot N_2]^-$ spectrum. We assign the peak at 20930 cm^{-1} as the band origin of $HBDI^-$. The presence of the first N_2 messenger tag results in a shift of the spectrum by 150 ± 27 cm^{-1} to the red. Addition of a second N_2 tag, shown in Figure 4.6, leads to an additional red shift of 80 ± 27 cm^{-1} (measured from the highest point of the band envelope). The spectrum of $[HBDI\cdot 2(N_2)]^-$ has a similar band envelope, but is in general less well resolved than the spectrum of $[HBDI\cdot N_2]^-$. Because there are now two N_2 molecules which can each bind to $HBDI^-$ at either oxygen site, there are possibly many distinct position isomers present, each with a potentially different band origin. The spectral congestion caused by the presence of these isomers, in combination with low overall signal-to-noise ratio, is likely the reason we do not resolve the 70 cm^{-1} spaced features on the main absorption peak.

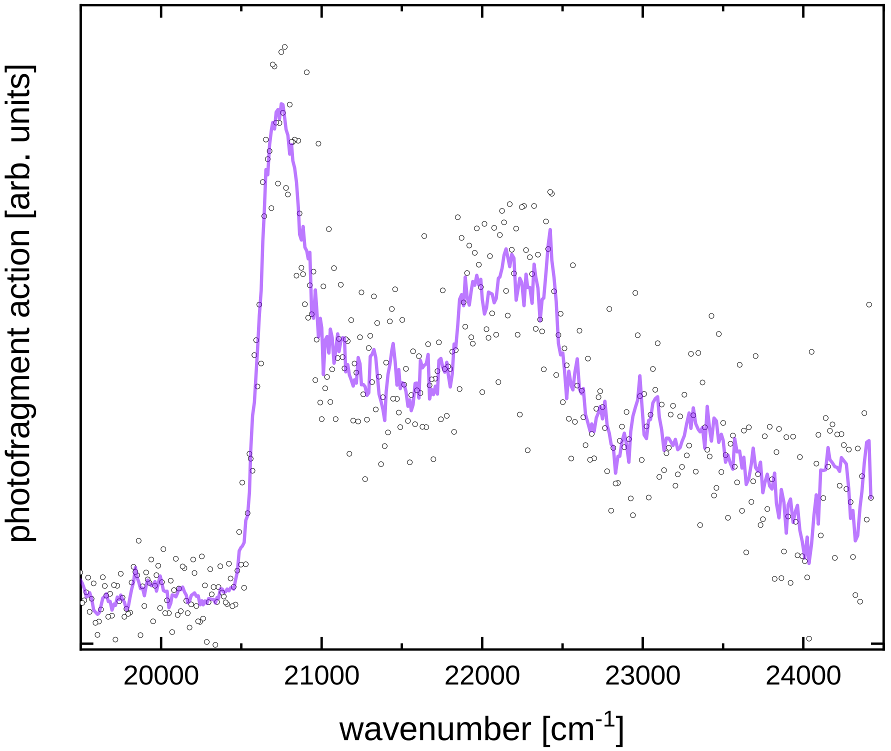

Figure 4.6. Electronic spectrum of $[HBDI\cdot(N_2)_2]^-$. Open circles represent the raw data, the purple line is a 5-point gliding average to guide the eye.

With increasing temperature, a prominent shoulder below the band origin develops, until we observe a partially resolved peak at 20700 ± 25 cm^{-1} at 180 K, which eventually dominates the spectrum at 300 K. This feature could be due to hot bands. However, our FC simulations do not recover this behavior regardless of the simulation temperature, consistent with FC simulations performed by others.[24, 38-39] Alternatively, this feature could be evidence for the presence of the *E* isomer, which would be consistent with recent results by Bieske and coworkers. They observed the presence of the *E* isomer in ion mobility experiments on $HBDI^-$ ions prepared at room temperature, and found that the *E* isomer absorbs at slightly longer wavelengths than the *Z* isomer.[13] The barrier to isomerization has been calculated to be 1.24 eV, which would prevent thermal isomerization.[13] We will revisit this problem in Section 4.5, where we will argue that only the Z isomer is present in our experiment.

There are subtle differences between the band envelopes of bare and N_2-tagged $HBDI^-$. The relative intensities of the feature around 22000 cm^{-1} and the band origin are different for the two species. This could be due to a change in the FC factors, but this seems unlikely given the small perturbation the N_2 tag induces. Alternatively, it could be due to a change in the branching ratio between internal conversion and electron detachment, as the adiabatic electron affinity of HBDI is 22017 cm^{-1}.[34] To test this hypothesis, we present a comparison of the parent ion depletion (which would include both fragmentation and electron loss) and fragment ion formation signal channels in Figure 4.7. As can be seen in the figure, the two traces show a near perfect overlap indicating that electron detachment does not play a role in our experiment. A third possibility is simply that there is a difference in ion temperatures, despite similar trap temperatures between $[HBDI{\cdot}N_2]^-$ and bare $HBDI^-$. As discussed in Section 4.3, the presence of the N_2 messenger tag limits the internal energy of the complex to *ca*. 720 cm^{-1}, while the bare ion has no such limit, and could be affected by radiofrequency heating (see Chapter 3).

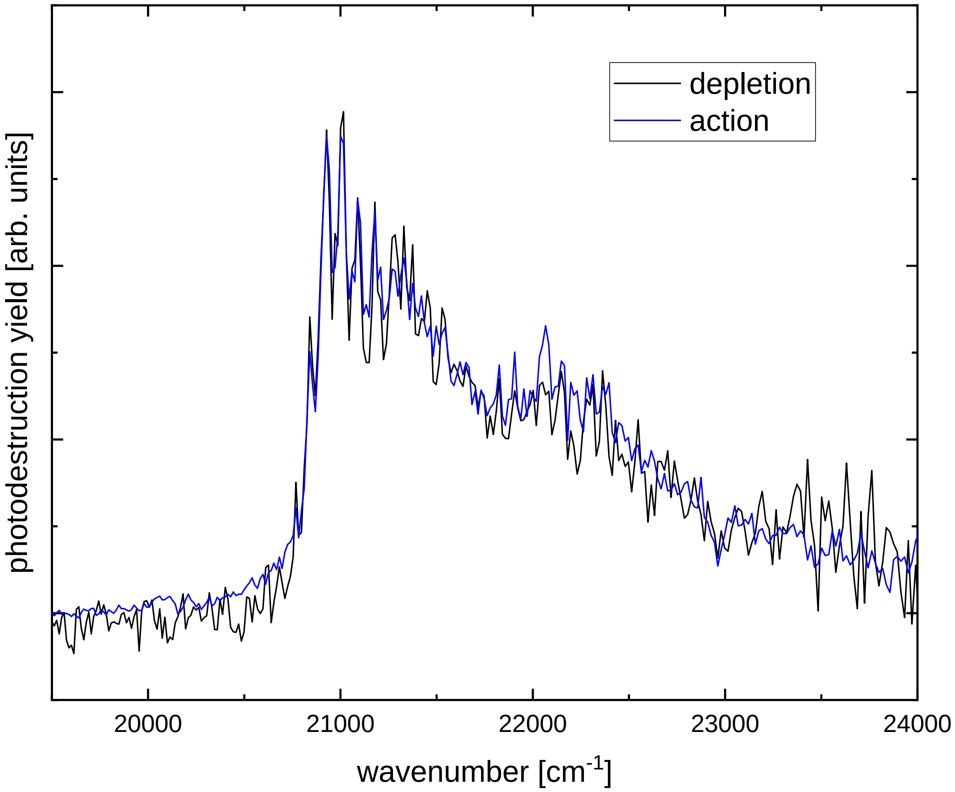

Figure 4.7. Comparison of the experimental photofragment action spectrum of HBDI$^-$ at 30 K trap temperature (blue curve) with the parent ion depletion spectrum taken at the same temperature (black curve).

4.4 Effects of microsolvation

In the chromophore pocket of GFP, a single water molecule binds to the phenolate moiety of the chromophore.[41] This interaction has only been investigated computationally for HBDI$^-$,[10] and one of the questions in this context is whether the water molecule has a strong influence on the electronic spectrum of the chromophore. By raising the trap temperature to 180 K, we are able to form complexes between HBDI$^-$ and water molecules ($[\text{HBDI}\cdot(\text{H}_2\text{O})_n]^-$, where $n = 1, 2$). Figure 4.8 shows the experimental IR spectrum of the water complexes compared with $[\text{HBDI}\cdot\text{N}_2]^-$.

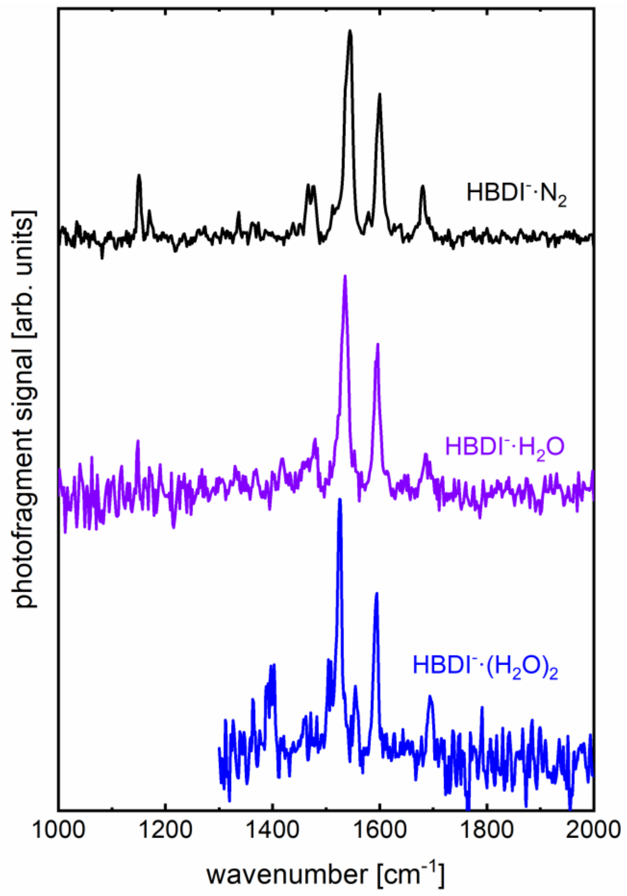

Figure 4.8. Infrared spectra of [HBDI·N$_2$]$^-$ and [HBDI·(H$_2$O)$_n$]$^-$ (n = 1, 2) from 1000 to 2000 cm^{-1}. The photofragment signals were due to the loss of N$_2$ for [HBDI·N$_2$]$^-$ and of a single H$_2$O molecule for [HBDI·(H$_2$O)$_n$]$^-$, respectively.

Based on the similarities between the three traces in Figure 4.8, we conclude that the chromophore in hydrated clusters is in the *Z* isomer. We also note the positions of the intense vibrational features of HBDI$^-$ are only weakly influenced by the microsolvation environment. The mode assignments for all three complexes in Figure 4.8 are presented in Table 4.2. The small changes to vibrational frequencies are in line with computational predictions by Krylov and coworkers.[10] There are several ways in which each water molecule can bind to the two oxygen molecules, and the binding motifs considered here are displayed in Figure 4.9.

Table 4.2. Vibrational mode assignments for [$HBDI^{-}\cdot N_2$] and [$HBDI^{-}\cdot(H_2O)_n$] (n = 1, 2).

mode	$HBDI^{-}\cdot N_2$	n = 1	n = 2
in-plane CH bending / imidazole ring deformation	1151	1148	N/A
phenolate in-plane CH bending / CO stretching	N/A	N/A	1396
methyl umbrella / imidazole deformation	1466	1461	N/A
methyl umbrella / phenolate deformation	1477	1478	N/A
phenolate in-plane CH bending / phenolate deformation	1512	N/A	1506
in-plane CH bending / imidazole ring deformation	1544	1535	1526
phenolate CO stretching / ring deformations	1578	N/A	1554
in-plane CH bending / imidazole ring deformation	1600	1595	1593
imidazole CO stretching	1680	1687	1695

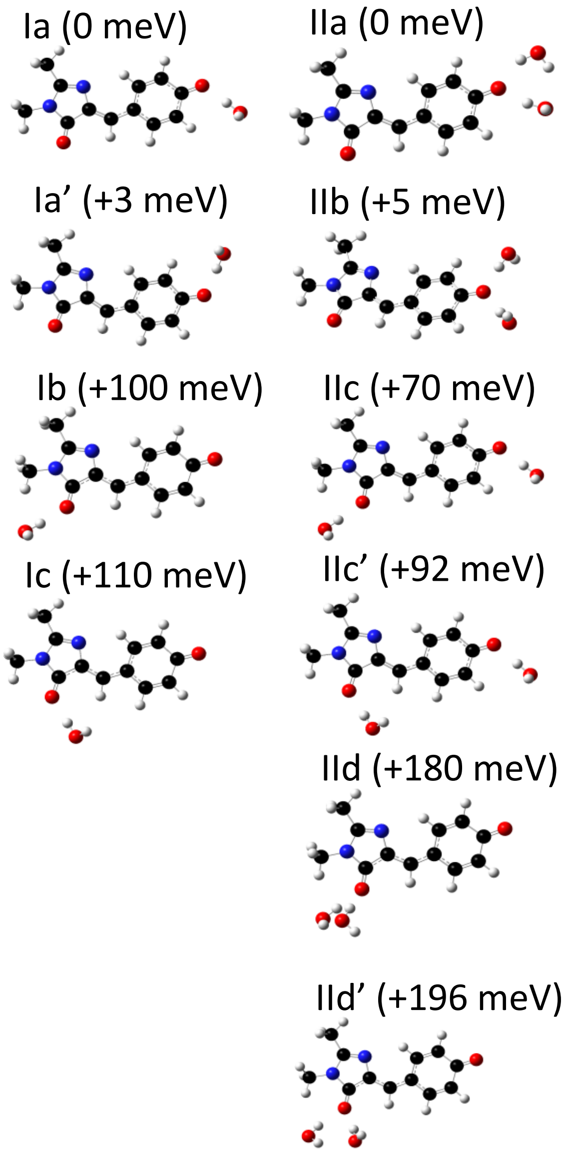

Figure 4.9. Calculated structures for all solvated species. Monohydrated species (left) are shown with energy relative to (Ia), dihydrate species (right) are presented with energy relative to (IIa). All energies are calculated at 0 K.

Natural bonding orbital calculations, done at the B3LYP/def2-TZVPP level of theory, indicate that in bare HBDI$^-$ both oxygen atoms have roughly equal charge (see Table 4.3). When a single water molecule is added, the negative change on the oxygen it binds to is increased slightly (*ca*. 0.04 e), which is followed by an increase in the corresponding CO bond length by about 1%. As noted in Table 4.2, the peak at 1680 cm^{-1} corresponds to the CO stretching vibration of the imidazole group. This peak shifts by +7 cm^{-1} in the monohydrate spectrum, and another +8 cm^{-1} in the dihydrate spectrum. These shifts are consistent with a loss of electron density from the imidazole oxygen and a strengthening of the CO bond of the imidazole group. This suggests that the water molecules are attached to the phenolate oxygen, but the evaluation of other features in the fingerprint region and in the OH stretching region shows that this is too simple an interpretation (see below).

Table 4.3. Calculated selected charges (in e) and bond lengths (in Angstroms) in HBDI$^-$ and different position isomers for $[HBDI\cdot(H_2O)_n]^-$ ($n = 1, 2$); isomer labels refer to Figure 4.9.

Absolute values	charge on phenolate O	charge on imidazole O	phenolate CO bond length	imidazole CO bond length
Bare	-0.662	-0.668	1.24882	1.23223
n = 1 on phenolate (Ia)	-0.699	-0.657	1.26178	1.22972
n = 1 on imidazole (Ib)	-0.653	-0.713	1.24701	1.24317
n = 2, both on phenolate (IIa)	-0.748	-0.648	1.26932	1.22787
n = 2, both on imidazole (IIc)	-0.643	-0.762	1.24525	1.25365
n = 2, one each on phenolate and imidazole (IIb)	-0.691	-0.703	1.25972	1.24032
Differences for hydration isomers w.r. to bare HBDI$^-$				
n = 1 on phenolate (Ia)	-0.037	0.011	0.01296	-0.00251
n = 1 on imidazole (Ib)	0.009	-0.045	-0.00181	0.01094
n = 2, both on phenolate (IIa)	-0.086	0.02	0.0205	-0.00436
n = 2, both on imidazole (IIc)	0.019	-0.094	-0.00357	0.02142
n = 2, one each on phenolate and imidazole (IIb)	-0.029	-0.035	0.0109	0.00809

The next two significant features of the HBDI$^-$ IR spectrum are the peaks at 1600 cm^{-1} and 1544 cm^{-1}, and both can be described as in-plane CH bending/imidazole ring deformation modes. The upper feature shifts by -6 cm^{-1} upon addition of the first water molecule, and shifts -2 cm^{-1} further with addition of the second water molecule. The peak at 1544 cm^{-1} shifts steadily by *ca.* 10 cm^{-1} per water molecule. The CO stretching motion of the phenolate ring is present as a shoulder on the high energy side of the dominant feature at 1578 cm^{-1}. This feature becomes clearly identifiable in the dihydrate spectrum when it has shifted to 1554 cm^{-1} and is now a resolved peak. The red-shift of this mode is consistent with hydration at the phenolate. However, an additional weak feature around 1650 cm^{-1} is characteristic of an isomer with a water molecule bound to the imidazole oxygen. Finally, a feature at 1396 cm^{-1}, which corresponds to an in-plane HCH bending/CO stretching mode on the phenolate moiety, gains intensity in the dihydrate spectrum. This behavior is only reproduced in calculations with both water molecules bound to the phenolate moiety.

In general, the spectral region from 1000 cm^{-1} to 2000 cm^{-1} shows weak effects of microhydration on the vibrational spectrum of the chromophore and suggests that we have a mixture of conformers, with some hydrated at the phenolate and some at the imidazole for both the mono- and dihydrated species. To investigate this question from the point of view of the solvent, we move to the OH stretching region of the IR, where the OH stretching frequencies of the water molecules will serve as sensitive IR probes of their hydrogen bonding environment.

Figure 4.10 shows the IR spectra of $[\mathrm{HBDI}\cdot\mathrm{N_2}]^-$ and $[\mathrm{HBDI}\cdot(\mathrm{H_2O})_n]^-$ (n = 1, 2) over the range of 2700 cm^{-1} to 3800 cm^{-1}. The spectrum of $[\mathrm{HBDI}\cdot\mathrm{N_2}]^-$ contains only CH stretching modes in this region (as no OH groups are present) in the range of 2800 cm^{-1} to 3100 cm^{-1}. This region can contain Fermi interactions between HCH bending mode overtones and CH stretching fundamentals, making assignments of vibrational features difficult. Despite this problem, we assign the peaks at 2848 cm^{-1} and 2878 cm^{-1} to the totally symmetric stretching modes of the CH_3 groups on the imidazole moiety and the unresolved group of peaks around 2930 cm^{-1} to the antisymmetric version of these modes. The two peaks at 3033 cm^{-1} and 3059 cm^{-1} are tentatively assigned as CH stretching modes of the phenolate ring. All of the CH stretching features exhibit minimal shifts upon hydration.

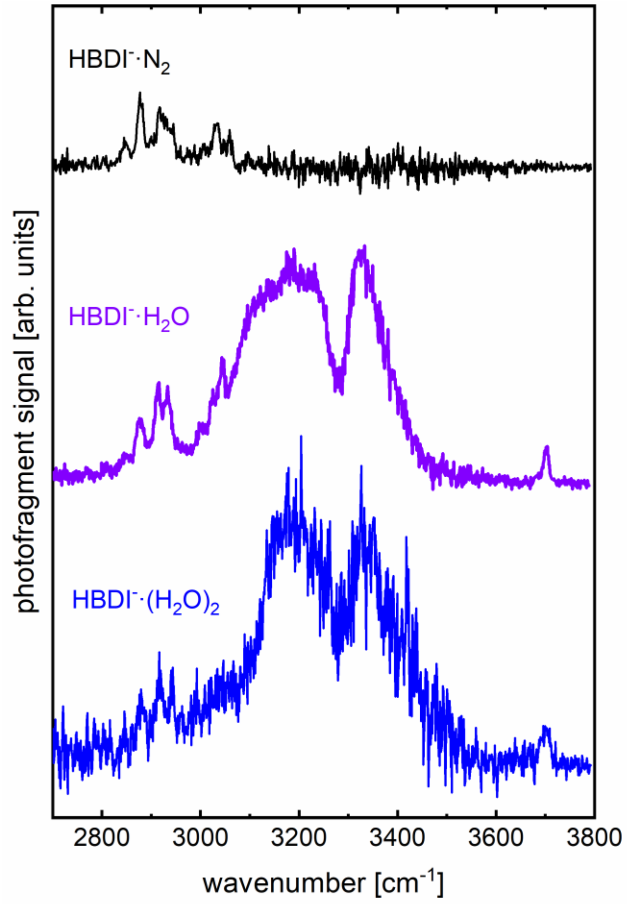

Figure 4.10. IR spectra of of [$HBDI^-\cdot N_2$] (top, black) and [$HBDI^-\cdot(H_2O)_n$] (n = 1, 2 magenta and blue) from 2700 to 3800 cm^{-1}. The photofragment loss channels are the same as in the low energy region.

The remainder of this spectral region contains the OH stretching vibrations of the water molecules, which dominate the spectra of the hydrated ion. All structures calculated here have at least one free OH oscillator that does not participate in a hydrogen bonding interaction. The signature for the free OH appears at 3703 cm^{-1} and is present in both the singly and doubly hydrated species. The large features in the 3100 cm^{-1} to 3500 cm^{-1} range belong to hydrogen bonded OH stretching vibrations.

Figure 4.11 shows a comparison of the experimental and calculated IR spectra for several conformers of the monohydrated species. We assign the broad feature at 3180 cm^{-1} to the signature of a water molecule solvating the phenolate oxygen. The corresponding vibrational mode can be characterized as the symmetric OH stretching mode, and is primarily localized on the OH group participating in the hydrogen bond. A conformer (Ia', see Figure 4.9) with the water molecule binding to the phenolate, but *anti* to the methine bridge CH group is isoenergetic with conformer Ia and has an identical infrared spectrum. The feature at 3340 cm^{-1} is representative of the symmetric OH stretching mode of a water molecule solvating the imidazole oxygen. The presence of both features confirms that we indeed have a mixture of conformers present in the experiment.

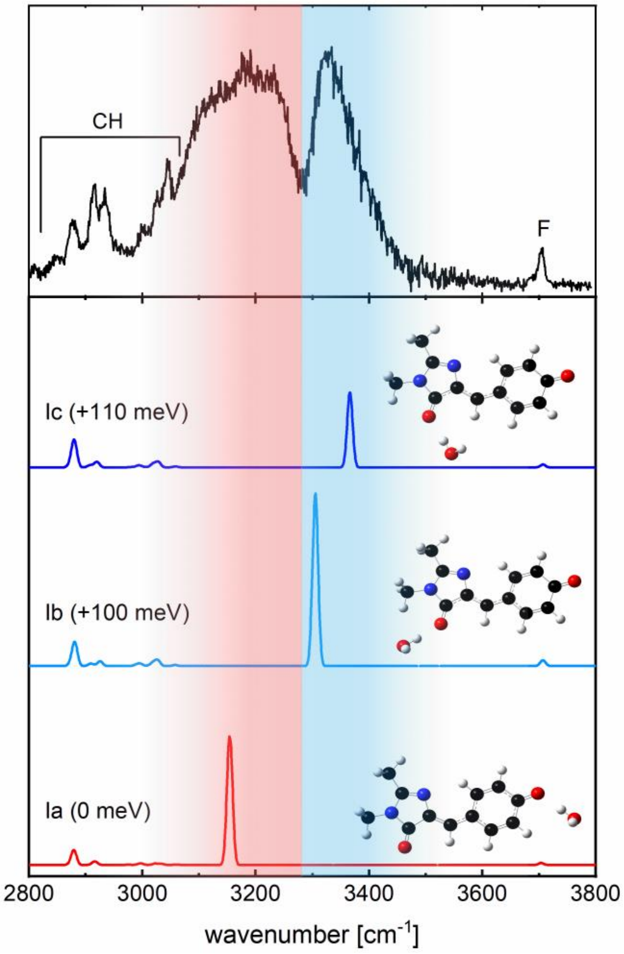

Figure 4.11. Calculated infrared spectra of selected conformers of monohydrated HBDI$^-$ (lower traces, see Figure 4.9 for other conformers), compared to the experimental spectrum (upper trace). The spectrum contains signatures for CH stretching vibrations (CH), H-bonded OH stretching on the phenolate (red-shaded region) and imidazole (blue-shaded region) groups, and the free OH stretching mode (F). All calculations have been scaled by 0.957 to match the experimentally observed free OH stretching vibrations. The calculated energies (at 0 K) of the conformers relative to the lowest energy conformer (Ia) are given in each simulated trace.

The broad widths of the hydrogen bonded OH stretching features reflect the fact that the complexes are formed through an evaporative ensemble,[37] with internal energies on the order of the binding energy of a water molecule (about 4000 cm^{-1}, discussion to follow). Because of this, the water molecule is likely to explore a significant range of OH···O$^-$ angles through large amplitude motions both in the plane of the HBDI$^-$ and perpendicular to it, resulting in the observed broadening. Figures 4.13 and 4.14 show the calculated frequency of the hydrogen bonded OH stretching mode as a function of the in-plane and out-of-plane pivot angle respectively. As can be seen in the figures, motion in either of these coordinate can lead to a change in OH stretching frequency of *ca*. 200 cm^{-1}.

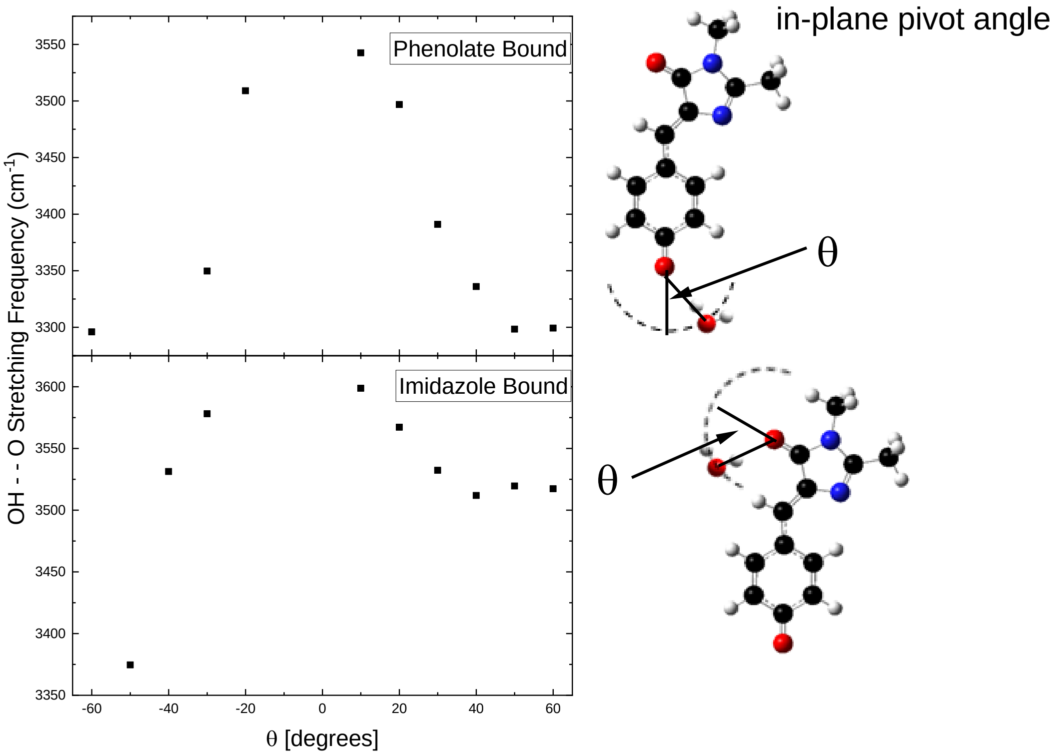

Figure 4.12. Calculated hydrogen bonded OH stretching frequency as a function of the in-plane pivot angle for both a phenolate bound and imidazole bound water molecule.

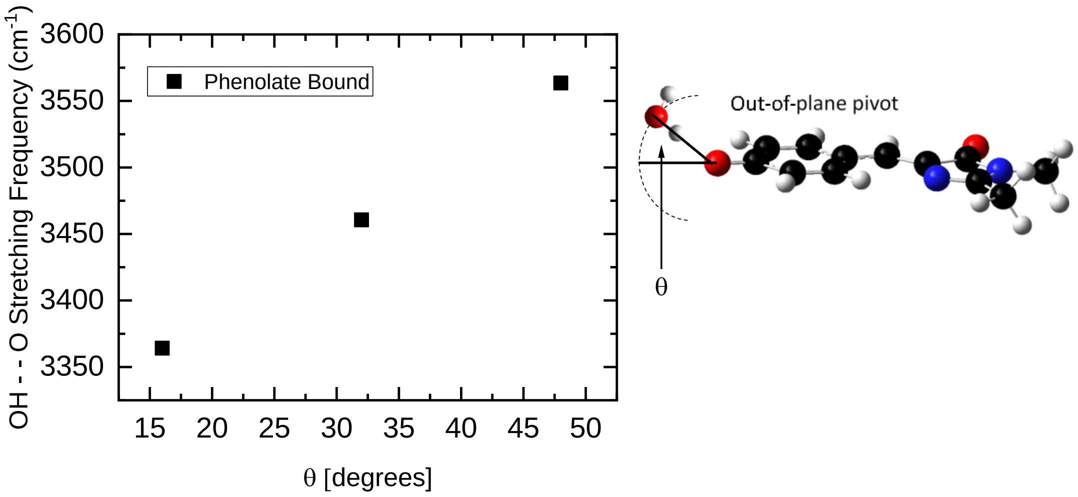

Figure 4.13. Calculated hydrogen bonded OH stretching frequency as a function of the out-of-plane pivot angle for both a phenolate bound water molecule.

Overall, we obtain similar structures and energetic ordering as found by Krylov and coworkers.[10] The lowest energy structure of the monohydrate complex corresponds to hydration at the phenolate oxygen (Ia). Hydration at the imidazole oxygen is *ca*. 100 meV higher in energy, with the oxygen lone pair being able to weakly bind to either the nearest methyl group (Ib) or to the CH group of the methine bridge (Ic).

A coarse estimate of the relative populations of the two binding sites was achieved by fitting the two H-bonded OH features with Gaussian profiles and comparing the areas, scaled by the calculated IR intensities for conformers Ia and Ib. The result suggests that *ca*. 60% of the complexes exist with the water bound to the phenolate group and *ca*. 40% have the water bound to the imidazole group. We note that this ratio is not consistent with a thermal population. One possible explanation for this behavior is through the differing binding energies of water molecules to each site. In principle, the larger binding energy at the phenolate site (calculated at 4550 cm^{-1}) could suppress the fragment ion signal generated from this complex compared to that of the complex with the water bound to the imidazole (binding energy calculated at 3740 cm^{-1}). However, as noted previously, there is considerable internal energy in the complexes, because they are formed from an evaporative ensemble.[37] The internal energy in a complex formed this way is on the order of the binding energy of a water molecule in the dihydrate, which is calculated between 3300 cm^{-1} and 4500 cm^{-1}. As a result, the internal energy of the complex assists in dissociation after photon absorption. This is also reflected in the fact that we are able to record IR spectra in and below the carbonyl stretching region (see Figure 4.8). A more plausible explanation for the deviation of the population ratio from that of a thermal distribution is that migration of water molecules between the two binding sites involves breaking of the hydrogen bond to the ion. Interconversion between the two binding sites is therefore likely to be hindered by a large barrier, leading to kinetically trapped species. This means that the population ratio is better described by a cross section for the capture of a water molecule by the two different binding cites. Future experiments could employ a separation of water adduct formation and messenger tagging,[42] together with hole-burning spectroscopy[43-44] to allow observation and assignment of individual hydration conformers.

The spectrum of the dihydrate species in the OH stretching region is presented in Figure 4.14 and is remarkably similar to that of the monohydrate. It is again dominated by two broad features at 3190 cm^{-1} and 3340 cm^{-1} corresponding to hydrogen bound OH stretches and again has the signature of the free OH stretching vibration at *ca*. 3700 cm^{-1}. The two water molecules can be either bonded to the same oxygen, or one to each binding site, resulting in three possible binding site occupation combinations. For each binding site occupation there are again several possible conformers due to the conformational flexibility within each site, and these conformers are all close in energy. Figure 4.15 shows a comparison of the experimental spectrum with several calculated conformers.

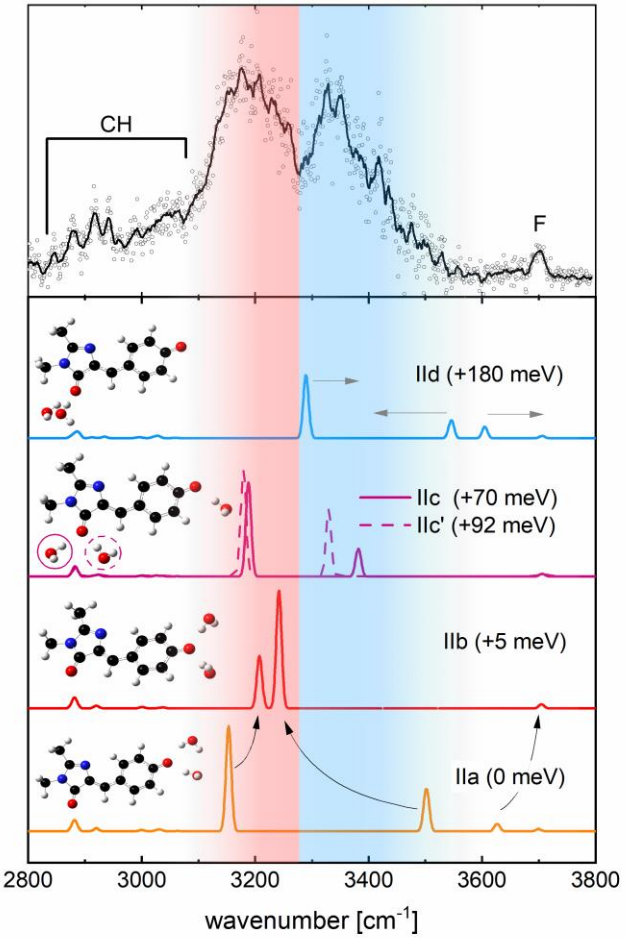

Figure 4.14. Calculated IR spectra of several conformers of $[HBDI\cdot(H_2O)_2]^-$ (lower traces), compared to the experimental spectrum (upper trace). The points in the upper trace are raw data, the full black line is an 11-point gliding average to guide the eye. The spectrum contains signatures for CH stretching vibrations (CH), OH stretching H-bonded to the phenolate (red-shaded region) and imidazole (blue-shaded region) groups, and the free OH stretching mode (F). All calculations have been scaled by 0.957 to match the experimentally observed free OH stretching vibrations. The calculated energies (at 0 K) of the conformers relative to the lowest energy conformer (IIa) are given in each simulated trace. Arrows in the lowest trace show how the infrared features of conformer IIa change as the H-bond between the water molecules is lost (see text). Arrows in the trace for conformer IId show the expected analogous behavior upon breaking the water-water H-bond for a conformer with both water molecules on the imidazole. The full and dashed lines in the trace for conformers IIc and IIc’ correspond to the water molecule positions indicated by full and dashed circles, respectively.

Conformer IIa is the lowest energy structure with both water molecules binding to the phenolate and forming a water-water hydrogen bond (see Figure 4.9). We note, however, that the experimental spectrum does not show any feature that would indicate a water-water hydrogen bond, which is predicted at *ca*. 3600 cm^{-1}. Experiments by Johnson and coworkers on $I^{-}\cdot(H_2O)_2$ showed that the water-water hydrogen bond in that cluster does not survive in trap temperatures in the present experiment, easily explaining the lack of this feature in our experiment.[45] Based on their work, we expect the two ionic hydrogen bond features to shift closer together (see arrows in lowest trace of Figure 4.14), behaving like independent monomers rather than dimers. The corresponding conformer (IIb) in the present case is a stable minimum energy structure, which is practically isoenergetic with IIa. At the internal energies present in these complexes, the higher entropy of conformer IIb will likely drive the breaking of the water-water hydrogen bond, and we expect that conformer IIa is not populated at this temperature. As a result, the lower frequency feature in the experimental trace is still due to hydration of the phenolate oxygen, while the higher energy feature is indicative of hydration of the imidazole moiety. Attempts at generating a stable structure with two independent water molecules bound to the imidazole moiety failed. We do, however, expect the same entropy driven loss of a water-water hydrogen bond to occur for this configuration, which will lead to the behavior indicated by the arrows shown in the trace of conformer IId in Figure 4.14. The experimental spectrum is again consistent with a mixture of hydration conformers, but we refrain from estimating the ratio of the different conformers due to the large number of possible structures. Hydration of the phenolate by both water molecules is lowest in energy, followed by hydration by one water at each binding site (+70 meV), with two water molecules on the imidazole being highest in energy (+180 meV), which is consistent with calculations by Krylov and coworkers.[10]

While $HBDI^-$ is hydrated at both the phenolate and imidazole moiety in our experiment, it is only hydrated at the phenolate in the protein. While this hinders the immediate comparison of hydration effects in clusters with hydration in the protein, it is still interesting to explore the effect of hydration on the electronic spectrum of $HBDI^-$. Figure 4.15 presents the electronic spectra for $HBDI^-$ at 30K and $[HBDI\cdot(H_2O)_n]^-$ (n = 1, 2) at 160 – 180 K. The band envelope for bare $HBDI^-$ and the singly hydrated species are strikingly similar. The vibronic features of the hydrated species are less well resolved than for bare $HBDI^-$, but we assign the band origin to a partially resolved peak at 20985 ± 30 cm^{-1}, which is only 55 cm^{-1} blue-shifted from bare $HBDI^-$. Additionally, we have a partially resolved peak at *ca.* 21120 cm^{-1} and a shoulder at 21195 cm^{-1}. These features are likely due to low-frequency bending motions of the methine bridge (see section 4.3). We also assign the set of peaks around 22200 cm^{-1} as an imidazole ring breathing/in-plane CH bending mode and its combination bands with the methine bridge bending mode. While the addition of a single water molecule has a minimal effect on the electronic spectrum of $HBDI^-$, the spectrum of the dihydrate exhibits a significantly altered envelope. Here we observe a broad feature around 21400 cm^{-1}, followed by another around 22130 cm^{-1}. It is impossible to extract a clean band origin from the spectrum, but we find that the half-maximum point on the rising edge of the first feature is blue shifted by *ca.* 180 cm^{-1} from the analogous point of the monohydrate envelope.

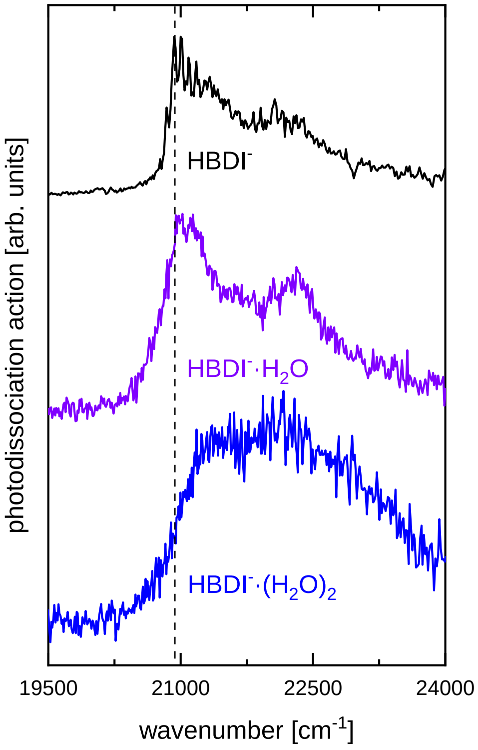

Figure 4.15. Electronic spectra of $HBDI^-$ at 30K and $[HBDI\cdot(H_2O)_n]^-$ ($n = 1, 2$). The photofragment signals were the loss of a methyl group for bare $HBDI^-$, and of all H_2O molecules for $[HBDI\cdot(H_2O)_n]^-$, respectively. The vertical dashed line marks the band origin of bare $HBDI^-$ at 20930 cm^{-1}.

We assume the vertical excitation energies are equal to the band origin energies in the FC region based on the discussion of the bare $HBDI^-$ spectrum, where the calculations predict a shallow minimum energy geometry on the S_1 potential energy surface. Our calculations, done at the CAM-B3LYP/def2-TZVPP level of theory, predict a shift of -9 cm^{-1} and +54 cm^{-1} for hydration at the phenolate and imidazole oxygen, respectively. This is in contrast to calculations done by Krylov and coworkers[10] at the SOS-CIS(D)/cc-pVTZ level of theory which predicted a shift of +240 cm^{-1} and -160 cm^{-1} upon hydration at the phenolate and imidazole oxygen, respectively. The first feature in the monohydrate spectrum (at *ca*. 20985 cm^{-1}), which is broader than that of bare $HBDI^-$, likely contains the band origin of both hydration conformers. The splitting between the calculated band origins in our calculations are consistent with the experimental width of this feature, although this agreement is likely fortuitous, while the splitting calculated by the Krylov group is too large to fit the experimentally observed width of the FC profile.

Calculations of vertical excitation energies for the three hydration families of the dihydrate span *ca*. 300 cm^{-1} (see Table 4.4 for a summary), and some are red shifted from that of the bare ion. These calculations do not explain the observed blue shift in the experimental spectrum or the deviation from the characteristic envelope of $HBDI^-$. It is likely that the change in envelope of the dihydrate spectrum is at least in part due to a mixture of hydration conformers. However, because of the many complications arising from the mixture of conformers and the lack of a clear computational description, we refrain from a more definitive assignment. We note that the dramatic shift induced by the second water molecule is unexpected, as most often the first one or two molecules induce a significant change, while additional water molecules have less pronounced effects.[46-47] This is clearly not the case here, where the second water molecule brings the electronic spectrum significantly closer to bulk solution than the first.

Figure 4.16 is a summary of all the electronic spectra we have discussed thus far, along with a comparison to the spectrum of GFP taken at 77 K[48] and that of $HBDI^-$ in aqueous solution. The figure shows the striking similarity of the absorption band envelopes of $HBDI^-$ in the protein and *in vacuo*, even when solvated by a single water molecule. As discussed previously, addition of a second water molecule shifts the band dramatically towards the solution spectrum. This highlights the value of experiments done on isolated chromophores. Not only can they provide a clean access to intrinsic photophysics, but also solution phase data can be representative of entirely different behavior than that of a protein environment.

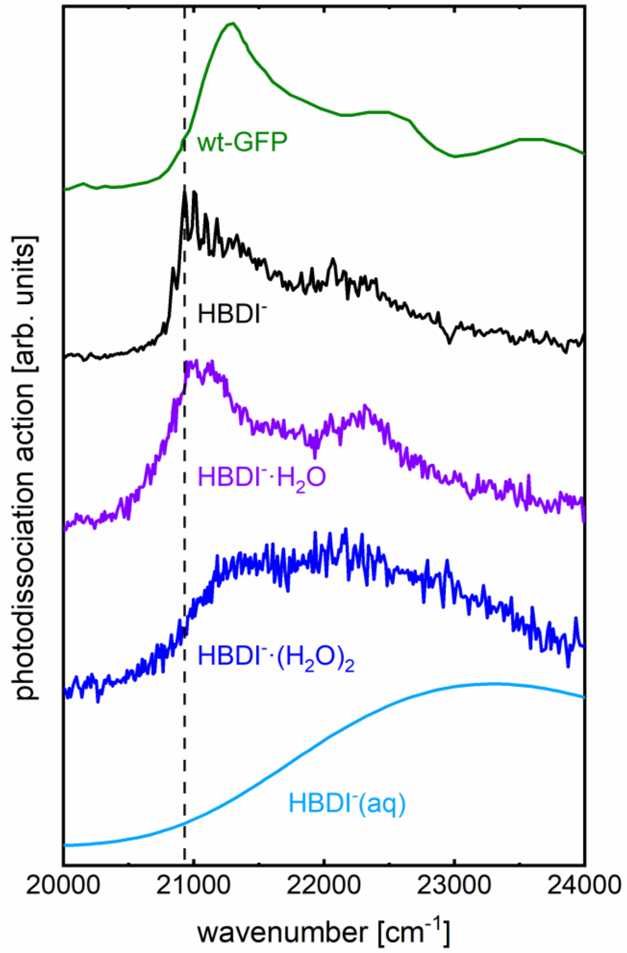

Figure 4.16. From top: Absorption spectrum of wild-type GFP at 77 K (green); photodissociation spectra of $HBDI^-$ at 30K (black) and $[HBDI\cdot(H_2O)_n]^-$ ($n = 1, 2$, magenta and blue) in the visible spectral region; UV/vis absorption spectrum of aqueous $HBDI^-$ at pH 11. All traces were normalized to the same peak height. Photofragment signals were the loss of a methyl group for bare $HBDI^-$, and of all H_2O molecules for $[HBDI\cdot(H_2O)_n]^-$, respectively. The vertical dashed line marks the band origin of bare $HBDI^-$ at 20930 cm^{-1}. The absorption spectrum of wild-type GFP was digitized from ref.[48]

4.5 Hot band assisted infrared spectroscopy

In the visible and UV regions of the electromagnetic spectrum, absorption of one or two photons is often sufficient to lead to photodissociation of a given molecule, but this is not typically the case for IR spectroscopy, since the bond dissociation energy of most molecules is significantly larger than the energy deposited by one or two IR photons. Therefore, to take IR photodissociation spectra of molecules, one must form weakly bound complexes with molecules like N_2, with binding energies on the order of a few hundred cm^{-1}. Combining the absorption of an IR photon with absorption of a UV photon, or photons, leads to a set of IR-UV double reesonance methods which can be used to investigate the structures of molecules. Though these methods require the implementation of two light sources, they are free from ion temperature limitations, difficulties in the preparation of messenger tagged species, and the technical requirements of infrared multiphoton dissociation (IRMPD) experiments, which typically require the use of expensive free electron lasers. There are several ways to carry out IR-UV double resonance spectroscopy, summarized in Figure 4.17. One such technique is referred to as ion dip spectroscopy (Figure 4.17.a) which involves tuning the UV/vis light source to a specific, narrow transition $|0\rangle \rightarrow |f\rangle$ starting from the electronic and vibrational ground state, $|0\rangle$, where fragmentation occurs upon electronic excitation into the fragmenting final state $|f\rangle$. One then monitors the fragment ion signal while tuning the infrared light source. When the infrared light source becomes resonant with a transition, the fragment ion signal dips as the population of $|0\rangle$ is depleted. Another technique is to tune the UV/vis light source to be on resonance with a specific vibrationally excited state $|vib\rangle$ to a specific vibronic resonance in the fragmenting state $|f\rangle$ $((|vib\rangle \rightarrow |f\rangle)$, true IR-UV double resonance (Figure 4.17.b).

In this chapter, we discuss another double resonance approach which works well for large ions due to their ability to undergo rapid intramolecular vibrational relaxation (IVR).[49] In this approach, the target molecule ($HBDI^-$ in our experiment) absorbs an infrared photon and undergoes IVR, resulting in a hot ion with nowhere for the excess energy to go. The distribution of energy depends on the time after absorption and is not necessarily a thermal distribution. We then tune the UV/vis photon to an energy where hot bands are found in the UV/vis spectrum of $HBDI^-$, which results in excitation into the fragmenting state $|f\rangle$ (Figure 4.17.c), here the S_1 state. We refer to this technique as hot band assisted IR (HAIR) spectroscopy, and note it is sometimes referred to as IR-UV gain spectroscopy in the literature.

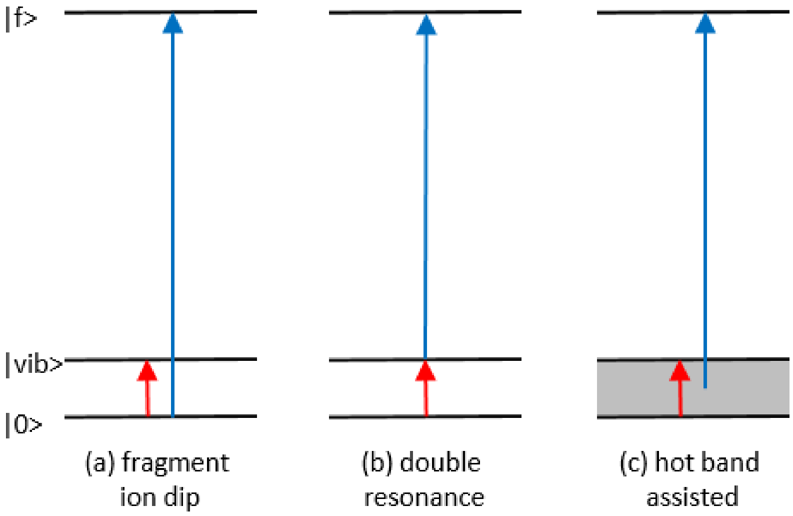

Figure 4.17. Excitation schemes for resonant IR-UV 2-photon photodissociation spectroscopy. Fragmentation occurs upon excitation to state $|f\rangle$.

In Section 4.3 we posed the possibility of the increase of intensity on the low energy side of the band origin region of the electronic spectrum observed for $HBDI^-$ as a function of increasing temperature being due to the development of a population of the E isomer, which has been observed in room temperature ion mobility experiments.[13] To address this question, we will use HAIR spectroscopy to investigate the temperature dependence of the IR spectra of $HBDI^-$.

This type of spectroscopy requires a slight modification to our experimental operation, as both infrared and visible light pulses will interact with the target ions. The two beam paths are spatially separated by 8 cm, and the infrared pulse irradiates the target molecules *ca.*1.5 μs before the visible pulse (parent ion kinetic energies are *ca.* 3.2 keV, the mass of the ion is 215 u). The mass spectrometer and visible OPO are operated at a repetition rate of 20 Hz, while the IR light source is fired every other experimental cycle (10 Hz). This provides photodissociation signals with and without IR irradiation, and the difference between these signals can be traced to the absorption of IR light.

Figure 4.18 shows a comparison between the electronic spectrum of HBDI$^-$ at 30 K and 300 K, focusing on the $S_0 \rightarrow S_1$ band origin at 20930 cm^{-1}. These spectra, discussed in Section 4.3, were taken without prior exposure to infrared irradiation. Comparing the two reveals that the spectral region below *ca*. 20750 cm^{-1} contains only hot bands and shows no absorption features at low temperatures. We use this region of the spectrum as a probe for infrared spectroscopy in the HAIR approach.

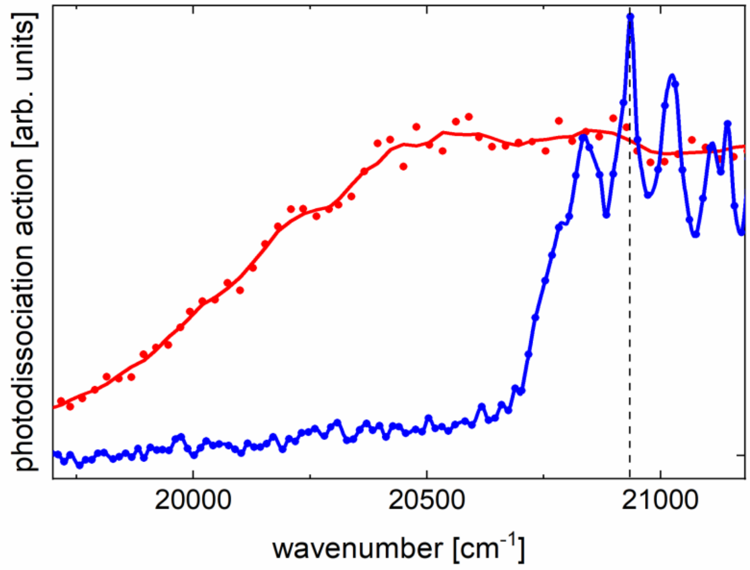

Figure 4.18. UV-Vis spectra of HBDI$^-$ at 300K (red trace) and 30K (blue trace) in the band origin region. The dots are data points, the lines are a 5-point adjacent average (300 K) and an Akima spline (30 K) to guide the eye. The dashed vertical line shows the band origin at 20930 cm^{-1}. Note that no IR irradiation was done to acquire these spectra.

Absorption of an infrared photon prior to electronic excitation adds vibrational energy into the molecule, which leads to an increase of intensity in hot bands, compared to irradiation by visible photons only. This effect is demonstrated in Figure 4.19. The increase in hot band intensity due to infrared irradiation is observable for all trap temperatures studied here, from 30 K to 300 K, which allows us to record infrared spectra of $HBDI^-$ at any temperature in this range. This would not be feasible relying on messenger tagging, given the narrow range of temperatures for attaching messenger species (e.g., 25 K – 40 K for N_2 in our experiment). As can be seen in Figure 4.19, the infrared-generated hot bands are more pronounced at low trap temperature than at high temperature, and the signal-to-noise ratio is correspondingly higher at low temperature.

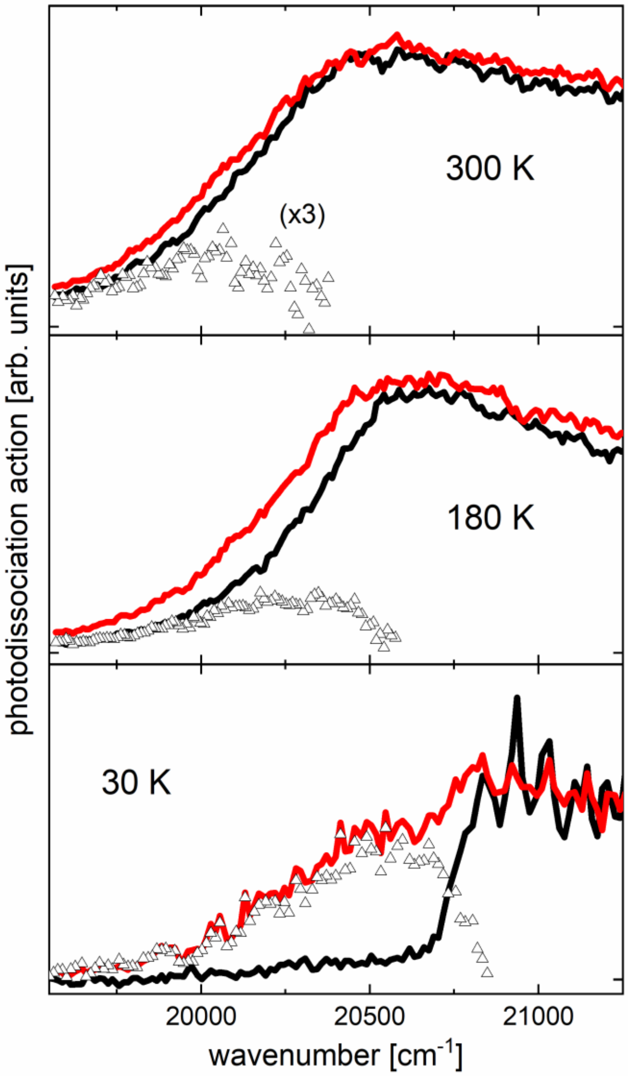

Figure 4.19. Electronic spectra in the S_1 band origin region of HBDI$^-$ at 30, 180, and 300 K trap temperatures. Full lines are spectra without (black) and with (red) resonant IR irradiation at 1536 cm^{-1}; open triangles show the difference between the two signals, where the difference values for 300 K have been amplified by a factor 3 for clarity.

Figure 4.20 shows the HAIR spectra of HBDI$^-$ in the carbonyl stretching region at various temperatures, compared to that of the N_2 messenger tagged spectrum. Calculated spectra for the E and Z isomers of HBDI are also presented. The spectra show a weak temperature dependence of the IR signatures. The peaks at 1544 cm^{-1} and 1600 cm^{-1} shift by -5 cm^{-1} and -7 cm^{-1} respectively over the range of 30 K to 300 K trap temperature. Recall from Section 4.3, the electronic spectrum of HBDI$^-$ had developed a partially resolved peak at 20700 cm^{-1} at 180 K. The shifts of both the 1544 cm^{-1}and 1600 cm^{-1} feature are nearly indiscernible at 180 K. The peak at 1680 cm^{-1} broadens with increasing temperature, until at 300 K it is no longer clearly observable.

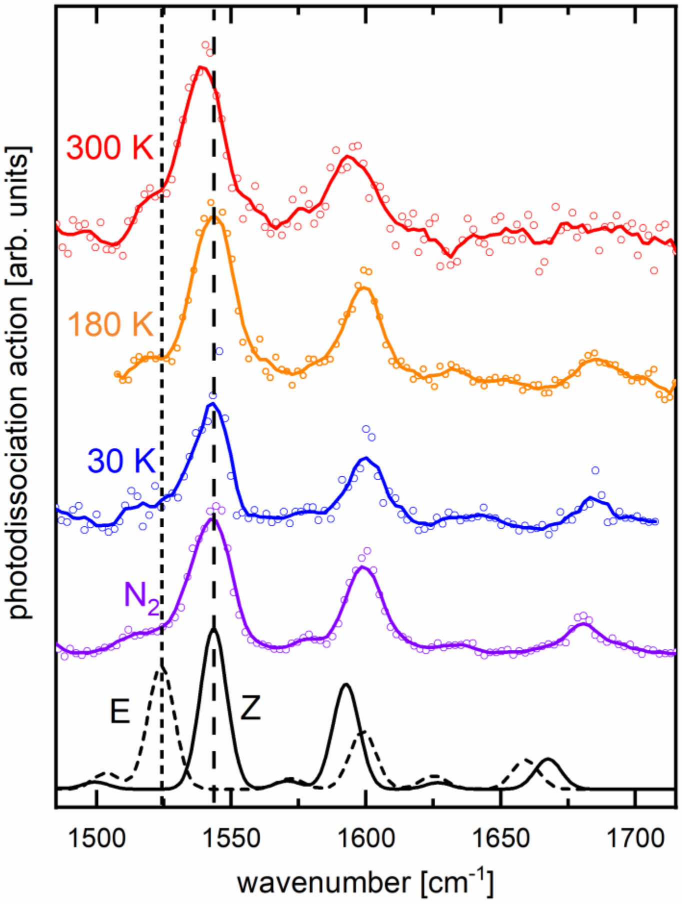

Figure 4.20. Infrared spectra of HBDI$^-$ under different conditions. The lowest traces are simulated spectra for the dominant Z isomer (full black line) and the E isomer (dotted black line). The other traces show experimental infrared spectra using N_2 tagging and HAIR data for different trap temperatures as indicated on the traces. Open circles are raw data points, the full lines are 5-point adjacent averages. The vertical lines show the calculated band positions of the dominant band for the Z and E isomers. The HAIR spectra were acquired at 20580 cm^{-1}, 20160 cm^{-1}, and 19800 cm^{-1} for 30 K, 180 K, and 300 K trap temperature, respectively.

To understand the decrease in HAIR signal with increasing temperature, we consider the temperature dependence of the vibrational molecular heat capacity and assume that IVR results in a thermal distribution of energy throughout the vibrational modes of the molecule by time the visible irradiation arrives (*ca*. 1.5 μs after irradiation by the IR source). Figure 4.21 shows the temperature dependence of the vibrational contributions to the internal energy (U_{vib}), which was calculated from equation (1), and constant volume heat capacity ($C_{V,vib}$), which is simply the temperature derivative of (1), of HBDI$^-$.

$$U_{vib} = \sum_j \frac{\hbar\omega_j}{e^{\hbar\omega_j/k_BT} - 1} \tag{1}$$

Here ω_j are the frequencies of the vibrational modes (obtained from harmonic frequency calculations), $\hbar$ is the reduced Planck constant, k_B is the Boltzmann constant, and T is the temperature. If we consider an ion of initial temperature of 30 K absorbing a single IR photon of frequency 1000 cm^{-1}, after IVR, this increase in internal energy represents a substantial increase in the molecular temperature (demonstrated by the blue dots in Figure 4.21). If we instead consider an ion with an initial temperature of 300 K absorbing that same 1000 cm^{-1} photon, the change in ion temperature is less pronounced (demonstrated by the orange dots in Figure 4.21) as the heat capacity has increased. Therefore, the HAIR intensity will in general be more difficult to measure with higher starting temperatures due to the relatively small change in ion temperature resulting from absorption of the IR photon. This problem is exacerbated when dealing with larger molecules, which have correspondingly larger heat capacities to begin with, and when dealing with relatively low energy photons.

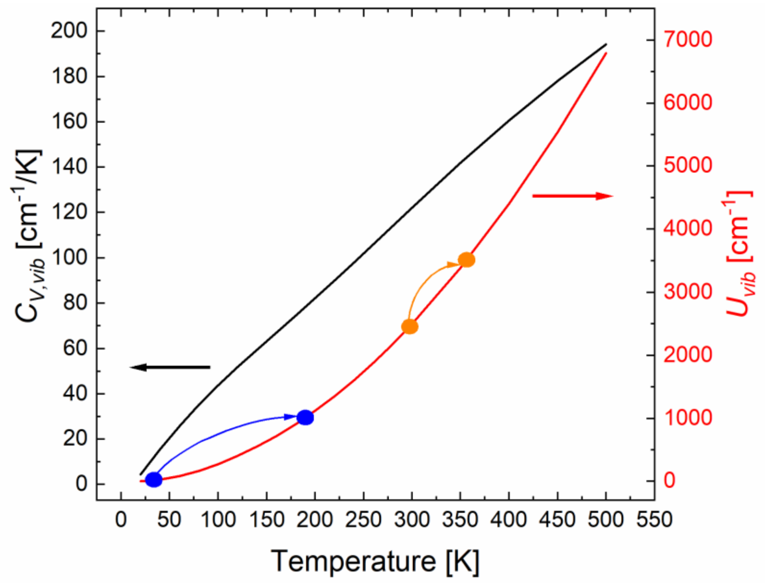

Figure 4.21. Constant volume heat capacity (black trace) and average vibrational internal energy (red trace) of HBDI$^-$ as a function of temperature. The circles and curved arrows show the change in molecular temperature upon absorption of a 1000 cm^{-1} infrared photon, starting from 30 K (blue) and from 300 K (orange). The horizontal arrows indicate which curve belongs to which vertical scale.

We present the carbonyl stretching region in Figure 4.20 because this region was used in the initial *Z* isomer assignment in Section 4.3, based on the spacing of the three dominate features. We observe neither a significant change in the spacing between these features of the spectrum at 180 K, nor the emergence of any new features at that temperature, and therefore conclude the HAIR spectra do not suggest the development of a population of the *E* isomer.

This leaves the questions about temperature dependence of the electronic spectrum of HBDI$^-$ unanswered, specifically the observation that behavior of the low energy side of the absorption band that was not recovered by FC simulations. This behavior is reminiscent of those observed by Roithova and coworkers[50] who found a pronounced temperature dependence of the spectra of rhodamine 123, which was also not recoverable by FC simulations. They concluded that the cause of this dependence lies in the fact that photodissociation required 3-4 photons. An efficient return to the ground state after successive absorption events resulted in an increase of vibrational temperature of the ions for the absorption of all photons after the first, drastically skewing the spectrum towards lower photon energies. These effects would not be accounted for by FC simulations. We assume similar processes are affecting the spectrum of $HBDI^-$, since two photons are required for photodissociation in the S_1 band origin region. $HBDI^-$ is known to undergo radiationless relaxation with ps lifetime[7-8, 19, 23-24, 27, 51] after absorption of the first photon, which results in the population of vibrationally hot ions in the electronic ground state, which then absorb the second photon. A simple FC simulation is unlikely to predict the spectral envelope in these circumstances.

4.6 References

1. Chalfie, M.; Tu, Y.; Euskirchen, G.; Ward, W. W.; Prasher, D. C., Green Fluorescent Protein as a Marker for Gene-Expression. *Science* **1994,** *263* (5148), 802-805.
2. Chudakov, D. M.; Matz, M. V.; Lukyanov, S.; Lukyanov, K. A., Fluorescent Proteins and Their Applications in Imaging Living Cells and Tissues. *Physiological Reviews* **2010,** *90* (3), 1103-1163.
3. Day, R. N.; Davidson, M. W., The fluorescent protein palette: tools for cellular imaging. *Chem. Soc. Rev.* **2009,** *38* (10), 2887-2921.
4. Hein, B.; Willig, K. I.; Hell, S. W., Stimulated emission depletion (STED) nanoscopy of a fluorescent protein-labeled organelle inside a living cell. *Proceedings of the National Academy of Sciences of the United States of America* **2008,** *105* (38), 14271-14276.
5. Tsien, R. Y., The green fluorescent protein. *Annu. Rev. Biochem.* **1998,** *67*, 509-544.
6. Ormö, M.; Cubitt, A. B.; Kallio, K.; Gross, L. A.; Tsien, R. Y.; Remington, S. J., Crystal Structure of the Aequorea victoria Green Fluorescent Protein. *Science* **1996,** *273* (5280), 1392-1395.
7. Mandal, D.; Tahara, T.; Meech, S. R., Excited-state dynamics in the green fluorescent protein chromophore. *Journal of Physical Chemistry B* **2004,** *108* (3), 1102-1108.
8. Litvinenko, K. L.; Webber, N. M.; Meech, S. R., Internal conversion in the chromophore of the green fluorescent protein: Temperature dependence and isoviscosity analysis. *Journal of Physical Chemistry A* **2003,** *107* (15), 2616-2623.

9. Forbes, M. W.; Jockusch, R. A., Deactivation Pathways of an Isolated Green Fluorescent Protein Model Chromophore Studied by Electronic Action Spectroscopy. *Journal of the American Chemical Society* **2009,** *131* (47), 17038-+.

10. Zuev, D.; Bravaya, K. B.; Makarova, M. V.; Krylov, A. I., Effect of microhydration on the electronic structure of the chromophores of the photoactive yellow and green fluorescent proteins. *Journal of Chemical Physics* **2011,** *135* (19).

11. Henley, A.; Fielding, H. H., Anion photoelectron spectroscopy of protein chromophores. *International Reviews in Physical Chemistry* **2019,** *38* (1), 1-34.

12. Langeland, J.; Kjaer, C.; Andersen, L. H.; Nielsen, S. B., The Effect of an Electric Field on the Spectroscopic Properties of the Isolated Green Fluorescent Protein Chromophore Anion. *Chemphyschem* **2018,** *19* (14), 1686-1690.

13. Carrascosa, E.; Bull, J. N.; Scholz, M. S.; Coughlan, N. J. A.; Olsen, S.; Wille, U.; Bieske, E. J., Reversible Photoisomerization of the Isolated Green Fluorescent Protein Chromophore. *Journal of Physical Chemistry Letters* **2018,** *9* (10), 2647-2651.

14. Tay, J.; Parkes, M. A.; Addison, K.; Chan, Y. H.; Zhang, L. J.; Hailes, H. C.; Page, P. C. B.; Meech, S. R.; Blancafort, L.; Fielding, H. H., The Effect of Conjugation. on the Competition between Internal Conversion and Electron Detachment: A Comparison between Green Fluorescent and Red Kaede Protein Chromophores. *Journal of Physical Chemistry Letters* **2017,** *8* (4), 765-771.

15. McLaughlin, C.; Assmann, M.; Parkes, M. A.; Woodhouse, J. L.; Lewin, R.; Hailes, H. C.; Worth, G. A.; Fielding, H. H., ortho and para chromophores of green fluorescent protein: controlling electron emission and internal conversion. *Chemical Science* **2017,** *8* (2), 1621-1630.

16. Bochenkova, A. V.; Mooney, C. R. S.; Parkes, M. A.; Woodhouse, J. L.; Zhang, L. J.; Lewin, R.; Ward, J. M.; Hailes, H. C.; Andersen, L. H.; Fielding, H. H., Mechanism of resonant electron emission from the deprotonated GFP chromophore and its biomimetics. *Chemical Science* **2017,** *8* (4), 3154-3163.

17. Anstöter, C. S.; Dean, C. R.; Verlet, J. R. R., Chromophores of chromophores: a bottom-up Huckel picture of the excited states of photoactive proteins. *Physical Chemistry Chemical Physics* **2017,** *19* (44), 29772-29779.

18. Kiefer, H. V.; Pedersen, H. B.; Bochenkova, A. V.; Andersen, L. H., Decoupling Electronic versus Nuclear Photoresponse of Isolated Green Fluorescent Protein Chromophores Using Short Laser Pulses. *Physical Review Letters* **2016,** *117* (24).

19. Anstöter, C. S.; Bull, J. N.; Verlet, J. R. R., Ultrafast dynamics of temporary anions probed through the prism of photodetachment. *International Reviews in Physical Chemistry* **2016,** *35* (4), 509-538.

20. West, C. W.; Bull, J. N.; Hudson, A. S.; Cobb, S. L.; Verlet, J. R. R., Excited State Dynamics of the Isolated Green Fluorescent Protein Chromophore Anion Following UV Excitation. *Journal of Physical Chemistry B* **2015,** *119* (10), 3982-3987.

21. Mooney, C. R. S.; Parkes, M. A.; Zhang, L. J.; Hailes, H. C.; Simperler, A.; Bearpark, M. J.; Fielding, H. H., Competition between photodetachment and autodetachment of the 2(1)pi pi* state of the green fluorescent protein chromophore anion. *Journal of Chemical Physics* **2014,** *140* (20).

22. Bochenkova, A. V.; Klaerke, B.; Rahbek, D. B.; Rajput, J.; Toker, Y.; Andersen, L. H., UV Excited-State Photoresponse of Biochromophore Negative Ions. *Angewandte Chemie-International Edition* **2014,** *53* (37), 9797-9801.

23. Mooney, C. R. S.; Horke, D. A.; Chatterley, A. S.; Simperler, A.; Fielding, H. H.; Verlet, J. R. R., Taking the green fluorescence out of the protein: dynamics of the isolated GFP chromophore anion. *Chemical Science* **2013,** *4* (3), 921-927.

24. Bochenkova, A. V.; Andersen, L. H., Ultrafast dual photoresponse of isolated biological chromophores: link to the photoinduced mode-specific non-adiabatic dynamics in proteins. *Faraday Discussions* **2013,** *163*, 297-319.

25. Toker, Y.; Rahbek, D. B.; Klaerke, B.; Bochenkova, A. V.; Andersen, L. H., Direct and Indirect Electron Emission from the Green Fluorescent Protein Chromophore. *Physical Review Letters* **2012,** *109* (12).

26. Mooney, C. R. S.; Sanz, M. E.; McKay, A. R.; Fitzmaurice, R. J.; Aliev, A. E.; Caddick, S.; Fielding, H. H., Photodetachment Spectra of Deprotonated Fluorescent Protein Chromophore Anions. *Journal of Physical Chemistry A* **2012,** *116* (30), 7943-7949.

27. Horke, D. A.; Verlet, J. R. R., Photoelectron spectroscopy of the model GFP chromophore anion. *Physical Chemistry Chemical Physics* **2012,** *14* (24), 8511-8515.

28. Forbes, M. W.; Nagy, A. M.; Jockusch, R. A., Photofragmentation of and electron photodetachment from a GFP model chromophore in a quadrupole ion trap. *International Journal of Mass Spectrometry* **2011,** *308* (2-3), 155-166.

29. Chingin, K.; Balabin, R. M.; Frankevich, V.; Barylyuk, K.; Nieckarz, R.; Sagulenko, P.; Zenobi, R., Absorption of the green fluorescent protein chromophore anion in the gas phase studied by a combination of FTICR mass spectrometry with laser-induced photodissociation spectroscopy. *International Journal of Mass Spectrometry* **2011,** *306* (2-3), 241-245.

30. Lammich, L.; Petersen, M. A.; Nielsen, M. B.; Andersen, L. H., The gas-phase absorption spectrum of a neutral GFP model chromophore. *Biophysical Journal* **2007,** *92* (1), 201-207.

31. Andersen, L. H.; Lapierre, A.; Nielsen, S. B.; Nielsen, I. B.; Pedersen, S. U.; Pedersen, U. V.; Tomita, S., Chromophores of the green fluorescent protein studied in the gas phase. *European Physical Journal D* **2002,** *20* (3), 597-600.

32. Nielsen, S. B.; Lapierre, A.; Andersen, J. U.; Pedersen, U. V.; Tomita, S.; Andersen, L. H., Absorption spectrum of the green fluorescent protein chromophore anion in vacuo. *Physical Review Letters* **2001,** *87* (22).

33. Andersen, L. H.; Bluhme, H.; Boye, S.; Jorgensen, T. J. D.; Krogh, H.; Nielsen, I. B.; Nielsen, S. B.; Svendsen, A., Experimental studies of the photophysics of gas-phase fluorescent protein chromophores. *Physical Chemistry Chemical Physics* **2004,** *6* (10), 2617-2627.

34. Deng, S. H. M.; Kong, X. Y.; Zhang, G. X.; Yang, Y.; Zheng, W. J.; Sun, Z. R.; Zhang, D. Q.; Wang, X. B., Vibrationally Resolved Photoelectron Spectroscopy of the Model GFP Chromophore Anion Revealing the Photoexcited S-1 State Being Both Vertically and Adiabatically Bound against the Photodetached D-0 Continuum. *Journal of Physical Chemistry Letters* **2014,** *5* (12), 2155-2159.

35. West, C. W.; Hudson, A. S.; Cobb, S. L.; Verlet, J. R. R., Communication: Autodetachment versus internal conversion from the S-1 state of the isolated GFP chromophore anion. *Journal of Chemical Physics* **2013,** *139* (7).

36. Almasian, M.; Grzetic, J.; Berden, G.; Bakker, B.; Buma, W. J.; Oomens, J., Gas-phase infrared spectrum of the anionic GFP-chromophore. *International Journal of Mass Spectrometry* **2012,** *330*, 118-123.

37. Klots, C. E., TEMPERATURES OF EVAPORATING CLUSTERS. *Nature* **1987,** *327* (6119), 222-223.

38. Kamarchik, E.; Krylov, A. I., Non-Condon Effects in the One- and Two-Photon Absorption Spectra of the Green Fluorescent Protein. *Journal of Physical Chemistry Letters* **2011,** *2* (5), 488-492.

39. Martin, M. E.; Negri, F.; Olivucci, M., Origin, nature, and fate of the fluorescent state of the green fluorescent protein chromophore at the CASPT2//CASSCF resolution. *Journal of the American Chemical Society* **2004,** *126* (17), 5452-5464.

40. Bublitz, G.; King, B. A.; Boxer, S. G., Electronic structure of the chromophore in green fluorescent protein (GFP). *Journal of the American Chemical Society* **1998,** *120* (36), 9370-9371.

41. Ormö, M.; Cubitt, A. B.; Kallio, K.; Gross, L. A.; Tsien, R. Y.; Remington, S. J., Crystal Structure of the Aequorea victoria Green Fluorescent Protein. *Science* **1996,** *273* (5280), 1392.

42. Marsh, B. M.; Voss, J. M.; Garand, E., A dual cryogenic ion trap spectrometer for the formation and characterization of solvated ionic clusters. *Journal of Chemical Physics* **2015,** *143* (20), 1-7.

43. Voss, J. M.; Fischer, K. C.; Garand, E., Revealing the structure of isolated peptides: IR-IR predissociation spectroscopy of protonated triglycine isomers. *Journal of Molecular Spectroscopy* **2018,** *347*, 28-34.

44. Elliott, B. M.; Relph, R. A.; Roscioli, J. R.; Bopp, J. C.; Gardenier, G. H.; Guasco, T. L.; Johnson, M. A., Isolating the spectra of cluster ion isomers using Ar-"tag" -mediated IR-IR double resonance within the vibrational manifolds: Application to NO2-center dot H2O. *Journal of Chemical Physics* **2008,** *129* (9).

45. Wolke, C. T.; Menges, F. S.; Totsch, N.; Gorlova, O.; Fournier, J. A.; Weddle, G. H.; Johnson, M. A.; Heine, N.; Esser, T. K.; Knorke, H.; Asmis, K. R.; McCoy, A. B.; Arismendi-Arrieta, D. J.; Prosmiti, R.; Paesani, F., Thermodynamics of Water Dimer Dissociation in the Primary Hydration Shell of the Iodide Ion with Temperature-Dependent Vibrational Predissociation Spectroscopy. *Journal of Physical Chemistry A* **2015,** *119* (10), 1859-1866.

46. Xu, S.; Smith, J. E. T.; Weber, J. M., Hydration of a Binding Site with Restricted Solvent Access – Solvatochromic Shift of the Electronic Spectrum of a Ruthenium Polypyridine Complex, One Molecule at a Time. *J. Phys. Chem. A* **2016,** *120*, 7650–7658.

47. Støchkel, K.; Hansen, C. N.; Houmøller, J.; Nielsen, L. M.; Anggara, K.; Linares, M.; Norman, P.; Nogueira, F.; Maltsev, O. V.; Hintermann, L.; Nielsen, S. B.; Naumov, P.; Milne, B. F., On the Influence of Water on the Electronic Structure of Firefly Oxyluciferin Anions from Absorption Spectroscopy of Bare and Monohydrated Ions in Vacuo. *Journal of the American Chemical Society* **2013,** *135* (17), 6485-6493.

48. Chattoraj, M.; King, B. A.; Bublitz, G. U.; Boxer, S. G., Ultra-fast excited state dynamics in green fluorescent protein: Multiple states and proton transfer. *Proceedings of the National Academy of Sciences of the United States of America* **1996,** *93* (16), 8362-8367.

49. Nagornova, N. S.; Rizzo, T. R.; Boyarkin, O. V., Exploring the Mechanism of IR–UV Double-Resonance for Quantitative Spectroscopy of Protonated Polypeptides and Proteins. *Angewandte Chemie International Edition* **2013,** *52* (23), 6002-6005.

50. Navrátil, R.; Jašík, J.; Roithová, J., Visible photodissociation spectra of gaseous rhodamine ions: Effects of temperature and tagging. *Journal of Molecular Spectroscopy* **2017,** *332*, 52-58.

51. Voliani, V.; Bizzarri, R.; Nifosi, R.; Abbruzzetti, S.; Grandi, E.; Viappiani, C.; Beltram, F., Cis-trans photoisomerization of fluorescent-protein chromophores. *Journal of Physical Chemistry B* **2008,** *112* (34), 10714-10722.

Chapter 5 Protoporphyrin

This chapter has been adapted from Ref.[1] with permission from the PCCP Owner Societies.

5.1 Introduction

Porphyrins are a class of macrocycles with a characteristically intense visible absorption and are a vital component of many biological processes such as participating in electronic/chemical transport,[2] and photosynthesis,[3] among others. Their abundance in biology has prompted many efforts to apply them in areas centered around their visible absorption properties such as photosensitizers in solar cells,[4-5] photocatalysts for CO_2 reduction,[6-7] and as candidates for non-linear optical materials[8] to name a few. Optimization of these applications requires a thorough understanding of the intrinsic electronic structure of the porphyrin system being used, as well as how interaction with the chemical environment can affect their properties.

Porphyrins are tetrapyrroles (four pyrrole rings connected by methine bridges forming an extended conjugated system) which form a conjugated ring. Varieties exist with or without a metal atom in the center (see Figure 5.1). The incredible biological versatility is introduced by modifying the side chains of the pyrrole rings or changing the metal center if one is present. The simplest way to model the electronic properties of a porphyrin ring is by treating the 18 π electrons as particles on a ring. This was used by Gouterman[9-10] to develop the four-orbital model which predicts two separate pairs of degenerate transitions, where the lower energy pair is weaker and is referred to as the Q band, and the higher energy pair is more intense and is referred to as the B or Soret band. While the Soret band typically presents as a single, wide feature, the Q band typically consists of two features spaced by *ca*. 1500 cm^{-1}, which are part of the vibronic progression. These two features are resolved even in low-resolution spectra. The Q band appears either in of two patterns, which are named after the symmetries of the macrocycles as the D_{4h} and the D_{2h} pattern (see Figure 5.1). The D_{4h} pattern consists of a single set of two features and is observed primarily in the spectra of metalloporphyrins, where the macrocycle has approximate D_{4h} symmetry. This spectral pattern can also be achieved by protonating all 4 of the pyrrole nitrogen atoms. The D_{2h} pattern appears if the metal center is removed and only two of the pyrrole nitrogen atoms are protonated, thus lowering the symmetry and breaking degeneracy of the electronic state giving rise to the Q band. This leads to the observation of two separate pairs of features, which are referred to as the Q_x and Q_y bands. The B band undergoes an analogous splitting and gives rise to a B_x and B_y band, though typically the splitting in these bands is too small to be observed, and is outside the spectral range considered in the present experiment. The D_{2h} pattern is also referred to as the free-base pattern and is found in the case of protoporphyrin IX (PP), which is the focus of this chapter.

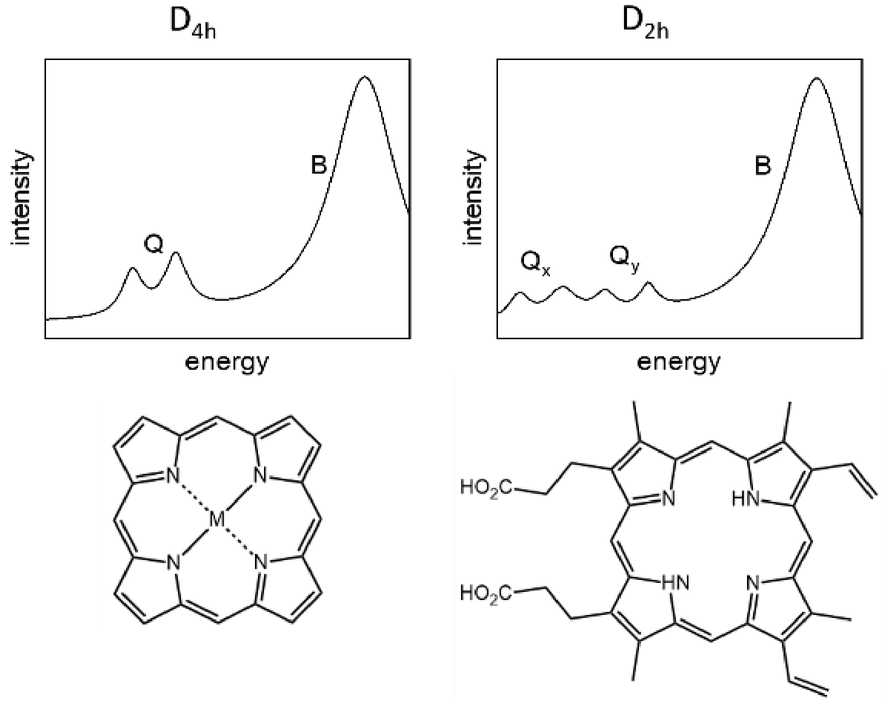

Figure 5.1. D_{4h} and D_{2h} macrocycle structures and their schematic electronic spectra for a general metalloporphyrin (left) and protoporphyrin IX (right).

The electronic structure of porphyrin systems has been studied for decades[9, 11-14], including that of PP.[15] Many of these experiments were performed at room temperature in solutions, causing vibronic structure, beyond the previously mentioned characteristic two-peak structure of the Q band, to largely be obscured by hot bands and solvent effects. PP has an added complication in that it is amphiphilic and forms polydisperse aggregates in aqueous solution, with a pH dependent number of monomer units.[16] Porphyrins have also been studied extensively in cryogenic matrices[9, 15] which were able to provide vibronic resolution, but in these experiments each absorption feature appears as a multiplet, due to matrix effects, complicating interpretation. As a result, condensed-phase results are difficult to interpret and do not reflect the intrinsic photophysics of this chromophore.

Experiments have been done on PP in gaseous environments as well. Brøndsted-Nielsen and coworkers[17] investigated the PP Q bands in an experiment similar to ours but at room temperature and they were unable to observe the lowest energy peak of the Q_x signature. The features of the vibronic progression they did observe were unresolved due to the elevated temperature. Experiments have also been done on neutral PP using supersonic jet techniques which yielded congested spectra,[18] likely due to incomplete vibrational cooling. In general, an electronic spectrum in the Q band region of PP with vibronic resolution has remained elusive, leaving key details about the intrinsic photophysics of this important species unknown.

Here we present the electronic spectra of cryogenically prepared PP in a singly and doubly deprotonated form, where we achieve vibronic resolution of the Q bands. Additionally, we are able to investigate the electronic Stark effect, a shift of the electronic bands induced by the electric field of a charge, or set of charges, located only a few Å away from the conjugated macrocycle, which is on the order of 10^9 V/m. We also present infrared spectra of both deprotonated species to assess structural differences.

5.2 Computational

Ground and S_1 excited state geometry optimizations and harmonic frequency calculations of PP and porphine (a simplified model of PP) were performed using DFT at the CAM-B3LYP/cc-pVDZ level of theory. Vertical transition energies of the S_1 and S_2 states were calculated using TDDFT with both the ωB97XD and CAM-B3LYP functionals and the cc-pVDZ basis sets after ground state optimization with the same functionals/basis sets.

Results from these calculations were then used to perform Franck-Condon-Herzberg-Teller (FCHT) simulations. We interpret our experimental spectrum using the FCHT simulation for porphine. We employed the vertical gradient approximation[19] when performing FCHT simulations of PP in the S_1 state, as calculations on PP not done under this approximation lead to a failure to construct a Duschinsky rotation matrix. All FCHT simulations were done at 0 K, and all DFT, TDDFT, and FCHT simulations were performed using Gaussian 16.

We also used multireference methods to calculate the vertical excitation energies as previous work has shown that CASSCF/NEVPT2 calculations predict the excitation energies of the Q bands well,[20-21] and Angeli et al. note that using an active space of 4 electrons in 4 orbitals provides nearly quantitative splitting of the Q bands.[22] The active space for all reference wave functions was chosen to include the two highest (and lowest) lying doubly occupied (and unoccupied) π-orbitals from the conjugated system of PP and the reference wave functions were generated using state averaged CASSCF (denoted SA-N-CASSCF, where N is the number of states averaged). The energies of these wave functions were corrected using NEVPT2.[23-25] Exploratory calculations were performed averaging 3 (X, Q_x, Q_y) and 5 states (X, Q_x, Q_y, B_x, B_y). Both results are reported here as both produced qualitatively similar results with the N = 3 case providing the best agreement with experiment. All correlated calculations used the cc-pVDZ basis set, were performed using the PySCF[26-28] package, and were checked with the ORCA[29-30] package. All multireference calculations were performed by James E. T. Smith in the group of Prof. Sandeep Sharma.

5.3 Discussion

Figure 5.2 shows the D_{2h} patterned electronic spectrum of $[(PP–H)\cdot N_2]^-$ in the Q band region. The experimental spectrum fails to return to baseline on the high energy end of the spectrum which we attribute to the onset of the Soret band. The Q_x band origin is at 15868 ±10

cm^{-1} and is followed by a vibronic progression that extends about 2000 cm^{-1}. The Q_y band origin is at 18760 ± 30 cm^{-1} and has a similar, though less resolved, vibronic progression. This reduction of resolution is likely due to a shorter lifetime of the S_2 state. Exploratory measurements on the complex with two N_2 molecules attached indicate a *ca.* 10 cm^{-1} induced shift of the band origin per N_2 adduct.

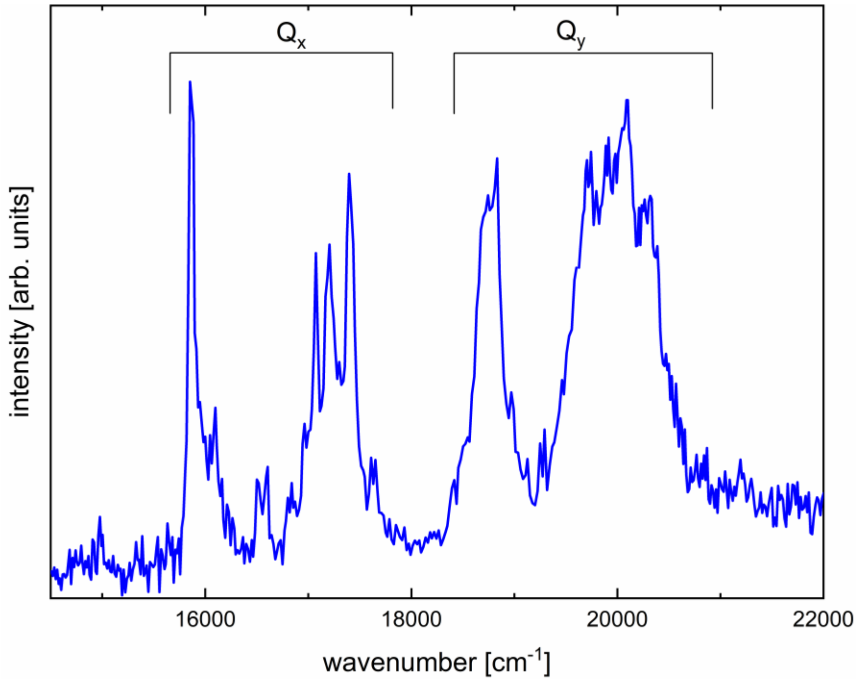

Figure 5.2. Electronic spectrum of $[(PP–H)\cdot N_2]^-$, showing the Q_x and Q_y absorption bands. The Q_x band origin is at 15868 ±10 cm^{-1}, and the Q_y band origin is at 18760 ± 30 cm^{-1}. Both band origins exhibit a qualitatively similar vibronic progression which extends ca. 2000 cm^{-1} above each origin.

Figure 5.3 shows the Q_x band of the experimental electronic spectrum (blue trace) along with the FCHT simulation for porphine (black trace) and $(PP-H)^-$ (green trace). Recall, the FCHT simulation for $(PP-H)^-$ was done under the vertical gradient approximation. Both simulations acceptably recover the experimental pattern, however the porphine simulation has a slightly better match. This suggests that the observed vibronic progression is primarily due to excitations in the vibrational modes of the macrocycle, rather than the propionic side chains. This is consistent with the observation of the same general Q band structure (and spacing) for most porphyrins, as was discussed in the introduction. Others have shown previously that while the Herzberg-Teller treatment underestimates the relative intensity of the band origin, it does produce a better match with the vibronic progression in general when compared to FC simulations.[12] FC simulations do however capture the experimental band origin behavior well, and establish the vertical transition energies at the band origin.

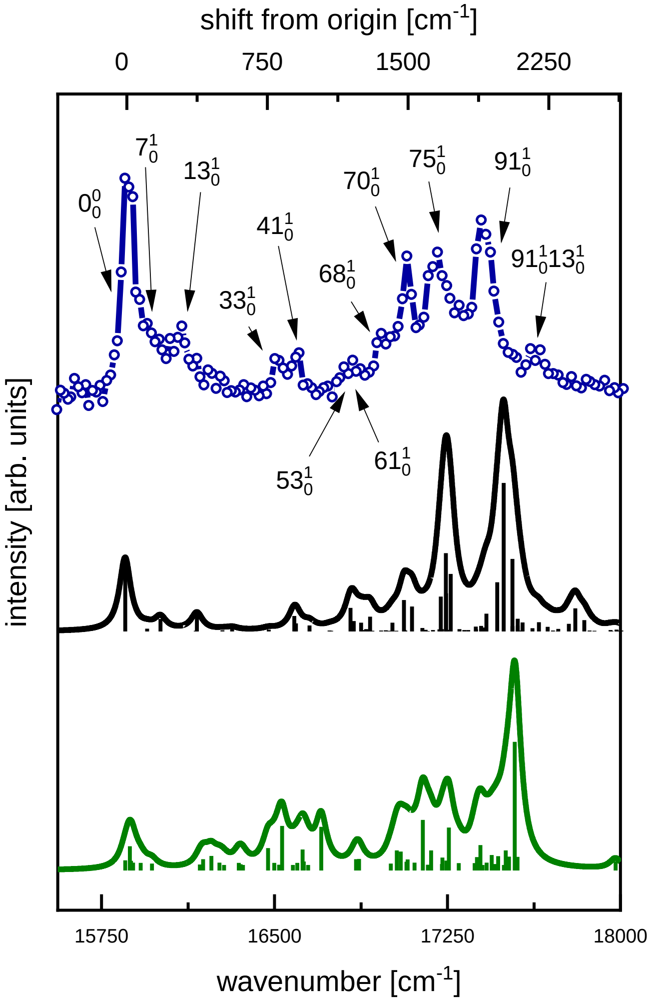

Figure 5.3. The experimental Q_x absorption band of $[(PP–H)\cdot N_2]^-$ (blue) compared with the FCHT simulation of neutral porphine (black) and FCHT simulation (using the vertical gradient approximation) of $(PP\text{-}H)^-$ (green). All calculations (ground and excited state) were done at the CAM-B3LYP/cc-pVDZ level of theory using a scaling factor of 0.97. The open circles in the experimental trace are data points and the full line is a B-spline to guide the eye. The assignments are based on the porphine simulation. The simulations have been shifted to align with the experimental band origin.

As stated above, the Q_x band origin of $[(PP–H)\cdot N_2]^-$ is at 15868 ± 10 cm^{-1} and is followed by a vibronic progression that extends until *ca*. 18000 cm^{-1}. In the remainder of this chapter, we denote transitions, as in Chapter 3, by $Q^{\nu'}_{\nu''}$, where Q is the label of the vibrational mode numbered in order of increasing vibrational frequency in the S_1 state, and ν” and ν’ are the numbers of quanta in mode Q of the ground and S_1 electronic states, respectively. For clarity, experimental frequencies are reported in terms of their offset from the band origin, not as absolute values. The band origin is accompanied by a shoulder at 77 cm^{-1} and a partially resolved peak at 227 cm^{-1}. The shoulder is due to the 7_0^1 band, which can be described as a macrocycle deformation mode where elongation along the x-axis is out of phase with elongation along the y-axis. The peak at 227 cm^{-1} is due to the 13_0^1 mode and is the in-phase combinations of these motions.

The next set of peaks we assign are the two partially resolved peaks at 642 cm^{-1} and 722 cm^{-1}, which are the 33_0^1 and 41_0^1 modes, respectively. These modes include deformations of the pyrrole rings coupled with distortions of the macrocycle. This low energy portion of the absorption band exhibits minor spectral congestion, but beyond *ca*. 1000 cm^{-1} from the band origin, significant spectral congestion sets in because of multiple FCHT active states being close in energy resulting in the spectrum failing to return to baseline between features, as was similarly observed in *m*-NP in Chapter 3. The remaining assignments are based on states with the largest FCHT factors, but the weaker transitions are likely present as unresolved shoulders and certainly contribute to the overall band pattern of the experimental spectrum. The 53_0^1 and 61_0^1 modes contribute to two partially resolved features centered on 972 cm^{-1}. Mode 53 is a combination of pyrrole and macrocycle deformations, and mode 61 is an in-plane pyrrole CH wagging mode. The 68_0^1 band, which appears as a shoulder at 1102 cm^{-1}, is a methine CH wagging mode with all four methine bridges contributing. The set of three intense peaks at 1202 cm^{-1}, 1332 cm^{-1}, and 1532 cm^{-1} primarily correspond to the 70_0^1, 75_0^1, and 91_0^1 modes respectively. Mode 70 is predominantly an in-plane NH bending motion with minor contributions from methine CH wagging motions. Mode 75 is a CN stretching motion also coupled with methine CH wagging motions. Mode 91 is a CC stretch involving the bridging carbons combined with NH wagging.

In the case of $(PP\text{-}H)^-$, the excess negative charge is placed *ca*. 4 Å from the rim of the conjugated macrocycle. This produces an electric field strength on the order of 10^9 V/m at the rim of the conjugated system. The Stark effect from an electric field of this magnitude will have an effect on the electronic energy levels of the molecule. Unfortunately, our experiment is limited to ions, so we cannot measure the spectrum of neutral PP to say anything about the shift induced by the first deprotonation event. We can, however, investigate the effect of the second deprotonation event by comparing the results of the singly deprotonated (monoanion) to a doubly deprotonated (dianion) PP. In addition to the change in the overall charge of the molecule, the mono- and dianion must have different structures. In the dianion, the two carboxylate groups will both carry a negative charge and therefore repel each other, while in the monoanion no such repulsion exists, as only one group is deprotonated.

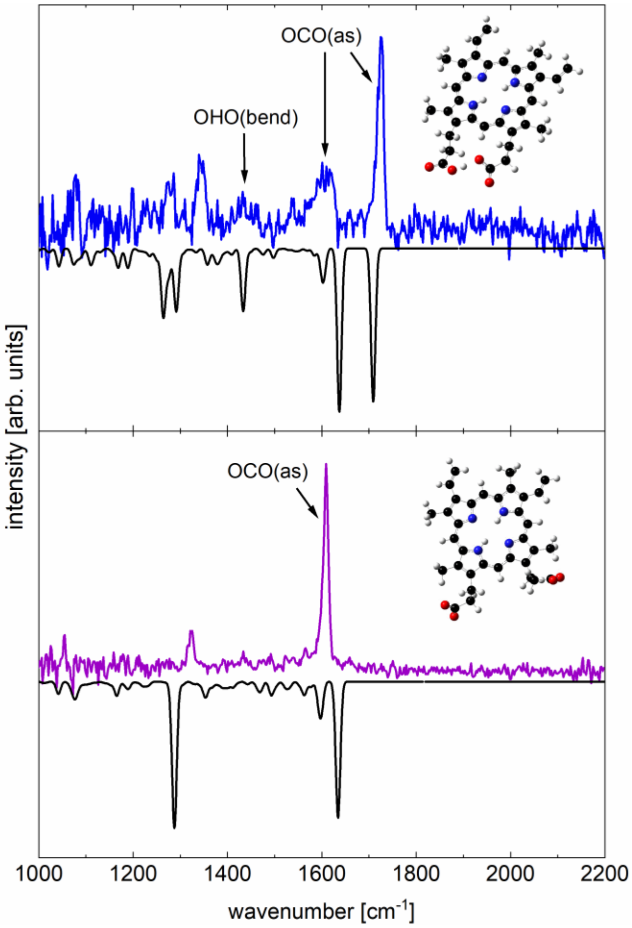

Figure 5.4. IR spectra of $[(PP\text{-}H)\cdot N_2]^-$ (blue) and $[(PP\text{-}2H)\cdot N_2]^{2-}$ (purple) in the fingerprint region from 1000 cm^{-1} to 2200 cm^{-1}. Each trace is accompanied by a simulated spectrum (scaling factor 0.95) for the structure shown.

Figure 5.4 shows the IR spectra of $[(PP\text{-}H)\cdot N_2]^-$ and $[(PP\text{-}2H)\cdot N_2]^{2-}$ in the region from 1000 cm^{-1} to 2200 cm^{-1} and simulated harmonic spectra of the conformers shown. These conformers were the lowest energy structures found in a structural search. The lowest energy monoanion structure has the two carboxylic groups sharing the remaining proton, while in the case of the dianionic structure this proton has been removed and the groups repel each other. Overall, the simulations reproduce the experimental spectra well. For the monoanion, the two peaks at 1726 cm^{-1} and 1617 cm^{-1} represent the antisymmetric OCO stretching vibrations of the two carboxylate groups which are slightly coupled. The peak at 1617 cm^{-1} is accompanied by an unresolved shoulder at *ca*. 1592 cm^{-1} which is due to the two CC stretching vibrations of the ethylene groups. The broad feature at 1430 cm^{-1} is due to the bending motion of the shared carboxylic acid proton. The final two features we assign are at 1280 cm^{-1} and 1245 cm^{-1} which are HCH bending modes localized on the carboxylic acid side chains coupled with the symmetric OCO stretching vibrations.

The purple trace in Figure 5.4 shows the IR spectrum of $[(PP\text{-}2H)\cdot N_2]^{2-}$. The two antisymmetric OCO stretching vibrations observed in the monoanion spectrum have merged into a single feature at 1609 cm^{-1} which, based on the calculation, contains the two unresolved antisymmetric stretching signatures which are of similar intensity and have now been decoupled. The CC stretching vibrations of the ethylene groups are again present as an unresolved shoulder on the low energy side of this peak. The lower two features of the monoanion spectrum, which correspond to HCH bending modes localized on the carboxylic acid side chains coupled with the symmetric OCO stretching vibrations, have similarly collapsed into a single feature at 1324 cm^{-1} in the spectrum of the dianion. The fact that both sets of features, which were both two separate peaks in the monoanion spectrum, now exist as single features, reflects the fact that the two carboxylic acid chains are now nearly completely decoupled. A similar result was reported in work by Johnson and coworkers on singly and doubly deprotonated dodecanedioic acid,[31] where the vibrational signatures of the monoanion species are significantly more complex than those of the dianion, as the carboxylate groups in the monoanion share a proton, and the two groups become fully decoupled in the dianion. The OHO bending signature has vanished from the spectrum of $(PP\text{-}2H)^{-2}$, and this is to be expected as the final carboxylic acid proton is no longer present. The structure shown for the dianion is the lowest energy isomer of four which produce identical IR spectra. These conformers consist of different combinations of orientations of the carboxylate tails being either above or below the plane defined by the macrocycle. All of the conformers in this set are calculated to lie within 30 meV of the structure shown, which has one carboxylate group (on the left in the figure) below the plane defined by the macrocycle, and the other (on the right on the figure) above that plane. We do not attempt to identify which isomer is present in this experiment as none of our measurements can distinguish between them.

Figure 5.5 shows the IR spectrum in the CH and OH stretching region, 2800 cm^{-1} to 3800 cm^{-1}, of the two protonation states of PP. Both spectra show the anti-symmetric NH stretching vibration as intense features at 3324 cm^{-1} and 3327 cm^{-1} for the mono- and dianion, respectively. The symmetric combination of these motions is present as a subtle feature in the monoanion spectrum at 3368 cm^{-1}, but is too weak to be observed in the dianion spectrum. The features just below 3200 cm^{-1} are CH stretching vibrations as well as Fermi-resonances of these modes with overtones and combination bands of lower frequency modes. There is no evidence of a free OH stretching vibration in the spectrum of the monoanion (or the dianion), conforming the prior assertion that the hydrogen is shared between the two carboxylate groups (or in the case of the dianion, no longer present).

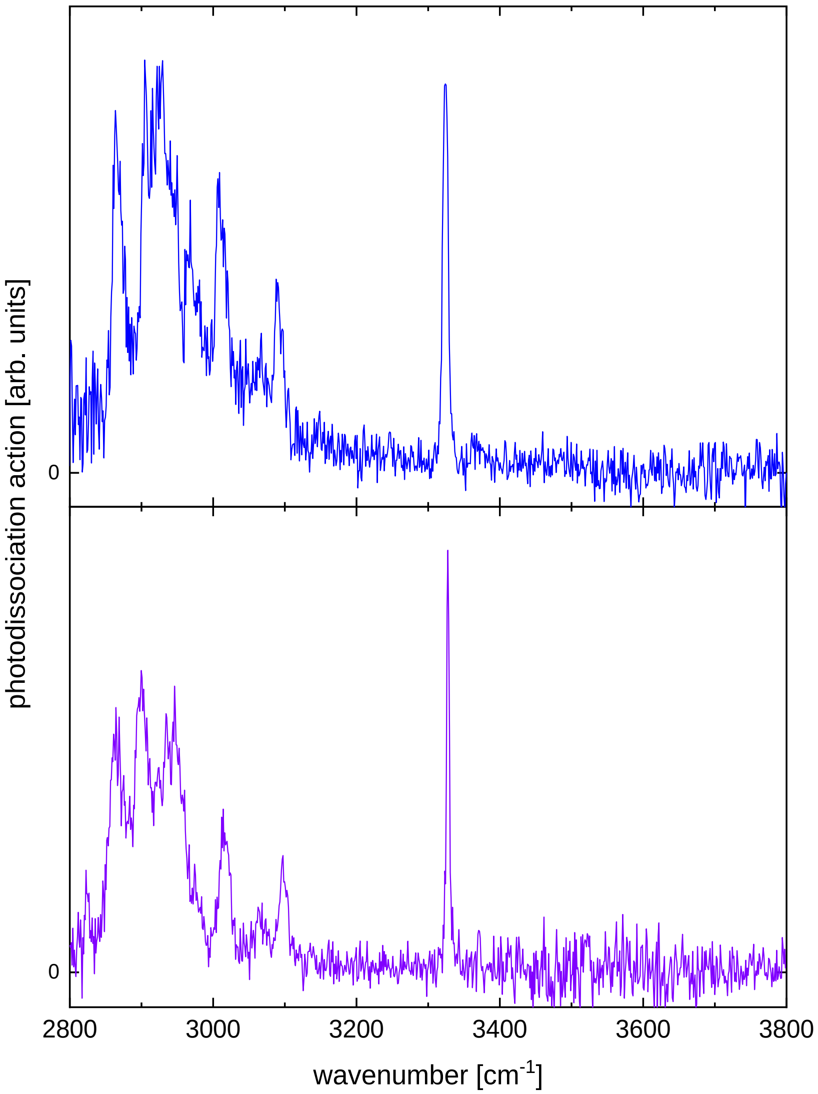

Figure 5.5. IR spectra of $[(PP\text{-}H)\cdot N_2]^-$ (top panel) and of $[(PP\text{-}2H)\cdot N_2]^{2-}$ (bottom) in the CH and OH stretching region.

The IR spectra inform on the molecular structure of PP when moving from a singly to doubly deprotonated species. To investigate the effect on the electronic structure we look at the electronic spectrum. Figure 5.6 shows the Q band region for the two species. The local electric field created by the charged side chains on the macrocycle most likely plays the main role in the observed band shifts through the Stark effect. The band structures of the two spectra are qualitatively very similar, with only slight changes in the splitting of the Q_x and Q_y bands and in the relative intensities of a few features in their vibronic progressions. The similarity of the vibronic progressions is not surprising, because the structure of the macrocycle has not changed substantially and, as we saw in the discussion of the FCHT simulation of the monoanion, the macrocycle largely determines the vibronic structure in PP. There is literature on neutral PP in the gas phase[18] but their data have relatively large error bars compared to our results. Comparing this data on the neutral to our data on the monoanion suggest that the Q_x band shifts very little to the red upon loss of a single proton, while the Q_y band shifts by *ca*. -300 cm^{-1}, reducing the $Q_x – Q_y$ splitting (see Table 5.1). In our experiment, the Q_x band in the dianion is shifted by -110 cm^{-1} relative to the monoanion, while the Q_y band shifts by -490 cm^{-1}. This again reduces the splitting between the Q_x and Q_y bands. Also of note, the onset of the Soret band at 22000 cm^{-1} is now more clearly visible in the spectrum of the dianion, suggesting that it too has shifted to lower wavenumbers.

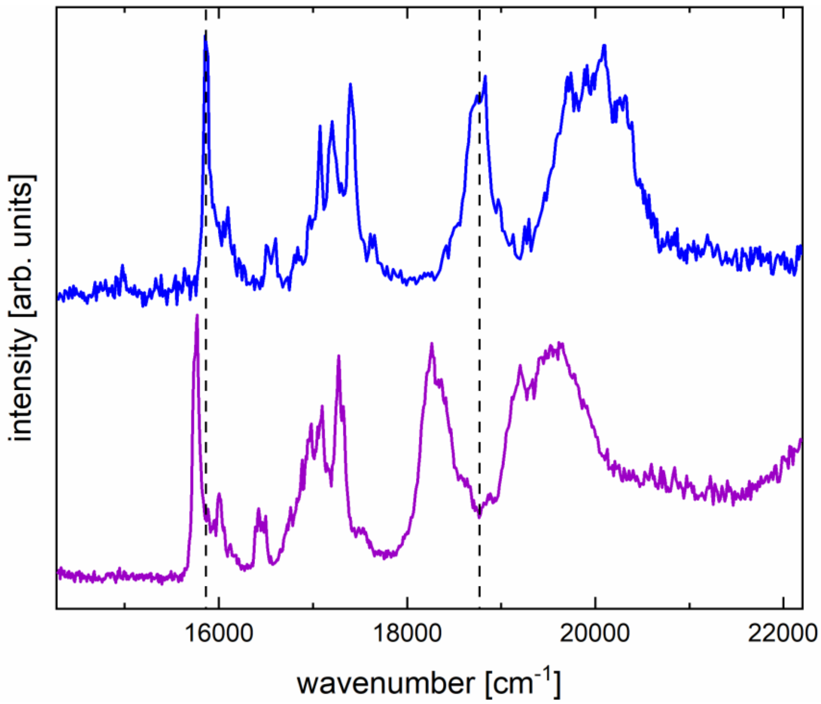

Figure 5.6. Electronic spectrum of $[(PP\text{-}H)\cdot N_2]^-$ (blue) and $[(PP\text{-}2H)\cdot N_2]^{2-}$ (purple) in the Q band region. Dashed vertical lines mark the positions of the Q_x and Q_y band origins of the singly deprotonated species to emphasize the differences.

Table 5.1 shows a comparison of experimental and calculated vertical transitions energies. As can be seen in the table, the TDDFT calculations generally overestimate the Q_x band origin energy while underestimating the Q_y band origin energy. This results in a $Q_x - Q_y$ splitting which is roughly half the experimentally observed value. The results of the TDDFT calculations are questionable, however, because for the dianion they contain charge transfer contributions from the carboxylate groups to the macrocycle even though both functionals used here are range-corrected. The NEVPT2 calculations on the other hand generally underestimate both Q_x and Q_y band origins but produce a better $Q_x - Q_y$ splitting for all charge states. The active space for these calculations consists of orbitals localized on the macrocycle and transitions involving the carboxylate groups are therefore excluded by design.

Table 5.1. Calculated and experimental vertical transition energies for PP and porphine in various charge states expressed in cm^{-1}.

Species	Charge State	Method(a)	$E(Q_x)$(b)	$E(Q_y)$(b)	ΔE(c)
porphine	0	CAM-B3LYP	17500	19321	1821
	0	ωB97XD	17029	18926	1897
PP	0	experiment(d)	15900 ±100	19050 ±100	3150 ± 141
	0	CAM-B3LYP	17312	18738	1426
	0	NEVPT2	15810	18606	2796
	-1	experiment(e)	15870 ± 10	18760 ± 30	2890 ± 32
	-1	CAM-B3LYP	16923	18426	1503
	-1	ωB97XD	16518	18095	1577
	-1	NEVPT2	15377	18217	2840
	-2	experiment(e)	15760 ±10 (-110)	18270 ±30 (-490)	2510 ±32
	-2	CAM-B3LYP	16970 (+452)	18240 (-186)	1270
	-2	ωB97XD	16660 (+142)	18048 (-47)	1388
	-2	NEVPT2	15472 (+95)	18123 (-94)	2651

(a) See Methods section for basis sets.

(b) Numbers in parentheses represent the shift of bands in the dianion from the position of each band in the monoanion.

(c) ΔE refers to the Q_x-Q_y splitting: $\Delta E = E(Q_y) - E(Q_x)$.

(d) Supersonic jet experiment, from ref [18].

(e) FC simulations establish the vertical transition energies at the band origin.

While the NEVPT2 calculations recover the band positions and splittings quite well, they are unable to reproduce the more subtle changes that occur upon further deprotonation. They predict a red shift for the Q_x band going from the neutral to the singly deprotonated monoanion and yield a blue shift as PP is deprotonated a second time rather than another red shift. The calculated $Q_x – Q_y$ splitting first becomes wider (from neutral to -1 overall charge), then narrows again (from -1 to -2 overall charge) while the experimental data suggests it narrows both times. The comparison of these calculations with our experimental results highlight the difficulties that molecules such as PP present even when treated at a high computational level, and shows how cryogenic ion spectroscopy serves as a benchmark for increasingly sophisticated theory.

In many situations, such as the nitrophenolates of Chapter 3 or HBDI in Chapter 4, cryogenic ion spectroscopy *in vacuo* provides the opportunity to determine absolute solvatochromic shifts. In aqueous solution, PP forms pH dependent aggregates due to its amphiphilic character as noted in the introduction, and monomers of PP are only present at low pH (< 3). Examining pK_a values of similar molecules[32] suggests that PP should be neutral in this range, not ionic, and so a direct comparison to our results should not be made. As a result, shifts of electronic absorptions observed upon bringing PP into a solvent can be the result of many effects: (i) solvatochromic effects due to differential solvation of charge distributions; (ii) aggregation effects; (iii) charge screening effects that affect the impact of the intramolecular electric field coming from the deprotonated carboxylic acid groups. These effects are not easily disentangled, and we therefore do not provide a more detailed discussion in this context, but provide a comparison of the current data with literation data on solutions of PP in Table 5.2.

Table 5.2. Solvatochromic data for PP (transition energies in cm^{-1})

Solvent / Temperature	pH (charge)	$Q_x(0)^{(a)}$	$Q_x(1)^{(a)}$	$Q_y(0)^{(a)}$	$Q_y(1)^{(a)}$	ref.
in vacuo / jet	(0)	15900 ±100	17420 ±100	19050 ±100	20410 ±100	17
in vacuo / 60	(-1)	15870 ± 10	17400 ±10	18760 ± 30	20090 ±20	This work
in vacuo / RT	(-1)	N/A	17210 ±100	18690 ±100	20040 ±100	16
in vacuo / 60	(-2)	15760 ±10	17280 ±10	18270 ±30	19630 ±30	This work
water / RT	1	15870	16670	18050	19380	15
water / RT	5	15530	16840	17670	18730	15
water / RT	12	15970	17300	18350	19610	15
DMSO / RT	N/A	15870	17330	18450	19760	15

(a) $Q_x(0)$ and $Q_y(0)$ refer to the maximum of each envelope in the band origin region, while $Q_x(1)$ and $Q_y(1)$ represent the maxima of the envelope in the region of Franck-Condon active modes, ca. 1000 cm^{-1} above each band origin.

5.4 References

1. Zagorec-Marks, W.; Smith, J. E. T.; Foreman, M. M.; Sharma, S.; Weber, J. M., Intrinsic electronic spectra of cryogenically prepared protoporphyrin IX ions in vacuo – deprotonation-induced Stark shifts. *Physical Chemistry Chemical Physics* **2020,** *22* (36), 20295-20302.
2. Carlsen, C. U.; Møller, J. K. S.; Skibsted, L. H., Heme-iron in lipid oxidation. *Coordination Chemistry Reviews* **2005,** *249* (3-4), 485-498.
3. Mamedov, V. A.; Kalinin, A. A., Chapter Two - Quinoxaline Macrocycles. In *Advances in Heterocyclic Chemistry*, Katritzky, A. R., Ed. Academic Press: 2014; Vol. 112, pp 51-115.
4. Kang, S. H.; Jeong, M. J.; Eom, Y. K.; Choi, I. T.; Kwon, S. M.; Yoo, Y.; Kim, J.; Kwon, J.; Park, J. H.; Kim, H. K., Porphyrin Sensitizers with Donor Structural Engineering for Superior Performance Dye-Sensitized Solar Cells and Tandem Solar Cells for Water Splitting Applications. *Advanced Energy Materials* **2017,** *7* (7), 1602117.
5. Yella., A.; Lee., H.-W.; Tsao., H. N.; Yi., C.; Chandiran., A. K.; Nazeeruddin., M. K.; Diau., E. W.-G.; Yeh., C.-Y.; Zakeeruddin., S. M.; Gratzel., M., Porphyrin-Sensitized Solar Cells with Cobalt (II/III)-Based Redox Electrolyte Exceed 12 Percent Efficiency. *Science* **2011,** *334* (6056), 629-634.
6. Lin., S.; Diercks., C. S.; Zhang., Y.-B.; Kornienko., N.; Nichols., E. M.; Zhao., Y.; Paris., A. R.; Kim., D.; Yang., P.; Yaghi., O. M.; Chang., C. J., Covalent organic frameworks comprising cobalt porphyrins for catalytic CO_2 reduction in water. *Science* **2015,** *349* (6253), 1208-1213.

7. Costentin., C.; Drouet., S.; Robert., M.; Saveant., J.-M., A Local Proton Source Enhances CO_2 Electroreduction to CO by a Molecular Fe Catalyst. *Science* **2012,** *338* (6103), 90-94.

8. Tessore, F.; Biroli, A. O.; Di Carlo, G.; Pizzotti, M., Porphyrins for Second Order Nonlinear Optics (NLO): An Intriguing History. *Inorganics* **2018,** *6* (3), 81.

9. Gouterman, M., 1 - Optical Spectra and Electronic Structure of Porphyrins and Related Rings. In *The Porphyrins*, Dolphin, D., Ed. Academic Press: 1978; pp 1-165.

10. Gouterman, M., Spectra of Porphyrins. *Journal of Molecular Spectroscopy* **1961,** *6*, 138-163.

11. Lopes, J. M. S.; Sharma, K.; Sampaio, R. N.; Batista, A. A.; Ito, A. S.; Machado, A. E. H.; Araujo, P. T.; Barbosa Neto, N. M., Novel insights on the vibronic transitions in free base meso-tetrapyridyl porphyrin. *Spectrochim Acta A Mol Biomol Spectrosc* **2019,** *209*, 274-279.

12. Santoro, F.; Lami, A.; Improta, R.; Bloino, J.; Barone, V., Effective method for the computation of optical spectra of large molecules at finite temperature including the Duschinsky and Herzberg-Teller effect: the Q_x band of porphyrin as a case study. *J Chem Phys* **2008,** *128* (22), 224311.

13. Radziszewski, J. G.; Waluk, J.; Nepras, M.; Michl, J., Fourier transform fluorescence and phosphorescence of porphine in rare gas matrixes. *The Journal of Physical Chemistry* **1991,** *95* (5), 1963-1969.

14. Rimington., C.; Mason., S. F.; Kennard, O., Porphin. *Spectrochimiea Acta* **1957,** *12*, 65-77.

15. O. N. Korotaev, R. I. P., Reversible Transformations of Luminescent Impurity Centers in an N-Paraffin Matrix Under Laser Irradiation. *Optics and Spectroscopy* **1971,** *32* (5), 479-480.

16. Scolaro., L. M.; Castriciano., M.; Romeo., A.; Patane., S.; Cefali., E.; Allegrini., M., Aggregation Behavior of Protoporphyrin IX in Aqueous Solutions: Clear Evidence of Vesicle Formation. *J. Phys. Chem. B* **2002,** (106), 2453-2459.

17. Wyer, J. A.; Jensen, C. S.; Brøndsted Nielsen, S., Gas-phase action spectroscopy of protoporphyrin IX (PP) and zinc-PP anions from 210nm to 720nm. *International Journal of Mass Spectrometry* **2011,** *308* (1), 126-132.

18. Beames, J. M.; Vaden, T. D.; Hudson, A. J., The spectroscopy of jet-cooled porphyrins: an insight into the vibronic structure of the Q band. *Journal of Porphyrins and Phthalocyanines* **2012,** *14* (04), 314-323.

19. Baiardi, A.; Bloino, J.; Barone, V., General Time Dependent Approach to Vibronic Spectroscopy Including Franck–Condon, Herzberg–Teller, and Duschinsky Effects. *Journal of Chemical Theory and Computation* **2013,** *9* (9), 4097-4115.

20. Sayfutyarova, E. R.; Hammes-Schiffer, S., Constructing Molecular pi-Orbital Active Spaces for Multireference Calculations of Conjugated Systems. *J Chem Theory Comput* **2019,** *15* (3), 1679-1689.

21. Falahati, K.; Hamerla, C.; Huix-Rotllant, M.; Burghardt, I., Ultrafast photochemistry of free-base porphyrin: a theoretical investigation of B --> Q internal conversion mediated by dark states. *Phys Chem Chem Phys* **2018,** *20* (18), 12483-12492.

22. Angeli, C.; Pastore, M.; Cimiraglia, R., New perspectives in multireference perturbation theory: the n-electron valence state approach. *Theoretical Chemistry Accounts* **2007,** *117* (5), 743-754.

23. Grimme, S.; Antony, J.; Ehrlich, S.; Krieg, H., A consistent and accurate ab initio parametrization of density functional dispersion correction (DFT-D) for the 94 elements H-Pu. *J Chem Phys* **2010,** *132* (15), 154104.

24. Angeli, C.; Cimiraglia, R.; Malrieu, J.-P., n-electron valence state perturbation theory: A spinless formulation and an efficient implementation of the strongly contracted and of the partially contracted variants. *The Journal of Chemical Physics* **2002,** *117* (20), 9138-9153.

25. Angelo., C.; Cimiraglia., R.; Malrieu., J.-P., N-electron valence state perturbation theory: a fast implementation of the strongly contracted variant. *Chemical Physics Letters* **2001,** *350* (3-4), 297-305.

26. Sun, Q.; Zhang, X.; Banerjee, S.; Bao, P.; Barbry, M.; Blunt, N. S.; Bogdanov, N. A.; Booth, G. H.; Chen, J.; Cui, Z.-H.; Eriksen, J. J.; Gao, Y.; Guo, S.; Hermann, J.; Hermes, M. R.; Koh, K.; Koval, P.; Lehtola, S.; Li, Z.; Liu, J.; Mardirossian, N.; McClain, J. D.; Motta, M.; Mussard, B.; Pham, H. Q.; Pulkin, A.; Purwanto, W.; Robinson, P. J.; Ronca, E.; Sayfutyarova, E.; Scheurer, M.; Schurkus, H. F.; Smith, J. E. T.; Sun, C.; Sun, S.-N.; Upadhyay, S.; Wagner, L. K.; Wang, X.; White, A.; Whitfield, J. D.; Williamson, M. J.; Wouters, S.; Yang, J.; Yu, J. M.; Zhu, T.; Berkelbach, T. C.; Sharma, S.; Sokolov, A.; Chan, G. K.-L., Recent developments in the PySCF program package. *Chemical Physics* **2020,** *arXiv:2002. 12531*.

27. Sun., Q.; Timothy C. Berkelbach; Nick S. Blunt; George H. Booth; Sheng Guo; Zhendong Li; Junzi Liu; James D. McClain; Elvira R. Sayfutyarova; Sandeep Sharma; Sebastian

Wouters; Chan, G. K.-L., PySCF: the Python-based simulations of chemistry framework. *WIREs Comput Mol Sci* **2018**, 1340.

28. Sun, Q.; Yang, J.; Chan, G. K.-L., A general second order complete active space self-consistent-field solver for large-scale systems. *Chemical Physics Letters* **2017,** *683*, 291-299.

29. Neese, F., Software update: the ORCA program system, version 4.0. *WIREs Computational Molecular Science* **2017,** *8* (1), 1327.

30. Neese, F., The ORCA program system. *WIREs Computational Molecular Science* **2011,** *2* (1), 73-78.

31. Kamrath, M. Z.; Relph, R. A.; Guasco, T. L.; Leavitt, C. M.; Johnson, M. A., Vibrational predissociation spectroscopy of the H_2-tagged mono- and dicarboxylate anions of dodecanedioic acid. *International Journal of Mass Spectrometry* **2011,** *300* (2-3), 91-98.

32. Das., D. K.; Medhi., O. K., The role of heme propionate in controlling ht redox potential of heme: Square wave voltammetry of protoporphyrinato IX iron (III) in aqueous surfactant micelles. *Journal of Inorganic Biochemistry* **1998,** *70*, 83-90.

Chapter 6 Biliverdin

6.1 Overview

Fluorescent proteins (FPs) have become widely used for fluorescence labeling in biology and biochemistry where they have been engineered to emit at a variety of wavelengths spanning the visible range. FPs typically incorporate a relatively small molecular fluorophore, which is responsible for the fluorescence. While much of the initial work on FPs has been based on Green Fluorescent Protein and its variants, the strong visible and UV absorptions of biological tissue, its yellow autofluorescence, and the resulting shallow penetration depth for fluorescent probes in the visible spectral range are problematic for many applications in tissue imaging. Efforts have therefore been directed at developing fluorophores that emit in the 650-950 nm (15384 - 10526 cm^{-1}) range, the so-called "first near infrared (NIR) window" of biological tissue, where absorption by common biomolecules is minimal.[1-2] One promising fluorophore for these applications is biliverdin (BV) (see Figure 6.1) whose photophysical properties have been studied for decades.[3-6] Its typical emission wavelengths (700-750 nm)[3, 6-10] are in the first NIR window, but they cover a relatively small portion of the desired wavelength range.

Biliverdin is a breakdown product of heme[11] and is structurally similar to protoporphyrin, which was the subject of Chapter 5. While the tetrapyrrole structure of BV is inherited from its porphine-type precursor, it does not form a macrocycle, resulting in a molecule with large conformational freedom. In aqueous solution, BV exists primarily in a helical conformer,[12] even though other conformers have been found as well,[13-15] and it is likely that the absorption and fluorescence properties of BV will depend on its chemical environment and its conformation. It may be possible to extend the absorption and emission wavelengths of BV further to the red, if its response to chemical environment and conformation is known and can be modeled. To achieve this goal, we need a detailed understanding of the photophysics governing the low-lying electronic excited states of the molecule, in particular its intrinsic properties, without the influence of a chemical environment. Here we present the electronic and infrared (IR) spectra of BV in two different deprotonation states.

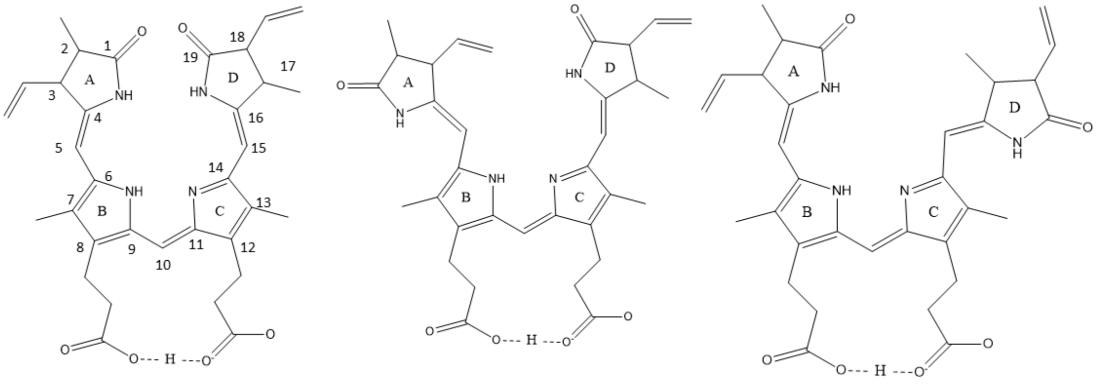

H
ZZZsss

J
ZZZass

K
ZZZssa

Figure 6.1. Examples of conformer families of singly deprotonated biliverdin, [BV-H]$^-$, with the remaining proton shared between the carboxylate groups of the propionic acid tails. Numbering the carbon atoms in the conjugated system as shown in structure H, the abbreviated *Z*/*E* labels refer to the bonds between carbon atoms 4/5, 9/10, and 14/15 in sequence. The abbreviated *syn*/*anti* labels encode the conformations with respect to the bonds between the carbon atoms 5/6, 10/11, and 15/16.

6.2 Computational

Biliverdin has a high degree of conformational flexibility. However, using characteristic signatures in the IR we were able to narrow down the conformational space considered. We generated ca. 15 conformers with the restriction that rings B and C were in a *Zs* configuration and either sharing the remaining proton on the propionic acid tails (in the case of the singly deprotonated monoanion) or allowing these tails to repel each other (in the case of the double deprotonated dianion). A few representative conformers generated in this way are shown in Figure 6.1, differing in the orientation of rings A and D, where the NH groups of the rings can be oriented towards the other rings, or away from them. All conformers were subject to ground state geometry optimizations, harmonic frequency, and vertical excitation calculations at the CAM-B3LYP/cc-pVDZ level of theory.

6.3 Discussion

Rotation around the bonds of the methine bridges between the pyrrole rings allows the existence of many conformers. They can be characterized in terms of the relative orientation of the N atoms on neighboring rings, and the orientation of the apex of the methine bridges between each ring. To describe the structures of different conformers, we will use the notation explained in the caption of Figure 6.1. In porphine and in the helical conformer of BV (Figure 6.1H), which is the dominant structure in solution, all methine bridges have the CH groups on their apex point to the opposite side of the N atoms (or NH groups) of all rings,[13] so both structures are ZZZsss in this notation. In aqueous solutions, BV also exists in a small part of the population as a slightly unfolded conformer, where the bridge between rings C and D is inverted, corresponding to ZZEssa.

For a molecule with the conformational freedom of BV, a key question in the context of the current work is whether the structure in solution is retained *in vacuo*. We use IR spectroscopy in comparison with predicted IR spectra of various conformers to address this question. Different regions of the IR spectrum encode different structural characteristics. Figure 6.2 shows a comparison of the spectra of $[(BV\text{-}H)\cdot N_2]^-$ and the analogous singly deprotonated protoporphyrin

IX complex, $[(PP\text{-}H)\cdot N_2]^-$ (which was discussed in Chapter 5) and a simulated spectrum of conformer J from Figure 6.1 over the range of 1000 cm^{-1} to 2100 cm^{-1}. PP does not have the same conformational freedom as BV because the porphine macrocycle is intact in this molecule, whereas it is open in BV. This region of the IR spectrum of deprotonated PP carries mainly features of the propionic acid tails. The striking similarity between the two IR spectra indicates that these propionic acid tails in $[BV\text{-}H]^-$ and in $[PP\text{-}H]^-$ adopt similar structures, with the intact and the deprotonated carboxylic groups sharing the remaining proton. This is a remarkable structural feature, since the deprotonated carboxylic group could in principle undergo H-bonding to any of the NH groups of the open tetrapyrrole system, if the latter is sufficiently unfolded.

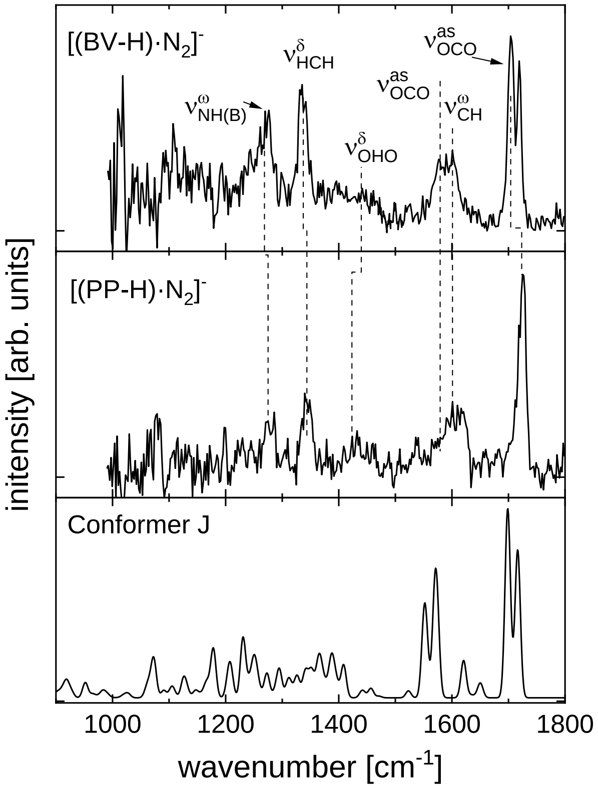

Figure 6.2. Top: IR spectrum of $[(BV\text{-}H)\cdot N_2]^-$, monitoring the loss of N_2. Center: IR spectrum of $[(PP\text{-}H)\cdot N_2]^-$, monitoring the loss of N_2. Bottom: predicted IR spectrum of conformer J (see Figure 1J), with frequencies scaled by 0.9375.

The comparison between BV, PP, and the predicted IR spectra of conformers whose local structure of the B and C rings and the bridge connecting them resembles that of PP, allows us to assign the most prominent peaks in this spectral range. The following spectral assignment is based on the comparison with structure J from Figure 6.1, but we note that this conformer is not the only one which reasonably reproduces the experimental spectrum in this spectral region. We assign the two peaks around 1710 cm^{-1} to CO stretching vibrations. The peak at 1704 cm^{-1} (ν_{OCO}^{s}) contains two overlapping features, one of which is the symmetric combination of the antisymmetric CO stretching vibrations of the carboxylate groups. The other feature is the CO stretch of the carbonyl group on ring D. The higher energy peak at 1719 cm^{-1} (ν_{CO}) contains the carbonyl stretching vibration of the carbonyl group on ring A. The symmetric combination of the carboxylate CO stretching vibrations of the carboxylate group on ring B contributes to the low energy side of the broad feature at 1590 cm^{-1} (ν_{OCO}^{ss}). The high energy side of this feature (ν_{CH}^{ω}) is due to a CC stretch combined with a CH wagging motion of the methine bridge between rings B and C. This feature is only calculated to be intense when it is sterically hindered, which reinforces our assumption of the Zs relationship between the BC rings. The very weak feature at ca. 1530 cm^{-1} (ν_{CC}^{et}) is the signature of the CC stretching vibrations of the ethylene groups on rings A and D. Centered around ca. 1450 cm^{-1} (ν_{OHO}^{δ}) is a broad feature that is due to primarily OHO bending motions of the shared proton. We note that these harmonic frequency calculations predict the OH stretching mode involving this shared proton to be at ca. 2100 cm^{-1}. However, as was the case in the spectrum of the monoanion of PP, this feature is not present in the experimental spectrum because the potential energy landscape for proton motion between the two carboxylate groups is strongly anharmonic and has been found to be significantly red shifted and broadened in similar molecules.[16] The feature at 1337 cm^{-1} (ν_{HCH}^{δ}) is caused by a delocalized combination of HCH bending motions coupled with symmetric CO stretching vibrations of the carboxylate group on ring B. The feature at ca. 1275 cm^{-1} ($\nu_{NH(B)}^{\omega}$) is due to the combination of HCH and NH bending motions of the sp^3 carbons of the propionic acid tails and the NH group of ring B coupled with symmetric CO stretching vibrations of the carboxylate group on ring C.

While the fingerprint region of the IR spectrum, discussed above, informs on the propionic acid tails and the conformation of rings B and C, the orientations of rings A and D have only weak effects on the main features in this region. However, information on the conformation of rings A and D is encoded in the mid-IR region though the NH stretching modes of the pyrrole rings, as the interaction between the NH groups and the lone N atom on ring C changes the IR spectra in characteristic ways. The NH groups on rings A, B, and D can either undergo H-bonding with the N atom on ring C or behave like free (or nearly free) NH oscillators. The NH group of ring B (NH_B) forms a H-bond with the N atom on ring C (N_C) for all structures found in our restricted search. Nearly every structure generated in this restricted structural search reproduce the 1000 – 2000 cm^{-1} region acceptably. Their differences lie predominantly in the 2800 – 3600 cm^{-1} spectral region, which has other complications.

Figure 6.3 shows the 2800 – 3600 cm^{-1} region of the experimental IR spectrum of $[(BV\text{-}H)\cdot N_2]^-$ compared with the computational spectra of several conformers. Four potential NH stretching signatures are observed. A sharp, intense peak at 3444 cm^{-1} (ν_{NH}^{free}) which is the signature of a free NH group. A weaker feature, which appears to be a doublet, at 3405 cm^{-1} and 3391cm^{-1} ($\nu_{NH}^{B/D}$), is characteristic of a NH group participating in a weak hydrogen bond. Finally, a very broad feature that barely rises above the baseline and is centered at *ca*. 3250 cm^{-1} could be representative of a more strongly hydrogen bonded NH group. The fact that there are four potential NH signatures presents several possible explanations: (i) we are looking at a mixture of at least two conformers; (ii) the feature which appears to be a doublet is actually a singlet with an unfortunate dip in the center due purely to the noise level of the spectrum; or (iii) the broad feature at 3250 cm^{-1} is a fluctuation in the baseline that escaped our baseline tracking, not a real signal. Since many scans were averaged on several different days, the latter explanation is very unlikely. A comparison of the experimental spectrum of $[(BV\text{-}H)\cdot N_2]^-$ with $[(PP\text{-}H)\cdot N_2]^-$ reveals that all features below 3150 cm^{-1} are not due to NH stretching vibrations as they appear with remarkable similarity in both the PP and BV spectrum, and all NH stretching vibrations are accounted for in the PP spectrum. As can be seen in Figure 6.3, this spectral region is unable to eliminate any of the presented conformers due to the weak signal intensity of the hydrogen bonded NH stretching vibrations. It is also possible that the red shifts of the hydrogen bonded NH stretching modes are incorrectly predicted in the DFT calculations.

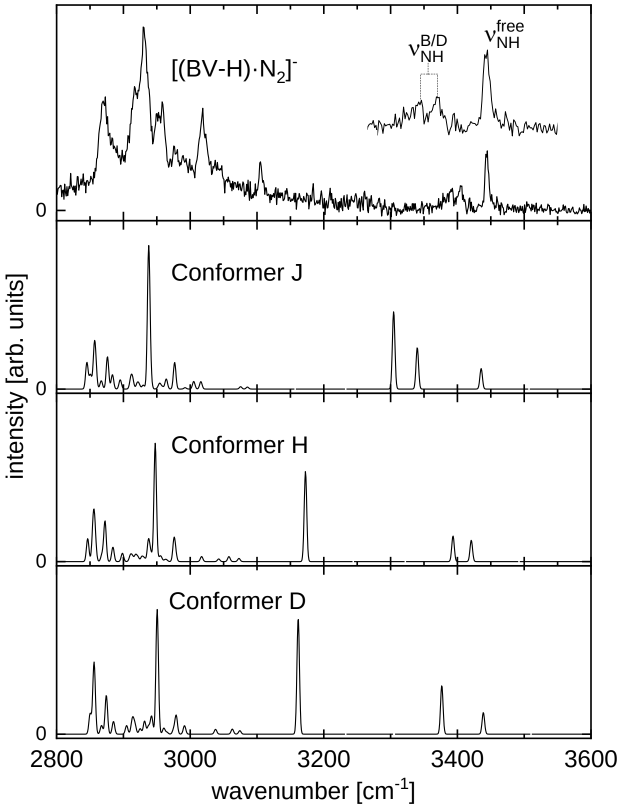

Figure 6.3. IR spectrum of [(BV-H)·N_2]$^-$ in the 2800 – 3600 cm^{-1} spectral region, monitoring the loss of N_2, compared to computational IR spectra of selected conformers from conformer families as shown in Figure 6.1, with frequencies scaled by 0.9392. The insert shows a zoom of the NH stretching region with assignments.

In the lowest energy conformer (structure J from Figure 6.1), the NH group on ring A (NH_A) is pointing away from the others, while the NH group on ring D (NH_D) is pointing toward the N atom on ring C. The distances of NH_B and NH_D to N_C are comparable (2.085 Å and 2.037 Å, respectively), and their NH stretching modes are significantly coupled in symmetric and antisymmetric combinations. Using a scaling factor of 0.9392 for the NH stretching frequencies to align the experimental and calculated free NH features, the antisymmetric and symmetric stretching modes of NH_B and NH_D are calculated at 3313 cm^{-1} and 3348 cm^{-1}, respectively. In the other two conformers presented, this coupling between NH stretching modes is removed. In conformer H, steric repulsion pushes rings A and D away from each other and forces the molecule to adopt a helical structure. This puts the NH groups in separate planes, and we observe two nearly free NH stretching vibrations due to the NH groups on rings A and D, and a hydrogen bonded NH stretching vibration due to the NH group on ring B. The latter can still interact with the nitrogen of ring C. Conformer K is similar to conformer H but instead of the NH group on ring A being turned away from the rest of the molecule, now the NH group on ring D is pointing out instead. In this situation, the NH groups on rings A and B do not couple as strongly as in conformer H, but the NH group of ring A is able to weakly hydrogen bond with the nitrogen on ring C. Out of all calculated IR spectra, the pattern for these conformer families recovers the experimentally observed features best.

We note that we observe an intense peak at 2930 cm^{-1} in the CH stretching region, which is recaptured in all calculated spectra shown in Figure 6.3. This is the signature of the CH stretching mode of the CH group on the methine bridge between rings B and C, which is particularly intense for the Zs geometry governing these two rings and their connecting bridge, corroborating the structural motif we identified for this part of the molecule.

Figure 6.4 shows the electronic spectrum of $[(BV\text{-}H)\cdot N_2]^-$ and the UV-vis spectrum of BV dissolved in water brought to pH 13 with addition of KOH. In the spectrum of $[(BV\text{-}H)\cdot N_2]^-$, we observe a peak at 15000 ± 100 cm^{-1} (ca. 667 nm) with an onset beginning at ca. 14200 cm^{-1}, and a shoulder at 14500 ± 40 cm^{-1}. Additional groups of features appear at higher photon energies, but they are rather broad, despite trap temperatures of 20-35 K. Based on the data shown in Figure 6.4, BV in aqueous solution shows a solvatochromic shift of -220 cm^{-1} compared to singly deprotonated BV *in vacuo*. This solvatochromic shift is not large enough to indicate a significant charge transfer component in the transition. Vertical transition energies to the S_1 states, calculated using TDDFT, for the lowest energy conformers found in our structural search have an average vertical excitation of 18390 cm^{-1}, with all of them falling within *ca*. 1100 cm^{-1} of each other, overestimating the experimental band maximum by 3390 cm^{-1}. The calculated excitation energies for the S_2 states are on average 6900 cm^{-1} higher than the S_1 states indicating that the observed band structure is due to the FC envelope of the S_1 band and could potentially be due to more than one conformer. The narrow range of observed S_1 transition energies shows the weak relation between the conformation of the macrocycle and the excitation energy of the monoanion, but does not provide insight into the conformer(s) responsible.

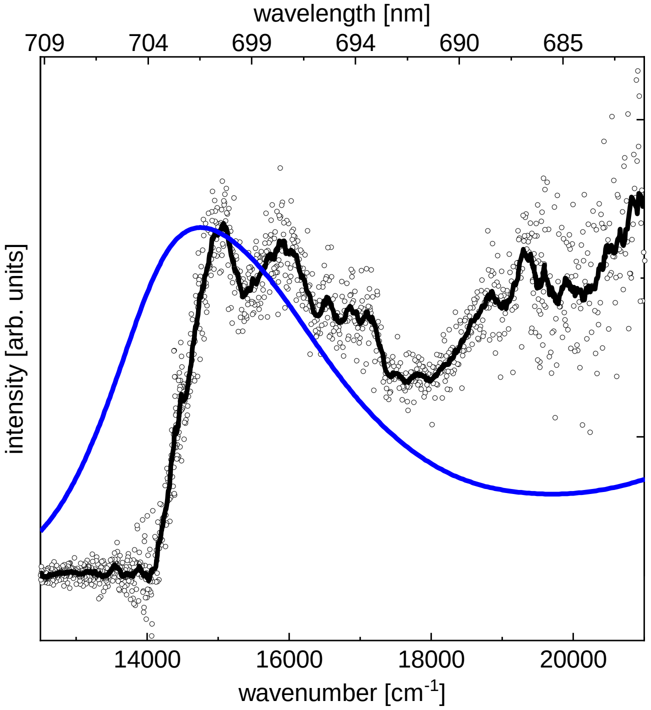

Figure 6.4. Electronic spectrum of $[(BV\text{-}H)\cdot N_2]^-$, monitoring the loss of N_2 (black trace) and the UV-vis spectra of BV dissolved in H_2O at pH 13 (blue trace). The black, open circles are raw data points, the full black line is a 20-point gliding average to guide the eye.

Figure 6.5 contains the experimental IR spectrum of $[(BV\text{-}2H)\cdot N_2]^{-2}$ along with simulated spectra for the same three conformer families presented for the singly deprotonated species from 1000 cm^{-1} to 1800 cm^{-1}. Simply removing the shared hydrogen from the conformers considered previously, and allowing the molecule to relax its geometry from these starting points, results in the conformers used to produce the traces in Figure 6.5. Deprotonating in this location causes the propionic side chains to electrostatically repel each other, and breaks the coupling between their vibrational modes. As discussed for the monoanion spectrum, the carbonyl region informs on the propionic side chains. The following mode assignment is based on conformer K which best matches the experimental spectrum. The peak at 1704 cm^{-1} (ν_{CO}^{D}) is the carbonyl stretching motion of ring D which couples to the NH bend of the same ring. The same motion, but for ring A (ν_{CO}^{A}) shows up as an unresolved shoulder at 1690 cm^{-1}.The mode corresponding to the asymmetric combination of CO stretches on the individual carboxylate groups are now nearly degenerate and appear as the peak at 1650 cm^{-1} (ν_{OCO}^{as}). The third intense feature in the carbonyl region, at 1596 cm^{-1}, is due to the CH wag of the bridge between rings A and B ($\nu_{CH}^{\omega AB}$) . There are several unresolved features centered around 1518 cm^{-1} ($\nu_{CH}^{\omega BC}$) which are due to the CH wag of the bridge between rings B and C coupling with CC stretches of the pyrrole rings. The next feature of the low energy region we assign corresponds to a diffuse mode involving coupled CH wagging motions of all three bridges, and ring deformations of all 4 rings, which is at 1350 cm^{-1} (ν_{CH}^{ω}). The symmetric combination of the CO stretching vibrations of the carboxylate groups are responsible for the feature at 1300 cm^{-1} (ν_{OCO}^{s}). The final feature we assign in this spectral region is the peak at 1250 cm^{-1} which is due to the NH and CH wagging motions from the NH groups on rings A and B and the CH of the BC methine bridge (ν_{NH}^{ω}).

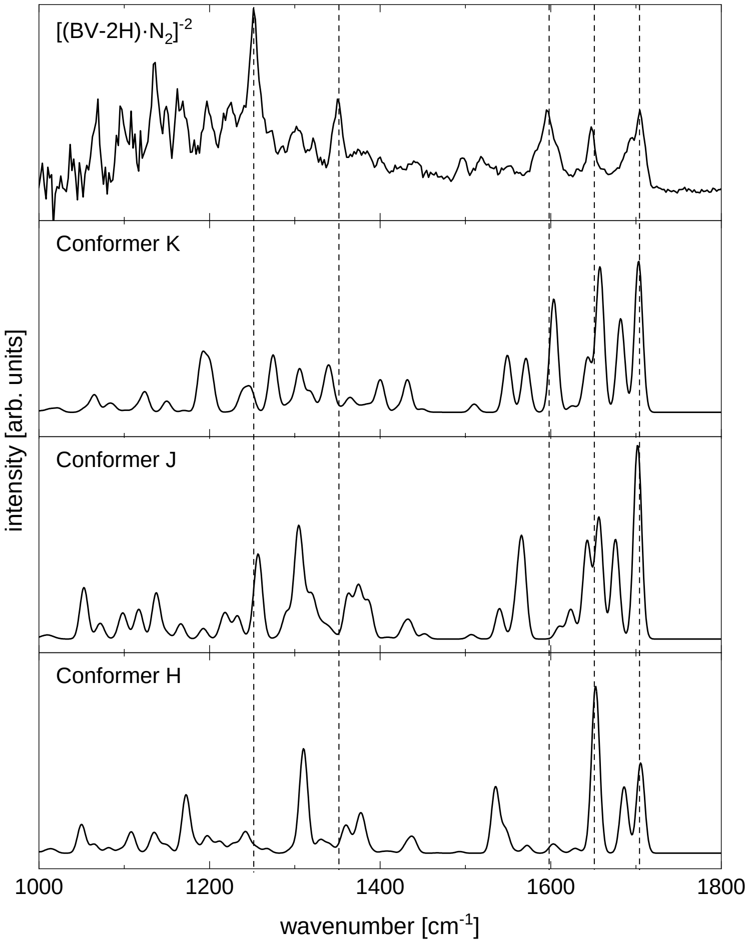

Figure 6.5. Comparison of IR spectra of [(BV-2H)·N$_2$]$^{-2}$ with simulated spectra for three select conformers from 1000-1800 cm^{-1}. The vertical dashed lines indicate the location of prominent features in the experimental spectrum. Simulated spectra have been scaled by 0.9325.

Figure 6.6 contains a comparison of the IR spectra of [(BV-2H)·N$_2$]$^{-2}$ with the same three conformers used in Figure 6.5 in the CH and NH stretching region. In this range, we observe a similar pattern of CH stretches as in the monoanion, with the important note that the CH stretching peak of the methine bridge between the BC rings, at *ca*. 2920 cm^{-1} is now of lower relative intensity. The three highest energy features are likely due to NH stretching vibrations. The peak at 3507 cm^{-1} corresponding to a free NH stretching motion (ν_{NH}^{free}) which is present in all three conformers in the figure. The remaining two features, at 3345 cm^{-1} and 3155 cm^{-1} correspond to hydrogen bonded NH stretching vibrations. As can be seen in the figure, none of these simulations reproduce the pattern of the NH stretching modes. This is not entirely surprising as these are harmonic frequency calculations, and hydrogen bonded modes can be significantly anharmonic.[17]

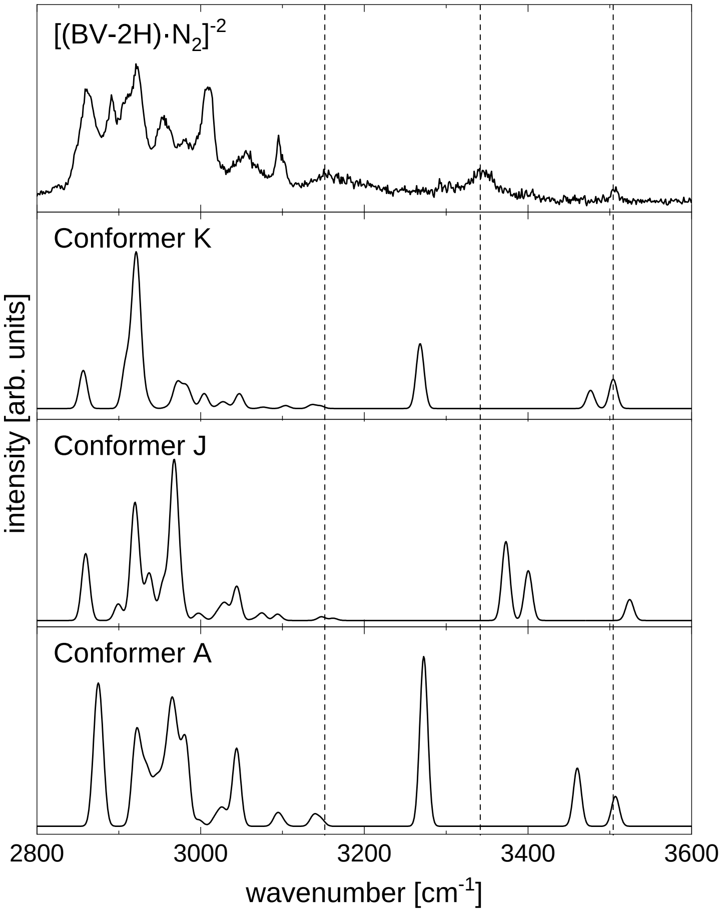

Figure 6.6. Comparison of IR spectra of $[(BV\text{-}2H)\cdot N_2]^{-2}$ with simulated spectra for three select isomers from 2800-3600 cm^{-1}. The vertical dashed lines indicate the location of prominent features in the experimental spectrum. Simulated spectra have been scaled by 0.96.

The electronic spectrum of $[(BV\text{-}2H)\cdot N_2]^{-2}$ is presented in Figure 6.7. The main absorption feature is red shifted by about 5000 cm^{-1} relative to that of the singly deprotonated species, and the absorption profile has changed qualitatively. The absorption maximum is at 10800 ± 100 cm^{-1} (926 nm), well into the NIR window of biological tissue, indicating that this chromophore can access a larger portion of the range than is currently achieved in proteins. We observe a broad peak at +1650 cm^{-1} above the absorption maximum and a second feature of similar width at +3400 cm^{-1}. For $[(BV\text{-}2H)\cdot N_2]^{-2}$, the calculated (TDDFT) S_1 vertical excitations place the first absorption maximum on average at ca. 16300 cm^{-1}, and they are spread further apart (ca. 3400 cm^{-1}) than for singly deprotonated BV. Conformers K and J are on the low energy end of this spread with calculated S_1 transition energies of 15084 cm^{-1} and 14561 cm^{-1} respectively. Recall from the discussion of the singly deprotonated species, calculations overestimated the experimental spectrum by ca. 3400 cm^{-1}. If we assume a similar offset is present here, the calculated S_1 transitions for both conformer J and K come close to the experimental value. While we can offer no unique structural assignment based on our IR and electronic spectra, we do note that the large observed red-shift between the mono- and dianion is qualitatively recovered by the calculations for the conformational families discussed here. This suggests that subjecting the conjugated system of the chromophore to an electric field is playing a substantial role in the position of the S_1 band in BV. However, because we are unable to provide a unique structural assignment to confirm only small structural changes are occurring between the mono- and dianion, we cannot completely rule out other effects (such as a large conformational change) .

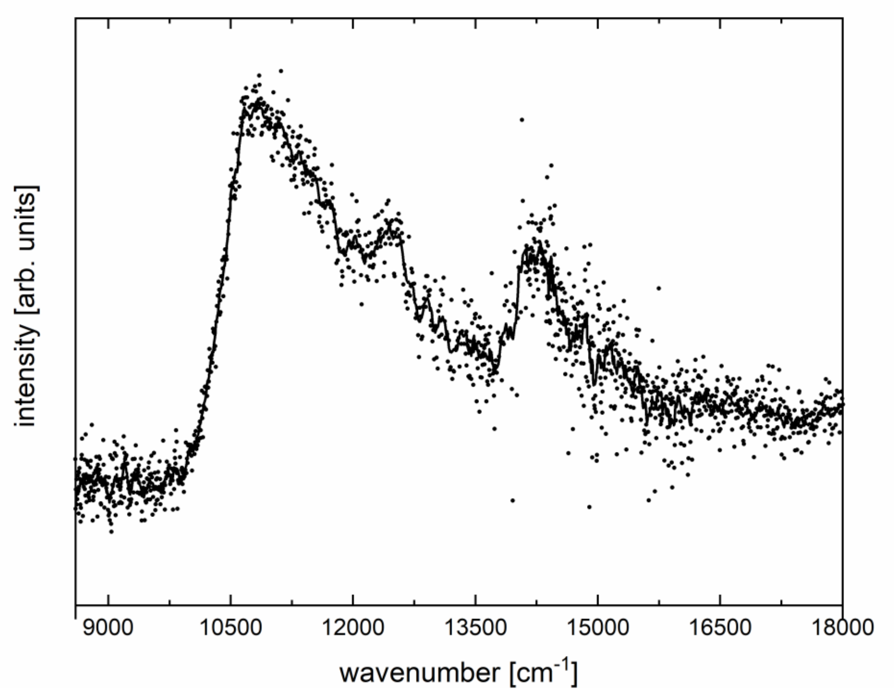

Figure 6.7. Electronic spectrum of $[(BV\text{-}2H)\cdot N_2]^{-2}$. As was the case for $[(BV\text{-}H)\cdot N_2]^-$, the vibronic progression is unresolved despite being taken at a trap temperature of 20 K. The main absorption feature occurs at 10800 cm^{-1} with a shoulder at +1650 cm^{-1} and a third feature at 14200 cm^{-1}.

Despite being taken at pH 13, the UV-vis spectrum of BV in aqueous solution in Figure 6.4 contains no features red of the peak absorption at 14780 cm^{-1}. This indicates that either the dianion species is not present in solution, which is unlikely at this pH,[18] or that it undergoes a substantial solvatochromic shift. Figure 6.8 compares the electronic spectra of $[(BV\text{-}2H)\cdot N_2]^{-2}$ and $[(BV\text{-}2H)\cdot (H_2O)_n]^{-2}$ for n=1-4. Addition of each water molecule shifts the absorption feature blue by ca. 290 cm^{-1}. If this trend were to continue in a linear fashion, one expects ca. 10-12 molecules are required to shift the absorption to where the solution phase absorption occurs. Of course, this trend is not likely to be linear, and this estimate represents a lower bound for the actual number of water molecules required to fully reach the value for aqueous solution. While we did not perform calculations on any hydrated clusters, one would expect the water molecules to solvate the negatively charged carboxylate groups. As the number of water molecules increases, they change the charge distribution of the molecule and therefore the electric field experienced by the conjugated system. As we have already seen, the S_1 excitation energy is sensitive to the electric field and so the shift is not surprising.

At the time of the writing of this thesis, investigations of this molecule are ongoing, aimed at addressing the question of which conformer, or conformers, is (or are) responsible for the observed electronic absorptions. The conformer (and charge distribution) responsible for the absorption spectrum of the dianion is of particular interest as an absorption wavelength of 926 nm would represent a significant increase in the spectral range accessible by this chromophore compared to what has been achieved previously. The hydration experiments suggest that one would be able to tune the absorption band throughout the first NIR window of biological materials. Future experiments will involve using ion mobility[19] to determine how many conformers are present (in both charge states), and hole burning[20] techniques to then determine which spectral features are due to which conformer.

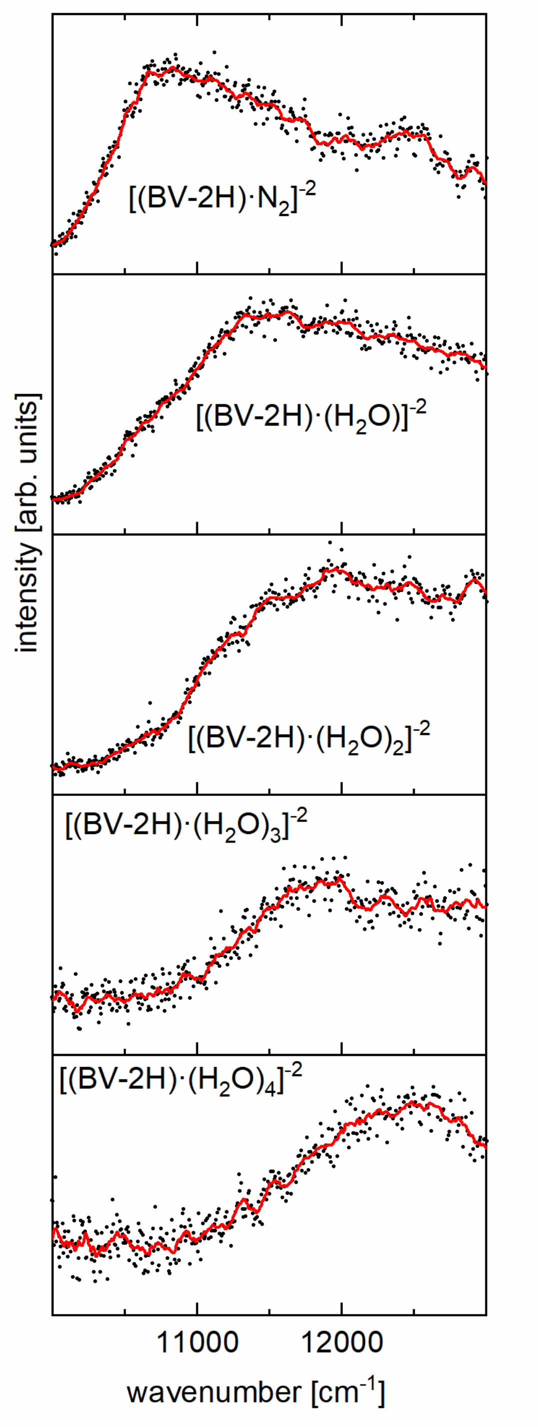

Figure 6.8. Electronic spectrum of the band origin region of [(BV-2H)·N_2]$^{-2}$ (top trace) and [(BV-2H)·(H_2O)$_n$]$^{-2}$ for n=1-4 (lower traces). The black circles are data points, the red lines are 10 point adjacent averages to guide the eye.

6.4 References

1. Frangioni, J. V., In vivo near-infrared fluorescence imaging. *Current Opinion in Chemical Biology* **2003,** *7* (5), 626-634.
2. Weissleder, R., A clearer vision for in vivo imaging. *Nature Biotechnology* **2001,** *19* (4), 316-317.
3. Chernov, K. G.; Redchuk, T. A.; Omelina, E. S.; Verkhusha, V. V., Near-Infrared Fluorescent Proteins, Biosensors, and Optogenetic Tools Engineered from Phytochromes. *Chemical Reviews* **2017,** *117* (9), 6423-6446.
4. Wagner, U. G.; Müller, N.; Schmitzberger, W.; Falk, H.; Kratky, C., Structure Determination of te Biliverdin Apomyoglobin Complex: Crystal Structure Analysis of Two Crystal Forms at 1.4 and 1.5 Å Resolution. *Journal of Molecular Biology* **1995,** *247* (2), 326-337.
5. Zahedi, M.; Ghiasi, M.; Safari, N., Modeling of biliverdin reduction process: regio-specificity and H-bonding. *Chemical Physics* **2005,** *310* (1), 179-187.
6. Montecinos-Franjola, F.; Lin, J. Y.; Rodriguez, E. A., Fluorescent proteins for in vivo imaging, where's the biliverdin? *Biochemical Society Transactions* **2020,** *48* (6), 2657-2667.
7. Tchekanda, E.; Sivanesan, D.; Michnick, S. W., An infrared reporter to detect spatiotemporal dynamics of protein-protein interactions. *Nature Methods* **2014,** *11* (6), 641-644.
8. Fushimi, K.; Nakajima, T.; Aono, Y.; Yamamoto, T.; Ni Ni, W.; Ikeuchi, M.; Sato, M.; Narikawa, R., Photoconversion and Fluorescence Properties of a Red/Green-Type

Cyanobacteriochrome AM1_C0023g2 That Binds Not Only Phycocyanobilin But Also Biliverdin. *Frontiers in Microbiology* **2016,** *7,* 588.

9. Fankhauser, C., The Phytochromes, a Family of Red/Far-red Absorbing Photoreceptors*. *Journal of Biological Chemistry* **2001,** *276* (15), 11453-11456.

10. Braslavsky, S. E.; Holzwarth, A. R.; Lehner, H.; Schaffner, K., The fluorescence of biliverdin dimethyl ester. *Helvetica Chimica Acta* **1978,** *61* (6), 2219-2222.

11. Rockwell, N. C.; Lagarias, J. C., A Brief History of Phytochromes. *ChemPhysChem* **2010,** *11* (6), 1172-1180.

12. Braslavsky, S. E.; Holzwarth, A. R.; Schaffner, K., Solution Conformations, Photophysics, and Photochemistry of Bile Pigments; Bilirubin and Biliverdin, Dimethyl Esters and Related Linear Tetrapyrroles. *Angewandte Chemie International Edition in English* **1983,** *22* (9), 656-674.

13. Frański, R.; Gierczyk, B.; Popenda, Ł.; Kasperkowiak, M.; Pędzinski, T., Identification of a biliverdin geometric isomer by means of HPLC/ESI–MS and NMR spectroscopy. Differentiation of the isomers by using fragmentation “in-source”. *Monatshefte für Chemie - Chemical Monthly* **2018,** *149* (6), 995-1002.

14. Holt, R. E.; Farrens, D. L.; Song, P. S.; Cotton, T. M., Surface-enhanced resonance Raman scattering (SERRS) spectroscopy applied to phytochrome and its model compounds. I. Biliverdin photoisomers. *Journal of the American Chemical Society* **1989,** *111* (26), 9156-9162.

15. Falk, H.; Grubmayr, K.; Haslinger, E.; Schlederer, T.; Thirring, K., Beiträge zur Chemie der Pyrrolpigmente, 25. Mitt. Die diastereomeren (geometrisch isomeren)

Biliverdindimethylester—Struktur, Konfiguration und Konformation. *Monatshefte für Chemie - Chemical Monthly* **1978,** *109* (6), 1451-1473.

16. Kamrath, M. Z.; Relph, R. A.; Guasco, T. L.; Leavitt, C. M.; Johnson, M. A., Vibrational predissociation spectroscopy of the H2-tagged mono- and dicarboxylate anions of dodecanedioic acid. *International Journal of Mass Spectrometry* **2011,** *300* (2), 91-98.

17. Garand, E.; Kamrath, M. Z.; Jordan, P. A.; Wolk, A. B.; Leavitt, C. M.; McCoy, A. B.; Miller, S. J.; Johnson, M. A., Determination of Noncovalent Docking by Infrared Spectroscopy of Cold Gas-Phase Complexes. *Science* **2012,** *335* (6069), 694.

18. Lightner, D. A.; Holmes, D. L.; McDonagh, A. F., On the Acid Dissociation Constants of Bilirubin and Biliverdin: pKa VALUES FROM 13C NMR SPECTROSCOPY (*). *Journal of Biological Chemistry* **1996,** *271* (5), 2397-2405.

19. Woods, L. A.; Radford, S. E.; Ashcroft, A. E., Advances in ion mobility spectrometry–mass spectrometry reveal key insights into amyloid assembly. *Biochimica et Biophysica Acta (BBA) - Proteins and Proteomics* **2013,** *1834* (6), 1257-1268.

20. Leavitt, C. M.; Wolk, A. B.; Fournier, J. A.; Kamrath, M. Z.; Garand, E.; Van Stipdonk, M. J.; Johnson, M. A., Isomer-Specific IR–IR Double Resonance Spectroscopy of D2-Tagged Protonated Dipeptides Prepared in a Cryogenic Ion Trap. *The Journal of Physical Chemistry Letters* **2012,** *3* (9), 1099-1105.

Chapter 7 Bibliography

Almasian, M.; Grzetic, J.; Berden, G.; Bakker, B.; Buma, W. J.; Oomens, J., Gas-phase infrared spectrum of the anionic GFP-chromophore. *International Journal of Mass Spectrometry* **2012,** *330*, 118-123.

Andersen, L. H.; Bluhme, H.; Boye, S.; Jorgensen, T. J. D.; Krogh, H.; Nielsen, I. B.; Nielsen, S. B.; Svendsen, A., Experimental studies of the photophysics of gas-phase fluorescent protein chromophores. *Physical Chemistry Chemical Physics* **2004,** *6* (10), 2617-2627.

Andersen, L. H.; Lapierre, A.; Nielsen, S. B.; Nielsen, I. B.; Pedersen, S. U.; Pedersen, U. V.; Tomita, S., Chromophores of the green fluorescent protein studied in the gas phase. *European Physical Journal D* **2002,** *20* (3), 597-600.

Anderson, J.; Burns, P. J.; Milroy, D.; Ruprecht, P.; Hauser, T.; Siegel, H. J., Deploying RMACC Summit: An HPC Resource for the Rocky Mountain Region. In *Proceedings of the Practice and Experience in Advanced Research Computing 2017 on Sustainability, Success and Impact*, Association for Computing Machinery: New Orleans, LA, USA, 2017; p Article 8.

Angeli, C.; Cimiraglia, R.; Malrieu, J.-P., n-electron valence state perturbation theory: A spinless formulation and an efficient implementation of the strongly contracted and of the partially contracted variants. *The Journal of Chemical Physics* **2002,** *117* (20), 9138-9153.

Angeli, C.; Pastore, M.; Cimiraglia, R., New perspectives in multireference perturbation theory: the n-electron valence state approach. *Theoretical Chemistry Accounts* **2007,** *117* (5), 743-754.

Angelo., C.; Cimiraglia., R.; Malrieu., J.-P., N-electron valence state perturbation theory: a fast implementation of the strongly contracted variant. *Chemical Physics Letters* **2001,** *350* (3-4), 297-305.

Anstöter, C. S.; Bull, J. N.; Verlet, J. R. R., Ultrafast dynamics of temporary anions probed through the prism of photodetachment. *International Reviews in Physical Chemistry* **2016,** *35* (4), 509-538.

Anstöter, C. S.; Dean, C. R.; Verlet, J. R. R., Chromophores of chromophores: a bottom-up Huckel picture of the excited states of photoactive proteins. *Physical Chemistry Chemical Physics* **2017,** *19* (44), 29772-29779.

Asvany, O.; Schlemmer, S., Numerical Simulations of Kinetic Ion Temperature in a Cryogenic Linear Multipole Trap. *International Journal of Mass Spectrometry* **2009,** *279* (2), 147-155.

Baiardi, A.; Bloino, J.; Barone, V., General Time Dependent Approach to Vibronic Spectroscopy Including Franck–Condon, Herzberg–Teller, and Duschinsky Effects. *Journal of Chemical Theory and Computation* **2013,** *9* (9), 4097-4115.

Bakels, S.; Gaigeot, M.-P.; Rijs, A. M., Gas-Phase Infrared Spectroscopy of Neutral Peptides: Insights from the Far-IR and THz Domain. *Chemical Reviews* **2020,** *120* (7), 3233-3260.

Beames, J. M.; Vaden, T. D.; Hudson, A. J., The spectroscopy of jet-cooled porphyrins: an insight into the vibronic structure of the Q band. *Journal of Porphyrins and Phthalocyanines* **2012,** *14* (04), 314-323.

Becke, A. D., Density-Functional Exchange-Energy Approximation with Correct Asymptotic-Behavior. *Phys. Rev. A* **1988,** *38* (6), 3098-3100.

Bochenkova, A. V.; Andersen, L. H., Ultrafast dual photoresponse of isolated biological chromophores: link to the photoinduced mode-specific non-adiabatic dynamics in proteins. *Faraday Discussions* **2013,** *163*, 297-319.

Bochenkova, A. V.; Klaerke, B.; Rahbek, D. B.; Rajput, J.; Toker, Y.; Andersen, L. H., UV Excited-State Photoresponse of Biochromophore Negative Ions. *Angewandte Chemie-International Edition* **2014,** *53* (37), 9797-9801.

Bochenkova, A. V.; Mooney, C. R. S.; Parkes, M. A.; Woodhouse, J. L.; Zhang, L. J.; Lewin, R.; Ward, J. M.; Hailes, H. C.; Andersen, L. H.; Fielding, H. H., Mechanism of resonant electron emission from the deprotonated GFP chromophore and its biomimetics. *Chemical Science* **2017,** *8* (4), 3154-3163.

Borgstahl, G. E. O.; Williams, D. R.; Getzoff, E. D., 1.4 Å Structure of Photoactive Yellow Protein, a Cytosolic Photoreceptor: Unusual Fold, Active Site, and Chromophore. *Biochemistry* **1995,** *34* (19), 6278-6287.

Braslavsky, S. E.; Holzwarth, A. R.; Lehner, H.; Schaffner, K., The fluorescence of biliverdin dimethyl ester. *Helvetica Chimica Acta* **1978,** *61* (6), 2219-2222.

Braslavsky, S. E.; Holzwarth, A. R.; Schaffner, K., Solution Conformations, Photophysics, and Photochemistry of Bile Pigments; Bilirubin and Biliverdin, Dimethyl Esters and Related Linear Tetrapyrroles. *Angewandte Chemie International Edition in English* **1983,** *22* (9), 656-674.

Brøndsted Nielsen, S.; Brøndsted Nielsen, M.; Rubio, A., Spectroscopy of Nitrophenolates in Vacuo: Effect of Spacer, Configuration, and Microsolvation on the Charge-Transfer Excitation Energy. *Accounts of Chemical Research* **2014,** *47* (4), 1417-1425.

Bublitz, G.; King, B. A.; Boxer, S. G., Electronic structure of the chromophore in green fluorescent protein (GFP). *Journal of the American Chemical Society* **1998,** *120* (36), 9370-9371.

Bureš, F., Fundamental Aspects of Property Tuning in Push–Pull Molecules. *RSC Advances* **2014,** *4* (102), 58826-58851.

Carlsen, C. U.; Møller, J. K. S.; Skibsted, L. H., Heme-iron in lipid oxidation. *Coordination Chemistry Reviews* **2005,** *249* (3-4), 485-498.

Carrascosa, E.; Bull, J. N.; Scholz, M. S.; Coughlan, N. J. A.; Olsen, S.; Wille, U.; Bieske, E. J., Reversible Photoisomerization of the Isolated Green Fluorescent Protein Chromophore. *Journal of Physical Chemistry Letters* **2018,** *9* (10), 2647-2651.

Chai, J.-D.; Head-Gordon, M., Long-range corrected hybrid density functionals with damped atom–atom dispersion corrections. *Physical Chemistry Chemical Physics* **2008,** *10* (44), 6615-6620.

Chalfie, M.; Tu, Y.; Euskirchen, G.; Ward, W. W.; Prasher, D. C., Green Fluorescent Protein as a Marker for Gene-Expression. *Science* **1994,** *263* (5148), 802-805.

Chattoraj, M.; King, B. A.; Bublitz, G. U.; Boxer, S. G., Ultra-fast excited state dynamics in green fluorescent protein: Multiple states and proton transfer. *Proceedings of the National Academy of Sciences of the United States of America* **1996,** *93* (16), 8362-8367.

Chernov, K. G.; Redchuk, T. A.; Omelina, E. S.; Verkhusha, V. V., Near-Infrared Fluorescent Proteins, Biosensors, and Optogenetic Tools Engineered from Phytochromes. *Chemical Reviews* **2017,** *117* (9), 6423-6446.

Chingin, K.; Balabin, R. M.; Frankevich, V.; Barylyuk, K.; Nieckarz, R.; Sagulenko, P.; Zenobi, R., Absorption of the green fluorescent protein chromophore anion in the gas phase studied by a combination of FTICR mass spectrometry with laser-induced photodissociation spectroscopy. *International Journal of Mass Spectrometry* **2011,** *306* (2-3), 241-245.

Chudakov, D. M.; Matz, M. V.; Lukyanov, S.; Lukyanov, K. A., Fluorescent Proteins and Their Applications in Imaging Living Cells and Tissues. *Physiological Reviews* **2010,** *90* (3), 1103-1163.

Costentin., C.; Drouet., S.; Robert., M.; Saveant., J.-M., A Local Proton Source Enhances CO_2 Electroreduction to CO by a Molecular Fe Catalyst. *Science* **2012,** *338* (6103), 90-94.

Das., D. K.; Medhi., O. K., The role of heme propionate in controlling ht redox potential of heme: Square wave voltammetry of protoporphyrinato IX iron (III) in aqueous surfactant micelles. *Journal of Inorganic Biochemistry* **1998,** *70*, 83-90.

Day, R. N.; Davidson, M. W., The fluorescent protein palette: tools for cellular imaging. *Chem. Soc. Rev.* **2009,** *38* (10), 2887-2921.

Deng, S. H. M.; Kong, X. Y.; Zhang, G. X.; Yang, Y.; Zheng, W. J.; Sun, Z. R.; Zhang, D. Q.; Wang, X. B., Vibrationally Resolved Photoelectron Spectroscopy of the Model GFP

Chromophore Anion Revealing the Photoexcited S-1 State Being Both Vertically and Adiabatically Bound against the Photodetached D-0 Continuum. *Journal of Physical Chemistry Letters* **2014,** *5* (12), 2155-2159.

Dodson, L. G.; Zagorec-Marks, W.; Xu, S.; Smith, J. E. T.; Weber, J. M., Intrinsic photophysics of nitrophenolate ions studied by cryogenic ion spectroscopy. *Physical Chemistry Chemical Physics* **2018,** *20* (45), 28535-28543.

Elliott, B. M.; Relph, R. A.; Roscioli, J. R.; Bopp, J. C.; Gardenier, G. H.; Guasco, T. L.; Johnson, M. A., Isolating the spectra of cluster ion isomers using Ar-"tag" -mediated IR-IR double resonance within the vibrational manifolds: Application to NO2-center dot H2O. *Journal of Chemical Physics* **2008,** *129* (9).

Falahati, K.; Hamerla, C.; Huix-Rotllant, M.; Burghardt, I., Ultrafast photochemistry of free-base porphyrin: a theoretical investigation of B --> Q internal conversion mediated by dark states. *Phys Chem Chem Phys* **2018,** *20* (18), 12483-12492.

Falk, H.; Grubmayr, K.; Haslinger, E.; Schlederer, T.; Thirring, K., Beiträge zur Chemie der Pyrrolpigmente, 25. Mitt. Die diastereomeren (geometrisch isomeren) Biliverdindimethylester—Struktur, Konfiguration und Konformation. *Monatshefte für Chemie - Chemical Monthly* **1978,** *109* (6), 1451-1473.

Fankhauser, C., The Phytochromes, a Family of Red/Far-red Absorbing Photoreceptors*. *Journal of Biological Chemistry* **2001,** *276* (15), 11453-11456.

Fenn, J. B.; Mann, M.; Meng, C. K.; Wong, S. F.; Whitehouse, C. M., Electrospray ionization for mass spectrometry of large biomolecules. *Science* **1989,** *246* (4926), 64.

Forbes, M. W.; Jockusch, R. A., Deactivation Pathways of an Isolated Green Fluorescent Protein Model Chromophore Studied by Electronic Action Spectroscopy. *Journal of the American Chemical Society* **2009,** *131* (47), 17038-+.

Forbes, M. W.; Nagy, A. M.; Jockusch, R. A., Photofragmentation of and electron photodetachment from a GFP model chromophore in a quadrupole ion trap. *International Journal of Mass Spectrometry* **2011,** *308* (2-3), 155-166.

Frangioni, J. V., In vivo near-infrared fluorescence imaging. *Current Opinion in Chemical Biology* **2003,** *7* (5), 626-634.

Frański, R.; Gierczyk, B.; Popenda, Ł.; Kasperkowiak, M.; Pędzinski, T., Identification of a biliverdin geometric isomer by means of HPLC/ESI–MS and NMR spectroscopy. Differentiation of the isomers by using fragmentation “in-source”. *Monatshefte für Chemie - Chemical Monthly* **2018,** *149* (6), 995-1002.

Frisch, M. J.; Trucks, G. W.; Schlegel, H. B.; Scuseria, G. E.; Robb, M. A.; Cheeseman, J. R.; Scalmani, G.; Barone, V.; Petersson, G. A.; Nakatsuji, H.; Li, X.; Caricato, M.; Marenich,

A. V.; Bloino, J.; Janesko, B. G.; Gomperts, R.; Mennucci, B.; Hratchian, H. P.; Ortiz, J. V.; Izmaylov, A. F.; Sonnenberg, J. L.; Williams; Ding, F.; Lipparini, F.; Egidi, F.; Goings, J.; Peng, B.; Petrone, A.; Henderson, T.; Ranasinghe, D.; Zakrzewski, V. G.; Gao, J.; Rega, N.; Zheng, G.; Liang, W.; Hada, M.; Ehara, M.; Toyota, K.; Fukuda, R.; Hasegawa, J.; Ishida, M.; Nakajima, T.; Honda, Y.; Kitao, O.; Nakai, H.; Vreven, T.; Throssell, K.; Montgomery Jr., J. A.; Peralta, J. E.; Ogliaro, F.; Bearpark, M. J.; Heyd, J. J.; Brothers, E. N.; Kudin, K. N.; Staroverov, V. N.; Keith, T. A.; Kobayashi, R.; Normand, J.; Raghavachari, K.; Rendell, A. P.; Burant, J. C.; Iyengar, S. S.; Tomasi, J.; Cossi, M.; Millam, J. M.; Klene, M.; Adamo, C.; Cammi, R.; Ochterski, J. W.; Martin, R. L.; Morokuma, K.; Farkas, O.; Foresman, J. B.; Fox, D. J. *Gaussian 16 Rev. C.01*, Wallingford, CT, 2016.

Fushimi, K.; Nakajima, T.; Aono, Y.; Yamamoto, T.; Ni Ni, W.; Ikeuchi, M.; Sato, M.; Narikawa, R., Photoconversion and Fluorescence Properties of a Red/Green-Type Cyanobacteriochrome AM1_C0023g2 That Binds Not Only Phycocyanobilin But Also Biliverdin. *Frontiers in Microbiology* **2016,** *7*, 588.

Garand, E.; Kamrath, M. Z.; Jordan, P. A.; Wolk, A. B.; Leavitt, C. M.; McCoy, A. B.; Miller, S. J.; Johnson, M. A., Determination of Noncovalent Docking by Infrared Spectroscopy of Cold Gas-Phase Complexes. *Science* **2012,** *335* (6069), 694.

Gouterman, M., Spectra of Porphyrins. *Journal of Molecular Spectroscopy* **1961,** *6*, 138-163.

Gouterman, M., 1 - Optical Spectra and Electronic Structure of Porphyrins and Related Rings. In *The Porphyrins*, Dolphin, D., Ed. Academic Press: 1978; pp 1-165.

Grabowski, Z. R.; Rotkiewicz, K.; Rettig, W., Structural Changes Accompanying Intramolecular Electron Transfer: Focus on Twisted Intramolecular Charge-Transfer States and Structures. *Chemical Reviews* **2003,** *103* (10), 3899-4032.

Grimme, S.; Antony, J.; Ehrlich, S.; Krieg, H., A consistent and accurate ab initio parametrization of density functional dispersion correction (DFT-D) for the 94 elements H-Pu. *J Chem Phys* **2010,** *132* (15), 154104.

Hein, B.; Willig, K. I.; Hell, S. W., Stimulated emission depletion (STED) nanoscopy of a fluorescent protein-labeled organelle inside a living cell. *Proceedings of the National Academy of Sciences of the United States of America* **2008,** *105* (38), 14271-14276.

Henley, A.; Fielding, H. H., Anion photoelectron spectroscopy of protein chromophores. *International Reviews in Physical Chemistry* **2019,** *38* (1), 1-34.

Holt, R. E.; Farrens, D. L.; Song, P. S.; Cotton, T. M., Surface-enhanced resonance Raman scattering (SERRS) spectroscopy applied to phytochrome and its model compounds. I. Biliverdin photoisomers. *Journal of the American Chemical Society* **1989,** *111* (26), 9156-9162.

Horke, D. A.; Verlet, J. R. R., Photoelectron spectroscopy of the model GFP chromophore anion. *Physical Chemistry Chemical Physics* **2012,** *14* (24), 8511-8515.

Houmøller, J.; Wanko, M.; Rubio, A.; Brøndsted Nielsen, S., Effect of a Single Water Molecule on the Electronic Absorption by o- and p-Nitrophenolate: A Shift to the Red or to the Blue? *The Journal of Physical Chemistry A* **2015,** *119* (47), 11498-11503.

Houmøller, J.; Wanko, M.; Støchkel, K.; Rubio, A.; Brøndsted Nielsen, S., On the Effect of a Single Solvent Molecule on the Charge-Transfer Band of a Donor–Acceptor Anion. *Journal of the American Chemical Society* **2013,** *135* (18), 6818-6821.

Kamarchik, E.; Krylov, A. I., Non-Condon Effects in the One- and Two-Photon Absorption Spectra of the Green Fluorescent Protein. *Journal of Physical Chemistry Letters* **2011,** *2* (5), 488-492.

Kamrath, M. Z.; Relph, R. A.; Guasco, T. L.; Leavitt, C. M.; Johnson, M. A., Vibrational predissociation spectroscopy of the H_2-tagged mono- and dicarboxylate anions of dodecanedioic acid. *International Journal of Mass Spectrometry* **2011,** *300* (2-3), 91-98.

Kang, S. H.; Jeong, M. J.; Eom, Y. K.; Choi, I. T.; Kwon, S. M.; Yoo, Y.; Kim, J.; Kwon, J.; Park, J. H.; Kim, H. K., Porphyrin Sensitizers with Donor Structural Engineering for Superior Performance Dye-Sensitized Solar Cells and Tandem Solar Cells for Water Splitting Applications. *Advanced Energy Materials* **2017,** *7* (7), 1602117.

Kiefer, H. V.; Pedersen, H. B.; Bochenkova, A. V.; Andersen, L. H., Decoupling Electronic versus Nuclear Photoresponse of Isolated Green Fluorescent Protein Chromophores Using Short Laser Pulses. *Physical Review Letters* **2016,** *117* (24).

Kirketerp, M.-B. S.; Petersen, M. Å.; Wanko, M.; Leal, L. A. E.; Zettergren, H.; Raymo, F. M.; Rubio, A.; Brøndsted Nielsen, M.; Brøndsted Nielsen, S., Absorption Spectra of 4-Nitrophenolate Ions Measured in Vacuo and in Solution. *ChemPhysChem* **2009,** *10* (8), 1207-1209.

Kirketerp, M. B. S.; Petersen, M. Å.; Wanko, M.; Zettergren, H.; Rubio, A.; Brøndsted Nielsen, M.; Brøndsted Nielsen, S., Double-Bond versus Triple-Bond Bridges: Does it Matter for the Charge-Transfer Absorption by Donor–Acceptor Chromophores? *ChemPhysChem* **2010,** *11* (12), 2495-2498.

Klots, C. E., TEMPERATURES OF EVAPORATING CLUSTERS. *Nature* **1987,** *327* (6119), 222-223.

Kozłowska, J.; Wielgus, M.; Bartkowiak, W., TD-DFT Study on the Charge-Transfer Excitations of Anions Possessing Double or Triple Bonds. *Computational and Theoretical Chemistry* **2013,** *1014*, 49-55.

Lammich, L.; Petersen, M. A.; Nielsen, M. B.; Andersen, L. H., The gas-phase absorption spectrum of a neutral GFP model chromophore. *Biophysical Journal* **2007,** *92* (1), 201-207.

Langeland, J.; Kjaer, C.; Andersen, L. H.; Nielsen, S. B., The Effect of an Electric Field on the Spectroscopic Properties of the Isolated Green Fluorescent Protein Chromophore Anion. *Chemphyschem* **2018,** *19* (14), 1686-1690.

Leavitt, C. M.; Wolk, A. B.; Fournier, J. A.; Kamrath, M. Z.; Garand, E.; Van Stipdonk, M. J.; Johnson, M. A., Isomer-Specific IR–IR Double Resonance Spectroscopy of D_2-Tagged Protonated Dipeptides Prepared in a Cryogenic Ion Trap. *The Journal of Physical Chemistry Letters* **2012,** *3* (9), 1099-1105.

Lightner, D. A.; Holmes, D. L.; McDonagh, A. F., On the Acid Dissociation Constants of Bilirubin and Biliverdin: pKa VALUES FROM 13C NMR SPECTROSCOPY (*). *Journal of Biological Chemistry* **1996,** *271* (5), 2397-2405.

Lin., S.; Diercks., C. S.; Zhang., Y.-B.; Kornienko., N.; Nichols., E. M.; Zhao., Y.; Paris., A. R.; Kim., D.; Yang., P.; Yaghi., O. M.; Chang., C. J., Covalent organic frameworks comprising cobalt porphyrins for catalytic CO_2 reduction in water. *Science* **2015,** *349* (6253), 1208-1213.

Litvinenko, K. L.; Webber, N. M.; Meech, S. R., Internal conversion in the chromophore of the green fluorescent protein: Temperature dependence and isoviscosity analysis. *Journal of Physical Chemistry A* **2003,** *107* (15), 2616-2623.

Lopes, J. M. S.; Sharma, K.; Sampaio, R. N.; Batista, A. A.; Ito, A. S.; Machado, A. E. H.; Araujo, P. T.; Barbosa Neto, N. M., Novel insights on the vibronic transitions in free base meso-tetrapyridyl porphyrin. *Spectrochim Acta A Mol Biomol Spectrosc* **2019,** *209*, 274-279.

Mamedov, V. A.; Kalinin, A. A., Chapter Two - Quinoxaline Macrocycles. In *Advances in Heterocyclic Chemistry*, Katritzky, A. R., Ed. Academic Press: 2014; Vol. 112, pp 51-115.

Mandal, D.; Tahara, T.; Meech, S. R., Excited-state dynamics in the green fluorescent protein chromophore. *Journal of Physical Chemistry B* **2004,** *108* (3), 1102-1108.

Marsh, B. M.; Voss, J. M.; Garand, E., A dual cryogenic ion trap spectrometer for the formation and characterization of solvated ionic clusters. *Journal of Chemical Physics* **2015,** *143* (20), 1-7.

Martin, M. E.; Negri, F.; Olivucci, M., Origin, nature, and fate of the fluorescent state of the green fluorescent protein chromophore at the CASPT2//CASSCF resolution. *Journal of the American Chemical Society* **2004,** *126* (17), 5452-5464.

McLaughlin, C.; Assmann, M.; Parkes, M. A.; Woodhouse, J. L.; Lewin, R.; Hailes, H. C.; Worth, G. A.; Fielding, H. H., ortho and para chromophores of green fluorescent protein:

controlling electron emission and internal conversion. *Chemical Science* **2017,** *8* (2), 1621-1630.

Michenfelder, N. C.; Ernst, H. A.; Schweigert, C.; Olzmann, M.; Unterreiner, A. N., Ultrafast Stimulated Emission of Nitrophenolates in Organic and Aqueous Solutions. *Physical Chemistry Chemical Physics* **2018,** *20* (16), 10713-10720.

Montecinos-Franjola, F.; Lin, J. Y.; Rodriguez, E. A., Fluorescent proteins for in vivo imaging, where's the biliverdin? *Biochemical Society Transactions* **2020,** *48* (6), 2657-2667.

Mooney, C. R. S.; Horke, D. A.; Chatterley, A. S.; Simperler, A.; Fielding, H. H.; Verlet, J. R. R., Taking the green fluorescence out of the protein: dynamics of the isolated GFP chromophore anion. *Chemical Science* **2013,** *4* (3), 921-927.

Mooney, C. R. S.; Parkes, M. A.; Zhang, L. J.; Hailes, H. C.; Simperler, A.; Bearpark, M. J.; Fielding, H. H., Competition between photodetachment and autodetachment of the 2(1)pi pi* state of the green fluorescent protein chromophore anion. *Journal of Chemical Physics* **2014,** *140* (20).

Mooney, C. R. S.; Sanz, M. E.; McKay, A. R.; Fitzmaurice, R. J.; Aliev, A. E.; Caddick, S.; Fielding, H. H., Photodetachment Spectra of Deprotonated Fluorescent Protein Chromophore Anions. *Journal of Physical Chemistry A* **2012,** *116* (30), 7943-7949.

Nagornova, N. S.; Rizzo, T. R.; Boyarkin, O. V., Exploring the Mechanism of IR–UV Double-Resonance for Quantitative Spectroscopy of Protonated Polypeptides and Proteins. *Angewandte Chemie International Edition* **2013,** *52* (23), 6002-6005.

Navrátil, R.; Jašík, J.; Roithová, J., Visible photodissociation spectra of gaseous rhodamine ions: Effects of temperature and tagging. *Journal of Molecular Spectroscopy* **2017,** *332*, 52-58.

Neese, F., The ORCA program system. *WIREs Computational Molecular Science* **2011,** *2* (1), 73-78.

Neese, F., Software update: the ORCA program system, version 4.0. *WIREs Computational Molecular Science* **2017,** *8* (1), 1327.

Nielsen, S. B.; Lapierre, A.; Andersen, J. U.; Pedersen, U. V.; Tomita, S.; Andersen, L. H., Absorption spectrum of the green fluorescent protein chromophore anion in vacuo. *Physical Review Letters* **2001,** *87* (22).

O. N. Korotaev, R. I. P., Reversible Transformations of Luminescent Impurity Centers in an N-Paraffin Matrix Under Laser Irradiation. *Optics and Spectroscopy* **1971,** *32* (5), 479-480.

Ormö, M.; Cubitt, A. B.; Kallio, K.; Gross, L. A.; Tsien, R. Y.; Remington, S. J., Crystal Structure of the *Aequorea victoria* Green Fluorescent Protein. *Science* **1996,** *273* (5280), 1392-1395.

Panja, S. K.; Dwivedi, N.; Saha, S., Tuning the Intramolecular Charge Transfer (ICT) Process in Push-Pull Systems: Effect of Nitro Groups. *RSC Advances* **2016,** *6* (107), 105786-105794.

Prazeres, R.; Berset, J. M.; Chaput, R.; Glotin, F.; Jaroszynski, D. A.; Ortega, J. M., CLIO, an infrared free electron laser facility. *Nuclear Instruments and Methods in Physics Research Section B: Beam Interactions with Materials and Atoms* **1994,** *89* (1), 54-59.

Radziszewski, J. G.; Waluk, J.; Nepras, M.; Michl, J., Fourier transform fluorescence and phosphorescence of porphine in rare gas matrixes. *The Journal of Physical Chemistry* **1991,** *95* (5), 1963-1969.

Rimington., C.; Mason., S. F.; Kennard, O., Porphin. *Spectrochimiea Acta* **1957,** *12,* 65-77.

Rockwell, N. C.; Lagarias, J. C., A Brief History of Phytochromes. *ChemPhysChem* **2010,** *11* (6), 1172-1180.

Santoro, F.; Lami, A.; Improta, R.; Bloino, J.; Barone, V., Effective method for the computation of optical spectra of large molecules at finite temperature including the Duschinsky and Herzberg-Teller effect: the Q_x band of porphyrin as a case study. *J Chem Phys* **2008,** *128* (22), 224311.

Sayfutyarova, E. R.; Hammes-Schiffer, S., Constructing Molecular pi-Orbital Active Spaces for Multireference Calculations of Conjugated Systems. *J Chem Theory Comput* **2019,** *15* (3), 1679-1689.

Scolaro., L. M.; Castriciano., M.; Romeo., A.; Patane., S.; Cefali., E.; Allegrini., M., Aggregation Behavior of Protoporphyrin IX in Aqueous Solutions: Clear Evidence of Vesicle Formation. *J. Phys. Chem. B* **2002,** (106), 2453-2459.

Shimomura, O., Discovery of Green Fluorescent Protein (GFP) (Nobel Lecture). *Angewandte Chemie International Edition* **2009,** *48* (31), 5590-5602.

Shimomura, O.; Johnson, F. H.; Masugi, T., Cypridina Bioluminescence: Light-Emitting Oxyluciferin-Luciferase Complex. *Science* **1969,** *164* (3885), 1299.

Støchkel, K.; Hansen, C. N.; Houmøller, J.; Nielsen, L. M.; Anggara, K.; Linares, M.; Norman, P.; Nogueira, F.; Maltsev, O. V.; Hintermann, L.; Nielsen, S. B.; Naumov, P.; Milne, B. F., On the Influence of Water on the Electronic Structure of Firefly Oxyluciferin Anions from Absorption Spectroscopy of Bare and Monohydrated Ions in Vacuo. *Journal of the American Chemical Society* **2013,** *135* (17), 6485-6493.

Stockett, M. H.; Boesen, M.; Houmøller, J.; Brøndsted Nielsen, S., Accessing the Intrinsic Nature of Electronic Transitions from Gas-Phase Spectroscopy of Molecular Ion/Zwitterion Complexes. *Angewandte Chemie* **2017,** *129* (13), 3544-3549.

Sun, Q.; Yang, J.; Chan, G. K.-L., A general second order complete active space self-consistent-field solver for large-scale systems. *Chemical Physics Letters* **2017,** *683*, 291-299.

Sun, Q.; Zhang, X.; Banerjee, S.; Bao, P.; Barbry, M.; Blunt, N. S.; Bogdanov, N. A.; Booth, G. H.; Chen, J.; Cui, Z.-H.; Eriksen, J. J.; Gao, Y.; Guo, S.; Hermann, J.; Hermes, M. R.; Koh, K.; Koval, P.; Lehtola, S.; Li, Z.; Liu, J.; Mardirossian, N.; McClain, J. D.; Motta, M.; Mussard, B.; Pham, H. Q.; Pulkin, A.; Purwanto, W.; Robinson, P. J.; Ronca, E.; Sayfutyarova, E.; Scheurer, M.; Schurkus, H. F.; Smith, J. E. T.; Sun, C.; Sun, S.-N.; Upadhyay, S.; Wagner, L. K.; Wang, X.; White, A.; Whitfield, J. D.; Williamson, M. J.; Wouters, S.; Yang, J.; Yu, J. M.; Zhu, T.; Berkelbach, T. C.; Sharma, S.; Sokolov, A.; Chan, G. K.-L., Recent developments in the PySCF program package. *Chemical Physics* **2020,** *arXiv:2002. 12531*.

Sun., Q.; Timothy C. Berkelbach; Nick S. Blunt; George H. Booth; Sheng Guo; Zhendong Li; Junzi Liu; James D. McClain; Elvira R. Sayfutyarova; Sandeep Sharma; Sebastian Wouters; Chan, G. K.-L., PySCF: the Python-based simulations of chemistry framework. *WIREs Comput Mol Sci* **2018**, 1340.

Tay, J.; Parkes, M. A.; Addison, K.; Chan, Y. H.; Zhang, L. J.; Hailes, H. C.; Page, P. C. B.; Meech, S. R.; Blancafort, L.; Fielding, H. H., The Effect of Conjugation. on the Competition between Internal Conversion and Electron Detachment: A Comparison between Green Fluorescent and Red Kaede Protein Chromophores. *Journal of Physical Chemistry Letters* **2017,** *8* (4), 765-771.

Tchekanda, E.; Sivanesan, D.; Michnick, S. W., An infrared reporter to detect spatiotemporal dynamics of protein-protein interactions. *Nature Methods* **2014,** *11* (6), 641-644.

Tessore, F.; Biroli, A. O.; Di Carlo, G.; Pizzotti, M., Porphyrins for Second Order Nonlinear Optics (NLO): An Intriguing History. *Inorganics* **2018,** *6* (3), 81.

Toker, Y.; Rahbek, D. B.; Klaerke, B.; Bochenkova, A. V.; Andersen, L. H., Direct and Indirect Electron Emission from the Green Fluorescent Protein Chromophore. *Physical Review Letters* **2012,** *109* (12).

Tsien, R. Y., The green fluorescent protein. *Annu. Rev. Biochem.* **1998,** *67*, 509-544.

van Geenen, F. A. M. G.; Kranenburg, R. F.; van Asten, A. C.; Martens, J.; Oomens, J.; Berden, G., Isomer-Specific Two-Color Double-Resonance IR2MS3 Ion Spectroscopy Using a Single Laser: Application in the Identification of Novel Psychoactive Substances. *Analytical Chemistry* **2021,** *93* (4), 2687-2693.

Voliani, V.; Bizzarri, R.; Nifosi, R.; Abbruzzetti, S.; Grandi, E.; Viappiani, C.; Beltram, F., Cis-trans photoisomerization of fluorescent-protein chromophores. *Journal of Physical Chemistry B* **2008,** *112* (34), 10714-10722.

Voss, J. M.; Fischer, K. C.; Garand, E., Revealing the structure of isolated peptides: IR-IR predissociation spectroscopy of protonated triglycine isomers. *Journal of Molecular Spectroscopy* **2018,** *347*, 28-34.

Wagner, U. G.; Müller, N.; Schmitzberger, W.; Falk, H.; Kratky, C., Structure Determination of te Biliverdin Apomyoglobin Complex: Crystal Structure Analysis of Two Crystal Forms at 1.4 and 1.5 Å Resolution. *Journal of Molecular Biology* **1995,** *247* (2), 326-337.

Wanko, M.; Houmoller, J.; Stochkel, K.; Kirketerp, M.-B. S.; Petersen, M. Å.; Brøndsted Nielsen, M.; Brøndsted Nielsen, S.; Rubio, A., Substitution Effects on the Absorption Spectra of Nitrophenolate Isomers. *Physical Chemistry Chemical Physics* **2012,** *14* (37), 12905-12911.

Weber, J. M.; Robertson, W. H.; Johnson, M. A., Argon predissociation and electron autodetachment spectroscopy of size-selected $CH_3NO_2^-\cdot Ar_n$ clusters. *The Journal of Chemical Physics* **2001,** *115* (23), 10718-10723.

Weigend, F.; Ahlrichs, R., Balanced Basis Sets of Split Valence, Triple Zeta Valence and Quadruple Zeta Valence Quality for H to Rn: Design and Assessment of Accuracy. *Phys. Chem. Chem. Phys.* **2005,** *7* (18), 3297-3305.

Weissleder, R., A clearer vision for in vivo imaging. *Nature Biotechnology* **2001,** *19* (4), 316-317.

West, C. W.; Bull, J. N.; Hudson, A. S.; Cobb, S. L.; Verlet, J. R. R., Excited State Dynamics of the Isolated Green Fluorescent Protein Chromophore Anion Following UV Excitation. *Journal of Physical Chemistry B* **2015,** *119* (10), 3982-3987.

West, C. W.; Hudson, A. S.; Cobb, S. L.; Verlet, J. R. R., Communication: Autodetachment versus internal conversion from the S_1 state of the isolated GFP chromophore anion. *Journal of Chemical Physics* **2013,** *139* (7).

Wester, R., Radiofrequency Multipole Traps: Tools for Spectroscopy and Dynamics of Cold Molecular Ions. *Journal of Physics B: Atomic, Molecular and Optical Physics* **2009,** *42* (15), 154001.

Western, C. M., PGOPHER: A Program for Simulating Rotational, Vibrational and Electronic Spectra. *Journal of Quantitative Spectroscopy and Radiative Transfer* **2017,** *186*, 221-242.

Wiley, W. C.; McLaren, I. H., Time-of-Flight Mass Spectrometer with Improved Resolution. *Review of Scientific Instruments* **1955,** *26* (12), 1150-1157.

Wolke, C. T.; Menges, F. S.; Totsch, N.; Gorlova, O.; Fournier, J. A.; Weddle, G. H.; Johnson, M. A.; Heine, N.; Esser, T. K.; Knorke, H.; Asmis, K. R.; McCoy, A. B.; Arismendi-Arrieta, D. J.; Prosmiti, R.; Paesani, F., Thermodynamics of Water Dimer Dissociation in the Primary Hydration Shell of the Iodide Ion with Temperature-Dependent Vibrational Predissociation Spectroscopy. *Journal of Physical Chemistry A* **2015,** *119* (10), 1859-1866.

Woods, L. A.; Radford, S. E.; Ashcroft, A. E., Advances in ion mobility spectrometry–mass spectrometry reveal key insights into amyloid assembly. *Biochimica et Biophysica Acta (BBA) - Proteins and Proteomics* **2013,** *1834* (6), 1257-1268.

Wyer, J. A.; Jensen, C. S.; Brøndsted Nielsen, S., Gas-phase action spectroscopy of protoporphyrin IX (PP) and zinc-PP anions from 210nm to 720nm. *International Journal of Mass Spectrometry* **2011,** *308* (1), 126-132.

Xu, S.; Gozem, S.; Krylov, A. I.; Christopher, C. R.; Mathias Weber, J., Ligand influence on the electronic spectra of monocationic copper–bipyridine complexes. *Physical Chemistry Chemical Physics* **2015,** *17* (47), 31938-31946.

Xu, S.; Gozem, S.; Krylov, A. I.; Christopher, C. R.; Weber, J. M., Ligand Influence on the Electronic Spectra of Monocationic Copper–Bipyridine Complexes. *Physical Chemistry Chemical Physics* **2015,** *17* (47), 31938-31946.

Xu, S.; Smith, J. E. T.; Weber, J. M., The electronic spectrum of cryogenic ruthenium-tris-bipyridine dications in vacuo. *The Journal of Chemical Physics* **2016,** *145* (2), 024304.

Xu, S.; Smith, J. E. T.; Weber, J. M., Hydration of a Binding Site with Restricted Solvent Access – Solvatochromic Shift of the Electronic Spectrum of a Ruthenium Polypyridine Complex, One Molecule at a Time. *J. Phys. Chem. A* **2016,** *120*, 7650–7658.

Yanai, T.; Tew, D. P.; Handy, N. C., A new hybrid exchange–correlation functional using the Coulomb-attenuating method (CAM-B3LYP). *Chemical Physics Letters* **2004,** *393* (1-3), 51-57.

Yella., A.; Lee., H.-W.; Tsao., H. N.; Yi., C.; Chandiran., A. K.; Nazeeruddin., M. K.; Diau., E. W.-G.; Yeh., C.-Y.; Zakeeruddin., S. M.; Gratzel., M., Porphyrin-Sensitized Solar Cells with Cobalt (II/III)-Based Redox Electrolyte Exceed 12 Percent Efficiency. *Science* **2011,** *334* (6056), 629-634.

Zagorec-Marks, W.; Foreman, M. M,; Verlet, J. R. R.; Weber, J. M., Cryogenic Ion Spectroscopy of the Green Fluorescent Protein Chromophore in Vacuo. *Journal of Physical Chemistry Letters* **2019,** 10, 7817-7822.

Zagorec-Marks, W.; Foreman, M. M,; Verlet, J. R. R.; Weber, J. M., Probing the Microsolvation Environment of the Green Fluorescent Protein Chomophore in Vacuo. *Journal of Physical Chemistry Letters* **2020**, 11, 1940-1946.

Zagorec-Marks, W.; Foreman, M. M.; Weber, J. M., Tag-Free, Temperature Dependent Infrared Spectra of the GFP Chromophore – Revisiting the Question of Isomerism. *Journal of Physical Chemistry A* **2020**, 124, 7827−7831.

Zagorec-Marks, W.; Smith, J. E. T.; Foreman, M. M.; Sharma, S.; Weber, J. M., Intrinsic electronic spectra of cryogenically prepared protoporphyrin IX ions in vacuo – deprotonation-induced Stark shifts. *Physical Chemistry Chemical Physics* **2020,** *22* (36), 20295-20302.

Zahedi, M.; Ghiasi, M.; Safari, N., Modeling of biliverdin reduction process: regio-specificity and H-bonding. *Chemical Physics* **2005,** *310* (1), 179-187.

Zuev, D.; Bravaya, K. B.; Makarova, M. V.; Krylov, A. I., Effect of microhydration on the electronic structure of the chromophores of the photoactive yellow and green fluorescent proteins. *Journal of Chemical Physics* **2011,** *135* (19).